ABSTRACT

Title of dissertation: ULTRACOLD PLASMA DYNAMICS
                           IN A MAGNETIC FIELD

Xianli Zhang, Doctor of Philosophy, 2009

Dissertation directed by: Professor Steven Rolston
                              Department of Physics

Plasmas, often called the fourth state of matter and the most common one in the universe, have parameters varying by many orders of magnitude, from temperature of a few hundred kelvin in the Earth's ionosphere to 10^{16} K in the magnetosphere of a pulsar. Ultracold plasmas, produced by photoionizing a sample of laser-cooled and trapped atoms near the ionization limit, have extended traditional neutral plasma parameters by many orders of magnitude, to electron temperatures below 1 K and ion temperatures in the tens of μK to a few Kelvin, and densities of 10^5 cm^{-3} to 10^{10} cm^{-3}. These plasmas thus provide a testing ground to study basic plasma theory in a clean and simple system with or without a magnetic field. Previous studies of ultracold plasmas have primarily concentrated on temperature measurements, collective modes and expansion dynamics in the absence of magnetic fields.

This thesis presents the first study of ultracold plasma dynamics in a magnetic field. The presence of a magnetic field during the expansion can initiate various phenomena, such as plasma confinement and plasma instabilities. While the electron

temperatures are very low in ultracold plasmas, we need only tens of Gauss of magnetic field to observe significant effects on the expansion dynamics. To probe the ultraocold plasma dynamics in a magnetic field, we developed a new diagnostic - projection imaging, which images the ion distribution by extracting the ions with a high voltage pulse onto a position-sensitive detector. Early in the lifetime of the plasma ($< 20 \mu$s), the size of the image is dominated by the time-of-flight Coulomb explosion of the dense ion cloud. For later times, we measure the 2-D Gaussian width of the ion image, obtaining the transverse expansion velocity as a function of magnetic field (up to 70 G),and observe that the transverse expansion velocity scales as $B^{-1/2}$, explained by a nonlinear ambipolar diffusion model that involes anisotropic diffusion in two different directions.

We also present the first observation of a plasma instability in an expanding ultracold plasma. We observe periodic emission of electrons from an ultracold plasma in weak, crossed magnetic and electric fields, and a strong perturbed electron density distribution in electron time-of-flight projection images. We identify this instability as a high-frequency electron drift instability due to the coupling between the electron drift wave and electron cyclotron harmonic, which has large wavenumbers corresponding to wavelengths close to the electron gyroradius.

ULTRACOLD PLASMA DYNAMICS
IN A MAGNETIC FIELD

by

Xianli Zhang

Dissertation submitted to the Faculty of the Graduate School of the
University of Maryland, College Park in partial fulfillment
of the requirements for the degree of
Doctor of Philosophy
2009

Advisory Committee:
Professor Steven Rolston, Chair/Advisor, University of Maryland
Professor Thomas Antonsen, University of Maryland
Professor Howard Milchberg, University of Maryland
Professor Luis Orozco, University of Maryland
Professor Michael Coplan, University of Maryland

Dedication

To Xiaochun and Daniel.

Acknowledgments

There are many people to whom I owe great thanks for contributing to this thesis and supporting me throughout the past few years. Without the supports and encourages from them, this accomplishment will never come to be true.

First and foremost I'd like to thank my advisor, Professor Steven Rolston for giving me an opportunity to work on challenging and interesting projects, and providing excellent guidance and support throughout my graduate career. Under his guidance, I learnt not only how to become a good scientist but also a good human being. It has been a pleasure to work with and learn from such an extraordinary individual. I would also like to thank my committee member, Professor Luis Orozco for his help and suggestions at various states of the research project, and also thank my other committee members, Professor Thomas Antonsen, Professor Howard Milchberg, and Professor Michael Coplan for their invaluable time reviewing the manuscript.

This PhD would have been an impossible task without the help and support of my group memebers. Dr. Robert S. Fletcher was the person I worked together for about four years since I joined the ultracold plasma lab. I will cherish the experience to overcome the difficulties, experience suffering time as well as exciting moments together with such a talent guy. I would like to thank other group members for their help and friendship, Emily Edwards, Matt Beeler, Brendan Wyker, Tommy Willis, Jennifer Robinson, Ilya Arakelyan, Kevin Twedt and post-doc Hong Tao.

Our group is close to the group of Luis Orozco since fall 2003 when both Steve

and Luis moved to Maryland for a strong program in AMO physics. I would like to give thanks to Orozco's members Rebecca Olson, Basudev Roy, Michael Scholten, David Norris, Elohim Becerra, Dong Sheng, Adrian Perez-Galvan, post-docs Yanting Zhao and Jietai Jing. Since fall 2007, Prof. Christopher Monroe's ion trap group joined the AMO group and Joint Quantum Institute. it is very fruitful to Interact with his members, such as Ming-Shien Chang, Simcha Korenblit, Jon Sterk, Le Luo and Dzmitry Matsukevich.

In particular I am grateful to Professor William Dorland, Dr. Parvez N. Guzdar and Dr. Marc Swisdak for collaboration with Steven and myself. We have both benefitted from their contributions to our work. Without their extraordinary theoretical ideas and computational expertise, this thesis would have been a distant dream.

I am thankful for the assistance from department staff, Jane Hessing for her continuous assistance for graduate student, Robert Dahms and Jesse Anderson for their careful work on equipment purchase, Richard Terlisner and Dave Cogswell for teaching me physics shop techniques. All of these were invaluable for my study and research.

Finally, I owe my deepest thanks to my wife Xiaochun for always supporting and encourage me, and for making the personal and financial sacrifices that are part of my graduate student life. I would also like to thank my parents, brother and in-laws for their love and support.

Table of Contents

List of Figures

viii

Chapter 1

Introduction

1.1 Backgroud

Conventional neutral plasmas, such as fluorescent light bulbs (10^4 K), the solar core (10^7 K), or magnetic fusion plasmas (10^8 K), are relatively hot because they are created from atoms and molecules that are ionized by collisions between particles. With the techniques of laser cooling and trapping developed in atomic physics, we can create ultracold neutral plasmas (UCPs) at electron temperatures as low as 1 K and ion temperatures of 1 mK and peak densities of 10^5 to 10^{10} cm^{-3} [1]. Under such low temperature conditions, the UCPs can access the parameter regime known as strongly coupled plasmas, where the ratio of Coulomb potential energy to the kinetic energy is greater than one ($\Gamma_{e,i} = e^2/4\pi\epsilon_0 a k_B T_{e,i}$, where e is the electron charge, ϵ_0 is the vacuum permittivity, and a is the Wigner-Seitz radius - the average interparticle spacing.) (Figure 1.1) [2]. Strongly coupled neutral plasmas are very difficult to create in the lab, although they do exist in dense astrophysical systems such as the interiors of large planets and white dwarf stars. Study of ultracold plasmas may help us to better understand and probe these exotic states of matter.

The dynamics of UCPs are similar to other laser-produced plasmas that are created by an intense laser irradiation of a solid [3, 4], thin film target [5, 6, 7, 8], rare gas cluster [9] or gas jet [10, 11]. However, these hot plasmas have much higher
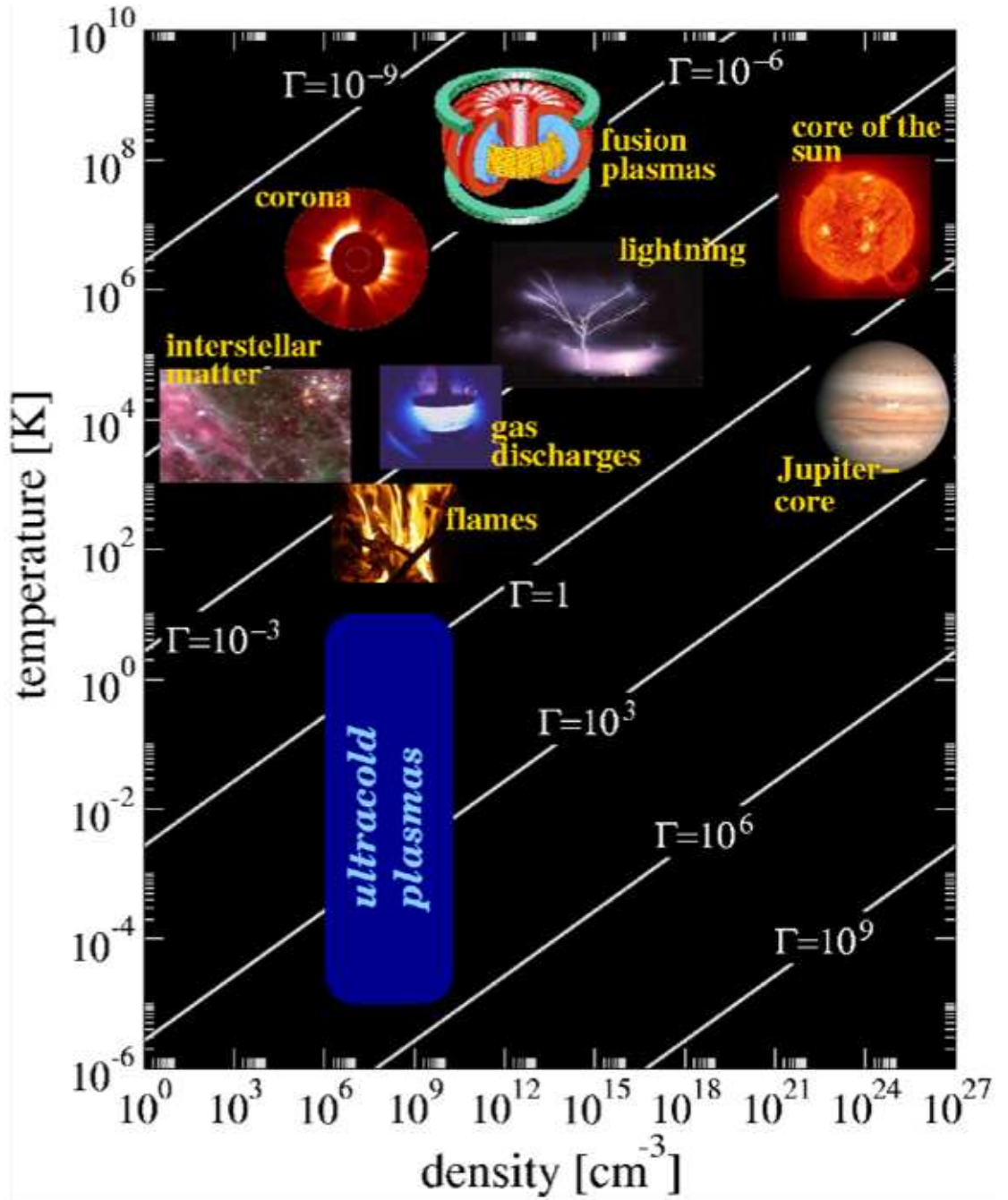
Figure 1.1: Neutral plasmas in the density-temperature parameter plane [2]. Lines of constant Coulomb coupling parameter Γ are indicated. UCPs are in or near the strongly coupled regime.

2

densities than UCPs, and the ions and electrons are at MeV temperatures. High densities and temperatures make it challenging to observe the plasma dynamics, which happen on the scale of the inverse plasma frequency, $\omega_p^{-1} = \sqrt{m\epsilon_0/e^2 n_e}$ (where m is the electron mass, ϵ_0 is the vacuum permitivity, e is the electron charge, and n_e is the electron density), which is on the order of attoseconds for electrons and femtoseconds for ions. UCPs have an advantage over these hot plasmas, in that, due to their much colder temperature and lower density, the ions and electrons expand on a time scale that is easily observable using optical probes [12, 13, 14, 15] or charged-particle detection techniques [16]. Unlike many other plasma experiments that usually require large facilities, ultracold plasma experiments are tabletop physics with a small vacuum chamber and associated laser hardware. UCPs also offer a high level of control and diagnostics. By varying laser intensities and wavelengths, it is possible to accurately set the initial density and energy of the system. Ultracold plasmas, therefore, provide a simple and clean system to study and test basic plasma theory and to understand the plasmas that exist in certain astrophysical systems because of the excellent control over the initial conditions and a widely accessible parameter space.

The study of UCPs began at the National Institute of Standards and Technology (NIST) in Gaithersburg, where S. L. Rolston's group made UCPs by photoionizing a sample of laser-cooled metastable xenon atoms [1]. Since then, a few other experimental groups started working with UCPs of different elements. T. C. Killian at Rice University currently works with strontium [13]; S. Bergeson at Brigham Young University works with calcium [14, 15]; G. Raithel at University of Michigan

works with rubidium [17]. Newer UCP experiments are typically made using second column elements such as strontium and calcium as these ions have optical transitions that are easy accessible for imaging the plasma ions using either absorption or fluorescence. Besides, there is the possibility to laser cool the ions in the plasma to push the ions very deeply in the strong coupling regime.

Immediately after the creation of an UCP through photoionization, the system is far from equilibrium and many UCP studies focus on the establishment of local and global thermal equilibrium. The lighter electrons thermalize within 10-100 ns [18], but the ions are essentially stationary on this time scale. The local thermodynamic equilibrium (LTE) of the ions occurs on a microsecond timescale, and is conveniently studied experimentally by optical techniques, such as absorption imaging [19], fluorescence imaging [14] and sheet fluorescence [20]. Chen *et al.* [19] studied the effective ion temperature evolution, and obseved a predicted heating effect [21] - disorder-induced heating that rapidly heats the ions to several kelvin before the plasma expands (the ion coupling parameter is about 1-5). Immediately after the photoionization, the ions have very little kinetic energy and are spatially uncorrelated because of their initial random distribution in the magneto-optical trap (MOT). There is more potential energy in the system compared to the equilibrium state. As ions equilibrate and correlations develop, the excess potential energy is converted into kinetic energy, heating the ions. The electrons also undergo disorder induced heating, although at a very fast rate (effectively spontaneous upon ionization), leading to an effective lower limit of the electron temperature of a few Kelvin (dependent on density). Besides the disorder-induced heating, another important

4

phenomenon was observed and studied during the ion approach to equilibrium by Chen *et al.* [19], and more recently by Castro *et al.* [20] - ion kinetic energy oscillations, which are general phenomena characteristic of strongly coupled systems approaching equilibrium. This oscillation damps out very quickly (in about 5 μs) due to density variations within the plasma.

After the plasma reaches LTE, the entire plasma expands into the surrounding vacuum on a timescale of tens of microseconds as a result of the electron thermal pressure. This is studied experimentally with various methods such as charged particle detection [16, 22], optical probes [13, 14, 15, 19, 20]. S. Kulin *et al.* [16] studied the plasma expansion using excitation of the electron plasma oscillations as a probe of the density and final expansion velocity. More recently, Fletcher *et al.* [22] observed a set of collective modes related to electron sound waves, known as Tonks-Dattner resonances, which may be used to study the plasma dynamics and electron temperature evolution in the plasma expansion. Cummings *et al.* [14, 15] used ion fluorescence to follow the spatial expansion of a calcium plasma. Simien *et al.* [13] used optical absorption and Castro *et al.* [20] used sheet fluorescence to study ion dynamics in a strontium plasma.

There has also been some experimental study on the various physical processes that heat the electrons during plasma expansion and the electron temperature evolution. Kulin *et al.* [16] measured the final asymptotic velocity of the plasma and related it to the initial electron temperature of the plasma, and obseved extra heating for initial electron temperatures less than 60 K. Roberts *et al.* [23] studied the electron temperature evolution by tilting the potential well of the plasma using an

electric field and measuring ejected electrons. P. Gupta *et al.* [24, 25] studied the electron temperature evolution by using a combination of spectroscopic ion-velocity measurements and numerical simulations. Fletcher *et al.* [26] studied the electron temperature evolution over a wide time range after the formation of plasma using the strong temperature dependence of the three-body recombination rate.

UCPs have been studied theoretically as well. Theoretical and numerical simulations of UCPs are challenging since the ions and electrons evolve on dramatically different time scales, which need to be treated differently. Mazevet *et al.* [27] did the first large-scale simulations of an UCP and studied the various processes that are significant during plasma evolution. They reproduced many of the results from the first experimental study on UCPs [1, 16]. Kuzmin *et al.* [28, 29] simulated the evolution of UCPs with special emphasis on the electron temperature evolution. They found that the various electron heating effects prevent electron-electron correlations from developing in an expanding UCP. Robicheaux *et al.* [30, 31] studied in detail, the effect of recombination on the electron temperature evolution during plasma expansion. They investigated certain plasma processes such as ion acoustic waves, density spike formation, and electron evaporation; and also simulated the evolution of a cold Rydberg gas into a plasma. Pohl *et al.* [32] did a theoretical study of the Rydberg to plasma transition as well. They suggest that the ionization process begins with some seed charges produced by black-body radiation which then collide with the Rydberg atoms to initiate an avalanche-like ionization process. They also studied the UCP dynamics by using kinetic modeling and molecular dynamics simulations that included ionic correlations [33, 34].

6

All the previous UCP studies focused on free expansion, in the abscence of a magnetic field. The presence of a magnetic field during the expansion can initiate various phenomena, such as plasma confinement and plasma instabilities. This thesis describes the first study of UCP dynamics in a magnetic field. The remainder of Chapter 1 discusses how to create UCPs from a sample of laser-cooled and trapped atoms. Chapter 2 describes UCP dynamics in the absence of a magnetic field, such as free expansion and temperature evolution. Chapter 3 discusses UCP expansion in a constant magnetic field by a newly developed technique - time-of-flight projection imaging. Chapter 4 focusses on the study of an UCP instability in a weak crossed magnetic and electric field, which is identified as a high frequency electron drift instability. Chapter 5 summarizes the conclusions from the thesis and ongoing and future work.

1.2   Creation of Ultracold Neutral Plasmas

The first ultracold plasma was created at NIST with metastable xenon by Killian *et al.* [1]. This apparatus was used for the experiments described in this work since it was moved to University of Maryland - College Park in 2003.

Xenon is a noble gas with nine stable isotopes (seven bosonic isotopes from ^{124}Xe to ^{136}Xe with no nuclear spin and two fermionic isotopes ^{129}Xe and ^{131}Xe with nuclear spin I=1/2 and I=3/2, respectively). The ^{132}Xe bosonic isotope is typically used to make the MOT and create the UCP since it has no nuclear spin and no hyperfine structure and thus the benefit of not requiring repumper beams in the
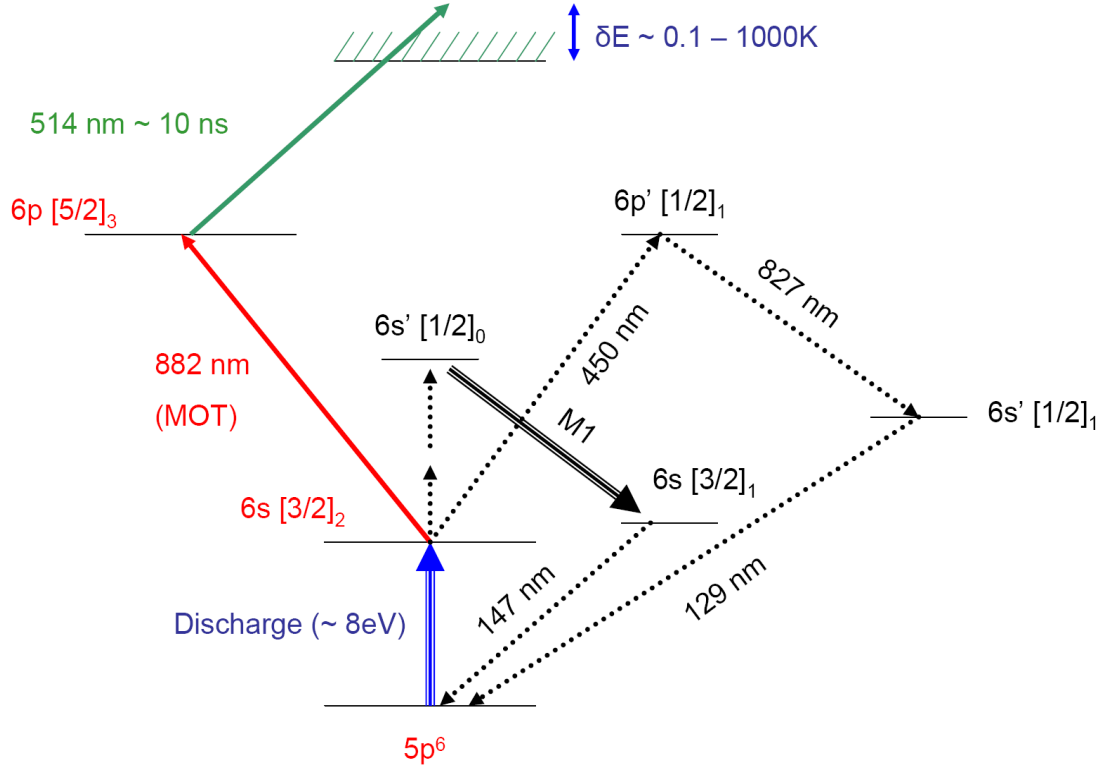
Figure 1.2: A DC discharge excites ground state xenon atoms to the $6s[3/2]_2$ metastable state. The MOT operates on the cooling transition at 882 nm between the $6s[3/2]_2$ and $6p[5/2]_3$ states. A two-photon process, using the 882 nm photons together with 514 nm photons from a pulsed laser, ionizes the xenon atoms to create a neutral plasma.

MOT to put atoms back into the trapping cycle after they decay into a hyperfine level not coupled to the trapping laser [35]. Furthermore, ^{132}Xe is the most abundant isotope of xenon with natural abundance of 26.89% resulting in faster MOT load times than other isotopes (less load time to get the same MOT density). It is relatively straightforward to create UCPs by two steps. The first uses laser cooling and trapping techniques to collect a sample of cold atoms in a magneto-optical trap (MOT). The second photoionizes the trapped atoms to produce a neutral plasma whose initial density and energy can be controlled by varying the photoionizing laser intensities and wavelengths. Figure 1.2 is the bosonic xenon energy levels. The $5p^6$ is the ground state with an closed shell configuration. The $6s[3/2]_2$ metastable state has a lifetime of about 43 s (much longer than our experimental cycle of 1 s), and serves as the effective "ground state "(like the ground state of alkali atoms) of the cooling transition between the $6s[3/2]_2$ and $6p[5/2]_3$ states. This transition occurs at a wavelength λ of 882 nm with a linewidth $\Gamma = 2\pi \times 5.3$ MHz, and is used to load the atoms into a MOT. A two-photon process, one photon from the 882-nm MOT beams together with one 514 nm photon from a pulsed dye laser, photoionizes the MOT to create a neutral plasma with controlled initial electron energies.

1.2.1 Cooling and Trapping of Metastable Xenon

There are many good resources on the laser cooling and trapping, such as the book "Laser Cooling and Trapping "by Metcalf and Van der Straten [35]. The primary force used in laser cooling and trapping is the recoil when momentum is
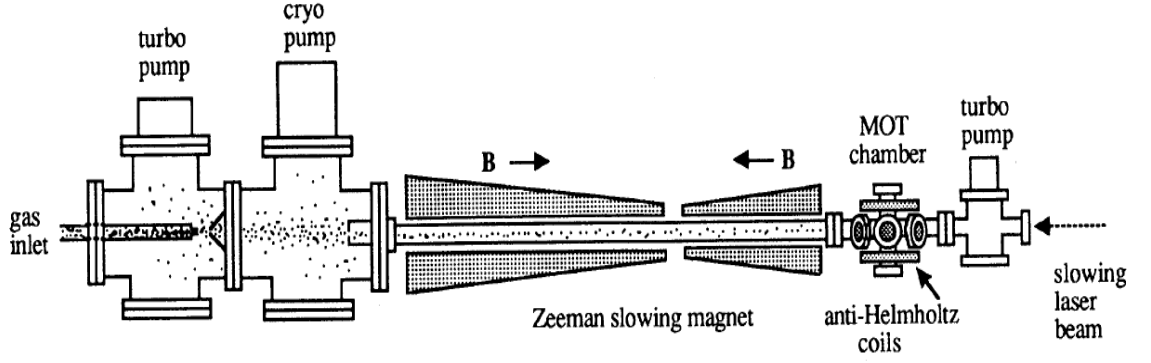
Figure 1.3: Atomic beam and vacuum system for laser cooling and trapping metastable Xe atoms. A metastable xenon beam is created by a DC discharge, collimated by a 1-mm skimmer and a 1-mm aperture, and slowed down by a Zeeman slower. The atomic beam propagates from left to right. The slowing laser beam is in the opposite direction. Diagram from the Ph.D. dissertation of Matthew S. Walhout [36].

transferred from photons scattering from an atom. This radiation-pressure force is analogous to that applied to a bowling ball when it is bombarded by a stream of ping pong balls. The radiation-pressure force is controlled in such a way that it brings the atoms in a sample to a velocity near zero ("cooling"), and holds them at a particular point in space ("trapping"). Much of the information in this section about the apparatus of metastable xenon MOT is described in the Ph.D. dissertation of Matthew S. Walhout [36].

Our metastable xenon beam is created by a DC electric discharge that runs at about -700 V and 2-3 mA, which excites ground state xenon atoms at pressure of about 1×10^{-6} Torr to the $6s[3/2]_2$ metastable state. The beam is then collimated by

10

two 1-mm apertures placed about 1 cm and 30 cm away from the source, respectively, as shown in figure 1.3. The estimated atomic beam in the metastable state has a flux on the order of 10^7 to 10^8 atoms/s. The collimated beam then travels through a Zeeman slower (Figure 1.3), and is slowed down from room temperature velocities (about 300 m/s) to velocities that a MOT can trap (typically 10-20 m/s).

The Zeeman slower consists of a spatially varying magnetic field and a circularly polarized laser beam aligned with the field and propagated in the opposite direction of the atomic beam. The Zeeman slowing laser beam is detuned about 135 MHz below the zero-field, 882-nm transition ($\delta = \omega_{laser} - \omega_{atom} = -2\pi \times 135 \text{MHz}$). It has a 2-cm size as it enters the right side of the Zeeman slower (as shown in Fig. 1.3) and is focused on the skimmer in the metastable source region. The magnetic field varies spatially such that the resonance condition $kv_z + \delta = \mu_B B_z/\hbar$ is always satisfied as the atoms travel through the slower, where $k = 2\pi/(882 \text{ nm})$, v_z is the component of the atom velocity along the axis of the slower (we define the direction along which the atomic beam travels as +z) and μ_B is the Bohr magneton. The atoms absorb photons from the beam, emit photons in random directions and decelerate. However, as their velocities are reduced, The Doppler shift is changed, so the Zeeman shift must be varied such that the atoms are kept in resonance the entire time they traverse the Zeeman slower (per the equation above, the Doppler shift plus the detuning of the laser beam is always equal to the Zeeman shift). The atoms decelerate continuously until they reach the end of the slower, where the velocities are approximately 10-15 m/s. At this point the slowed atomic beam enters the experimental chamber of the vacuum system and is aligned such that the beam

passes through the center of the MOT region.

The particular Zeeman slower in this apparatus uses a reversed-coil configuration. The field is approximately 160 Gauss at the beginning of the slower (left side), crosses zero at about a meter away along the slower and reverses direction, until it reaches -65 Gauss at the end of the slower (1.5 meters from the start of the slower, where the sign is relative to +z direction) [36]. This is done by using two coils - the slower coil, providing the larger, positive field and running at about 35 A, and the reverse slower coil, providing the smaller, negative field and running at about 4.2 A. There are several advantages of the reversed-coil configuration. First, a much smaller maximum field (160 G) can be used since the total change in magnetic field is distributed over positive and negative values comparing to the case (225 G) that the minimum field is zero. This greatly reduces the power dissipation in the most densely wound part of the coil. Second, the MOT loading geometry is more favorable because it allows detuning the slower laser beam by a large value (about 26 Γ in our case) so that it is not resonant with the zero-field transition the MOT uses. Thus the MOT can lie directly in the slower beam's path and be virtually unaffected by its presence; if the minimium field of the slower is 0 G at the end of the deceleration process, it is clear the slower laser would need to have a nearly 0-MHz detuning to compensate for the low-velocity Doppler shift at the end of the slowing process. In this case, the slower beam would resonantly push low velocity atoms, preventing MOT loading on the axis of the Zeeman slower. Finally, the sharp change in field gradient at the end of the coil causes rapid decoupling of atoms from the resonant slowing process and minimizes off-resonant scattering. This allows us to fine-detune

12

the final velocity of the slowed atoms by adjusting the minimium value of the field. These last two features (loading geometry and velocity tunability) facilitate efficient capture of slow atoms by the MOT.

As the slow atoms pass the Zeeman slower stage, they are collected in the MOT, which consists of six laser beams (three counter-propagating pairs) arranged on three orthogonal axes with proper polarization configuration, as well as a quadrupole magnetic field with a zero-field point at the intersection of the laser beams.

The interpretation of the forces and spacial confinements in a MOT is shown in Fig.1.4. For simplicity, we consider atoms that have a ground state with the total angular momentum $J_g = 0$, and the excited state with the total angular momentum $J_e = 1$, illuminated by a red-detuned σ_+ beam from the left and σ_- beam from the right. The magnetic field is zero at the origin ($z = 0$), increases linearly in the positive z direction and decreases linearly in the negative z direction. Becuase of the Zeeman effect, the excited state splits into three state with $m_e = +1, 0, -1$, which have the spatial dependence as shown in Fig.1.4. If atoms move to the $z > 0$ region, where the laser frequency is close to the $m_e = -1$ state, it will absorb more photons from σ_- beam and transfer to the $m_e = -1$ state. Thus scattering force on the atom pushes the atom back to the zero of the magnetic field. For the same reason, the atoms moving to the $z < 0$ region will absorb more photons from σ_+ beam and transfer to the $m_e = +1$ state, and again the atom is pushed toward the center where the magnetic field is zero.

Besides the Doppler cooling (as shown above in 1-D case) by which the lowest achievable temperature (often called the Doppler temperature) is about 120 μK, the

13
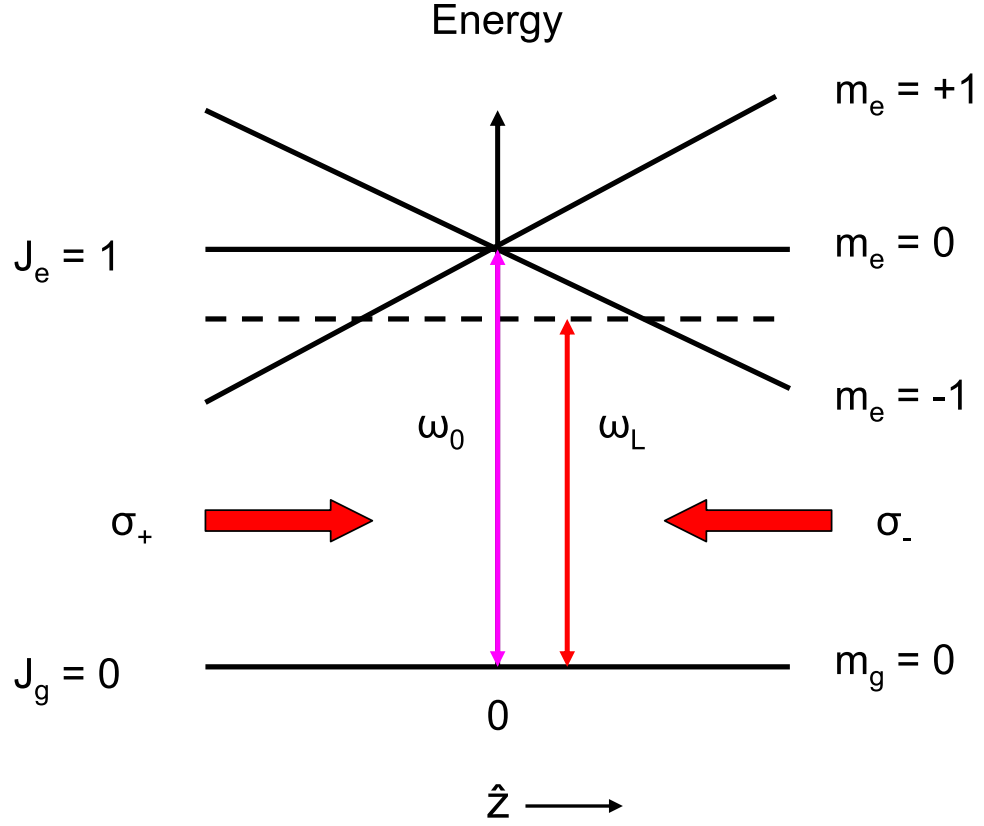
Figure 1.4: Schematic of the one-dimensional MOT mechanism. ω_0 is the zero-Gauss 882 nm transition, while ω_L is the MOT laser frequency (red-detuned about 5 MHz ($\sim 1\ \Gamma$) from ω_0). The $m_e = \pm 1$ sublevels of the excited state shift due to the linear magnetic field gradient. An atom moving to $z > 0$ region has an excited energy level corresponding to the $m_e = -1$ curve due to the MOT magnetic field (not shown); such an atom is closer to resonance with the σ_- beam than the σ_+ beam, so it preferentially absorbs photons from the σ_- beam and is thus pushed back toward the center of the trap z = 0.

cooling has a lower bound determined by polarization gradient cooling effects [35]. Polarization gradient cooling is essentially an enhancement of that scattering rate (due to optical pumping of atoms into the m-sublevels that enhance scattering rates of photons from the beam the atom is moving into) and gives a lower bound on the MOT temperature of $\sim 10~\mu$K for metastable xenon.

The MOT can be realized in three dimensions if we superimpose three orthogonal one-dimentional traps as shown in Fig.1.5. The quadrupole field has a gradient of about 5 G/cm. Each beam is derived from a single Ti:sapphire laser at 882 nm (detuned about 5 MHz from the zero-field $6s[3/2]_2$ to $6p[5/2]_3$ cooling transition and locked to this transition using saturated absorption spectroscopy in a xenon gas cell where metastable xenon is produced by a radio-frequency inductively coupled plasma (RF-ICP)). Each MOT beam is about 2 cm in diameter and with about 8-10 mW per beam; each beam is circularly polarized such that atoms moving into a beam are Zeeman shifted into resonance with that beam. Note that the original MOT configuration in this system used three retro-reflected beams to create the total six beams; the current configuration uses four independent beams plus one retro-reflected beam. The reason for this beam configuration is due to geometries in the vacuum chamber; because we have wire-mesh voltage grids close above and below the plasma, four beams must pass through grids, such that retro-beams on those axes will be unbalanced (the forward beam is attenuated by the grids one time, while the retro beam passes through the grids three times before reaching the MOT region). However, we can retro-reflect along the third axis, as it passes between the grids and is not attenuated by them. We couple each of these beams

15
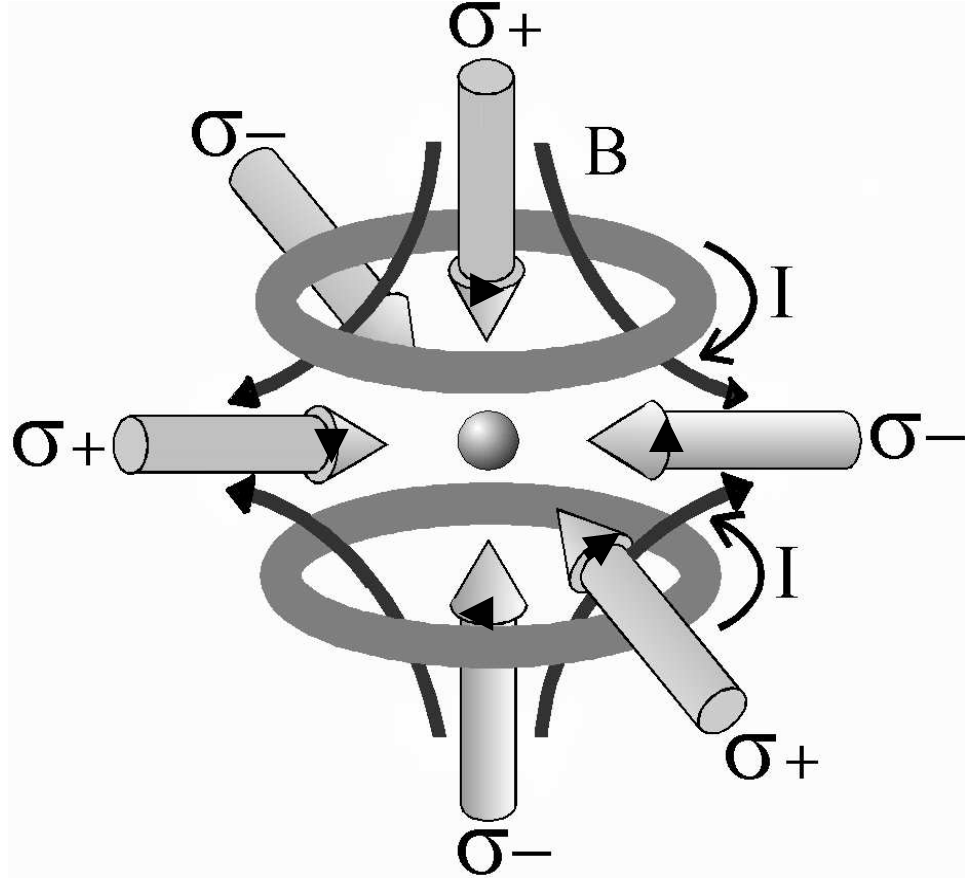
Figure 1.5: Schematic diagram for a three dimensional MOT configuration. A pair of magnets coils has anti-Helmholtz configuration (the coils are coaxial and the direction of current in the upper coil and the lower coil is opposite.). The resulting zero magnetic field is at the midpoint of the axis of the coils.

into a polarization-maintaining fiber; on the output side of each fiber, we expand and circularly polarize the beams before they reach the MOT region.

The MOT is usually loaded for approximately 800 ms since it reaches a steady state after about 500-600 ms. The peak MOT density is limited by collisions between metastable atoms, which leads to Penning ionization (a density-dependent process (more atoms, more collisions) where two metastable atoms collide, ionizing one and de-exciting the other as $Xe^* + Xe^* \rightarrow Xe^+ + Xe + e^-$, thus losing both atoms from the MOT as the ground state atoms and ions can not be trapped by the MOT). It should be noted that this Penning ionization process can be utilized as a MOT diagnostic in this system, since the charged particles can be easily detected and used as a rough guide for optimizing the MOT size and density. The resulting atom cloud has a three-dimensional Gaussian density distribution. Typical parameters for the trap, as measured by time-of-flight and absorption imaging [37], are given in Table 1.1.

Table 1.1: Magneto-Optic Trap (MOT) Parameters

Parameter	Abbreviation	Value
Temperature	T	$\sim$20 μK
Total number	N	5×10^6
Peak Density	n_0	2×10^{10} cm^{-3}
Radius	σ	280 μm

1.2.2   Creation of the Ultracold Plasma

After the trap loading has reached a steady state condition, we photoionize the sample using a two-photon excitation process [1]. One photon for this process is from the cooling laser at 882 nm, which is shifted onto resonance for the zero-field $6s[3/2]_2$ to $6p[5/2]_3$ transition, and the other one is from a 10-ns pulsed dye laser at 514 nm with a bandwidth of ~ 0.1 cm^{-1}, which is pumped by the third harmonic at 355 nm of a pulsed Nd:YAG laser with a repetition rate of 10 Hz and power of 200 mJ/pulse. The pulsed dye laser is about 20-40 mJ/pulse with a beam diameter of about 0.5 cm, and is focused to about 1.5 mm in diameter at the MOT position (about a factor of 3 larger than the MOT size to ensure the uniform power over the atomic cloud), which can ionize up to 30% of the MOT population.

The entire experiment is synchronized with the 10-Hz pulsed Nd:YAG laser, so it is quite easy to synchronize the 514-nm laser and 882-nm laser pulses. The experimental cycle is 1 Hz, so that only one out of the ten pulses per cycle is used for photoionization; the other nine pulses are blocked with a copper-plated mechanical shutter placed between the Nd:YAG and the dye laser to increase the effective dye lifetime (The Nd:YAG laser is powerful euough to burn through the copper shutter, so we need to replace it every everal months). The 882-nm pulse can be switched on in nanosecond by switching the AOM and is usually set to be longer than the 10-ns 514-nm pulse, so that any jitter in the timing electronics will have negligible effect on the photoionization process; while these timings vary, we often set the 882-nm pulse to be about 100 ns in duration with the 514-nm pulse centered at the 50-ns
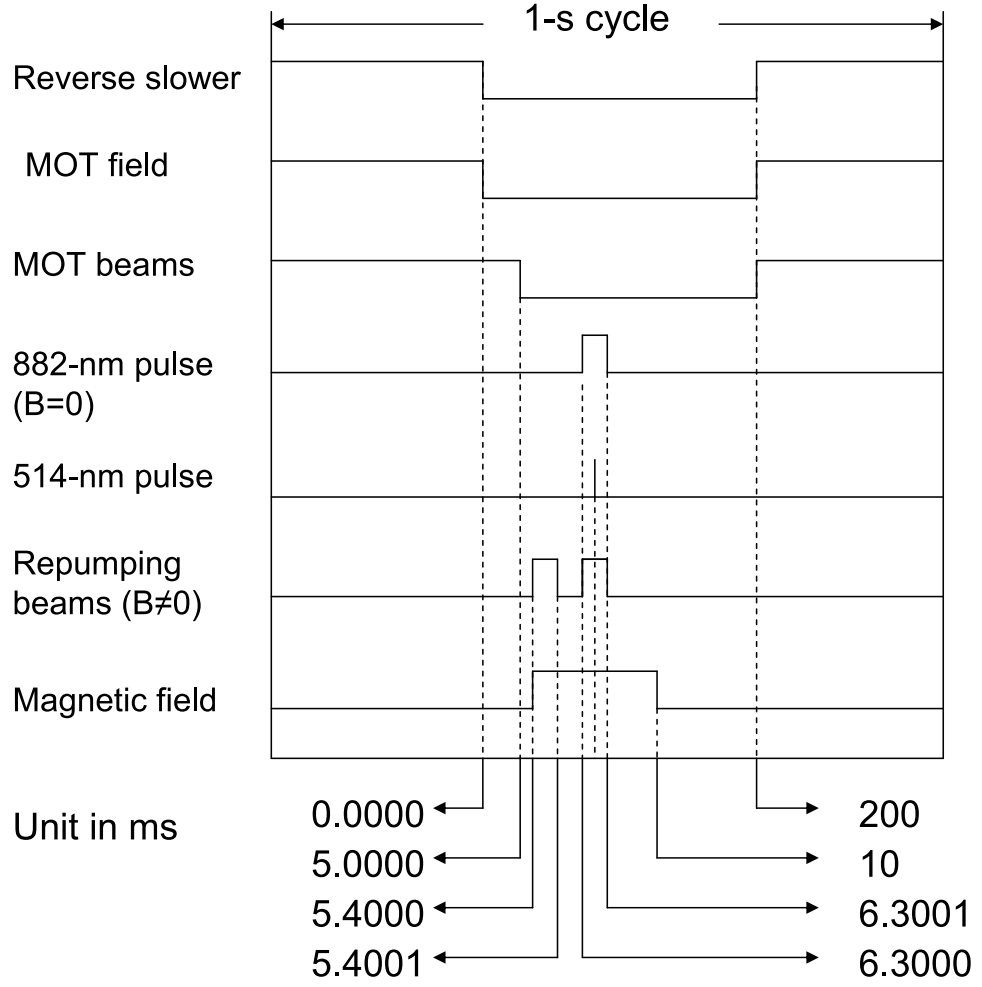
Figure 1.6: The timing sequence for creation of the metastable xenon plasma. The reverse slower, MOT field and MOT beams, cool and trap neutral metastable xenon atoms and then they are turned off. A 5-ms delay in MOT beam, comparing to the MOT field (optical molasses phase), is introduced to further cool the MOT. An optical pumping beam excites the atoms to a higher lying state and the photoionizing beam, which overlaps with the time of arrival of the optical pumping beam, ionizes these excited atoms. In the presence of a magnetic field, we need to turn on the field before the photoionization. All the units are in ms.

point. Figure 1.6 shows the timing sequence for creation of the metastable xenon plasma with or without a magnetic field.

Without a magnetic field, we can simply use the MOT beams which can shifted onto resonance for the the zero-field $6s[3/2]_2$ to $6p[5/2]_3$ transition to drive the $6s[3/2]_2$ to $6p[5/2]_3$ transition to create UCP; with the addition of a magnetic field, the $6s[3/2]_2$ and $6p[5/2]_3$ states split into 5 and 7 Zeeman sub-levels respectively, shifting the transitions out of resonance. To maintain a reasonable excitation fraction, we need to optically pump the atoms into the m = 0 magnetic sublevel of the ground state and then drive the $6s[3/2]_2$ (m = 0) $\rightarrow$ $6p[5/2]_3$ (m = 0) transition, which will be unaffected by the magnetic field to first order. (We cannot turn on magnetic fields in a time short compared to 1 μs that ions acquire velocity in the plasma due to electron pressure ($\sim$ 1 μs). Thus we must photoionize in the presence of the field). It is difficult to accumulate a large m = 0 population via optical pumping for a $J \rightarrow J + 1$ transition, so we developed a multiple-frequency scheme that uses Zeeman shifts to address the m = 0 and m = $\pm$ 1 sublevels (Fig.1.7). We use three voltage-controlled oscillators (VCO) to drive a double-pass acousto-optic modulator (AOM) to generate three π-polarized optical pumping beams that are detuned -5, 0, 5 MHz respectively relative to the $6s[3/2]_2$ (m = 0) $\rightarrow$ $6p[5/2]_3$ (m = 0) transition as shown in Fig.1.7. Total power of the three repumping beams is about 9 mW. The 3-frequency scheme is a compromise of a 5-frequency one, which would be optimum since the ground state $6s[3/2]_2$ has 5 Zeeman sub-levels, but it is too complicated (needs several AOMs and more laser power). With the 3-frequency configuration, we can achieve UCP densities of $\sim$ 50% of the zero field

20

Figure 1.7: Two-photon excitation process for an UCP in a magnetic field: one photon (red solid line, π polarized) at 882 nm drives the $6s[3/2]_2$ (m $= 0$) $\rightarrow 6p[5/2]_3$ (m $= 0$) transition, and the other (10-ns pulse) at 514 nm ionizes the atoms in the $6p[5/2]_3$ (m $= 0$) state. The dashed lines are the repumping beams (both blue and red of the $6s[3/2]_2 \rightarrow 6p[5/2]_3$ transition, also π polarized).
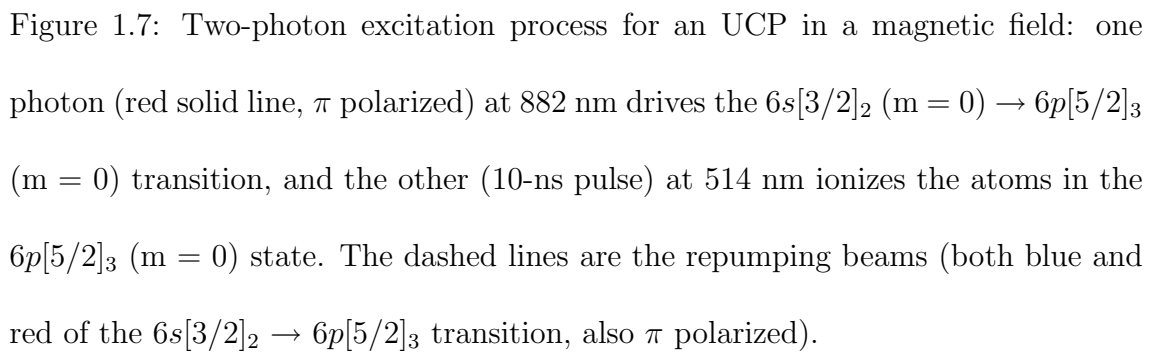
value, approximately independent of magnetic field up to 100 G.

The photoionizing laser can be tuned to provide more energy than is required just to photoionize the atoms. Because of the very small mass ratio between the electrons and ions, the electrons take up most of the extra energy (ΔE) above the ionization threshold in the photoionizing photon (($E_e = \left(\frac{m_i}{m_i+m_e}\right)\Delta$E). This transfer of energy to the electrons leaves the ions at about the same temperature as the MOT atoms (about tens of microkelvin, $E_i = \left(\frac{m_e}{m_i+m_e}\right)\Delta$E, although a large ΔE can result in ion temperatures near 1 mK). Since the initial electron energy is set by the tunable dye laser, it can in principle be as low as the linewidth of the photoionizing laser, which is $\sim$ 0.2 K (although initial electron temperatures effectively end up to be at least 1 K due to fast heating effects immediately after ionization). Typically the initial electron temperature in this study of UCPs is set from 1-500 K. The ions and electrons are not in thermal equilibrium immediately after creation. Various process heat the two species before they reach local equilibrium. A discussion of these processes will be presented later in the text. Immediately after photoionization, the electrons and ions have the same initial distribution of the MOT, their initial density distributions are likewise identical to the original MOT distribution with a multiplicative scaling factor to account for the two-photon ionization efficiency which is up to $\sim$ 30%. The actual number of atoms photionized can be controlled by varying the pulse intensity of the 514 nm pulse.

Typical initial plasma parameters given in Table 1.2.

By using the photoionizing laser, not only can a plasma be created, but atoms with very high values of principal quantum number can be produced by tuning

Table 1.2: Ultracold Plasma (UCP) Parameters

Parameter	Abbreviation	Value
Initial Ion Temperature	$T_i(0)$	$\sim$15-1000 μK
Initial Electron Temperature	$T_e(0)$	1-500 K
Peak Density (r=0, t=0)	$n_i(0,0)$ and $n_e(0,0)$	2×10^9 cm^{-3}
Size	σ	280 μm
Asymptotic Expansion Velocity	v	45-100 m/s

the energy of the laser to slightly below the ionization threshold. These Rydberg atoms [38] play an important role in plasma evolution. Studies have revealed that a dense cloud of ultracold Rydberg atoms can spontaneously evolve into a plasma by blackbody radiation and collisions [39]. Rydberg atoms can be also formed by three-body recombination (TBR), where an ion in a plasma interacts with two electrons and results in a Rydberg atom and an electron, which carries the extra energy [30]. This process plays a significant role in ion loss and electron heating. Thus, the study of Rydberg atoms is necessary in order to get a complete picture of the plasma dynamics, which will be discussed in detail in chapter 2.

1.3 Detection of Ultracold Plasmas

The techniques available for studying ultracold plasmas are relatively limited. Due to the delicate nature of these plasmas (the low temperature, the small size of the sample and the low number of charge carriers ($\sim 10^5$-10^6 ions) and high-vacuum

experimental environment), traditional probes of plasma physics properties are not suitable (such as solid electrode-based probes placed inside the plasma). Instead, they are usually probed by detecting charged particles (measuring the electrons or ions leaving the plasma, both spontaneously and extracted), or using laser spectroscopy (absorption or fluorescence) and imaging for ions with optical transitions. Xenon ions do not have a convenient optical transition from the ground state, as this is deep in the vacuum ultraviolet, so optical imaging techniques are not feasible.

1.3.1   Charged Particle Detection

The primary measurement tool available for our xenon plasma is a multi-channel plate (MCP) detector located approximately 15 cm below the plasma. The MCP is a periodic array of fused thin lead glass capillaries (or channels) sliced into a thin plate. A single incident electron enters a channel, hits a channel wall, and releases secondary electrons. The latter are accelerated by voltages ~ 1500 V applied across the MCP, and produce more secondary electrons. We use a two-stage MCP with a gain in the range of 10^8. The basic idea of charged particle detection is shown in Figure 1.8. When electrons escape from the plasma through an evaporative process (as the plasma expands, the potential due to the ion-electron imbalance weakens, so that the warmer electrons are able to escape), a small electric field created by potentials on two grids (1.5 cm above and below the plasma) directs the escaped electrons to the detector. By reversing the electric field, the MCP can also be used to detect ions, which are emitted from the plasma on a much
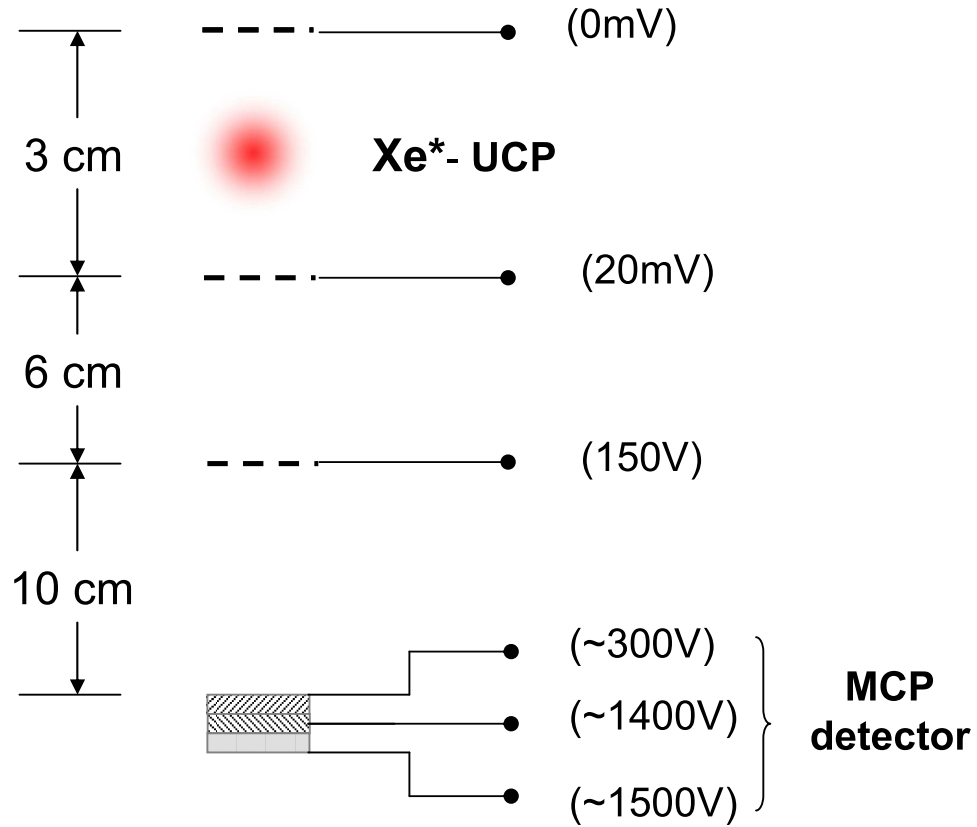
Figure 1.8: A diagram of the charged particle detection and guide grid geometry. The grids immediately above and below are biased at a few mV in such a manner as to attempt to shield the plasma from external fields while still maintaining a slight bias so that emitted particles are directed down toward the MCP. Either of those grids can have RF or microwaves coupled on top of the small DC bias. The middle grid (shown here at 160 V) typically is biased at a few hundred volts to assist in guiding particles to the MCP. The front of the MCP is typically biased at a few hundred volts (often $\sim$ 300 V) and the back of the MCP and the phosphor screen are typically biased at 1300-1500 V.
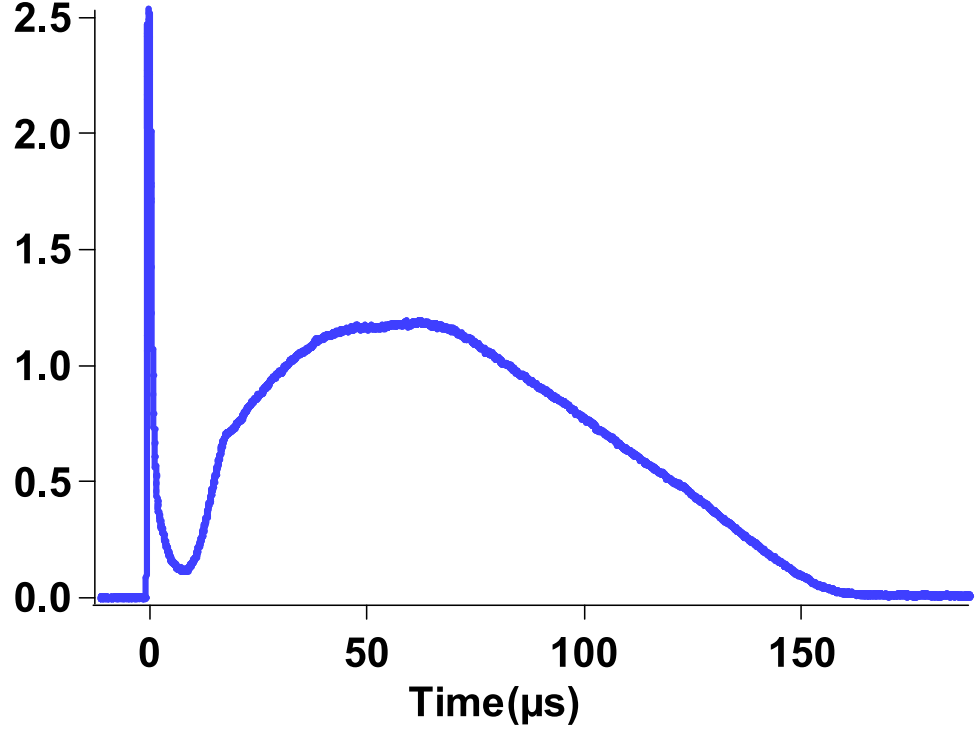
Figure 1.9: A typical electron emission curve using charged particle detection. The plasma is created by photoionization of the Xe^* MOT at $t = 0$ μs. The prompt narrow peak (at $t = 0$ μs) is due to the initial escaped electrons (2-3% of total electrons) immediately after the ionization. The broad peak at late time is due to the electrons spilling from the expanding plasma. The plasma is evolving in a small electric field of 5 mV/cm, which guides the electrons from the plasma to the MCP detector.

longer timescale than the electron emission. The grids can also be used to apply an oscillating radio frequency field to excite plasma collective modes and a microwave frequency field to ionize the Rydberg atoms. A typical electron emission curve using charged particle detection is shown in Figure 1.9. The signal consists of a prompt peak (initially escaped electrons) followed by a region of small electron loss where the quasineutral plasma state forms. This is followed by a long $\sim$150 μs loss of electrons, interpreted as the decay of the plasma as electrons spill out of the potential well, which is getting shallower due to the plasma expansion.

1.3.2 Time-of-flight Projection imaging Detection

Our MCP also has a phosphor screen mounted behind the MCP rear face. The phosphor screen emits a localized fluorescent light burst when impacted by charged particles and allows us to obtain spatial information of the plasma from the position on the detector where charged particles strike. This is potentially more useful than the absorption or fluorescence imaging used in UCPs of other elements, as the MCP technique can be applied to either electrons or ions, and can be used at later times in the plasma expansion when the densities are too low for effective use of the two optical techniques, especially for study the ultracold plasma dynamics in the presence of a magnetic field.

It is critical to project the charged particles as quickly as possible to the detector to minimize the Couloumb explosion effect (described in detail in Chapter 3) during charged particles transport to the detector. We tried to use a high voltage

Figure 1.10: Circuit diagram for a high-voltage pulser. It uses power field effect transistors to fast switch a high voltage source, and is ~ 400 V with a 50-ns turn-on time.
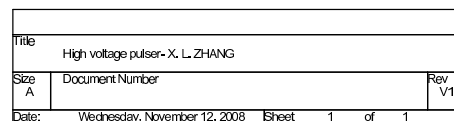
ramp for imaging the ions because there is a high voltage ramp (1000 V, 100 KHz) available in our lab which is used to detect the Rydberg atoms in UCP by field ionization, and we did get ion images with Gaussian profiles. Because the UCP is very sensitive to external electric fields, all the ions left the top and bottom grid region before the ramp reaches its maximum, which corresponds to the effective voltage seen by the UCP about 10 - 20 V, which was too small for good imaging, we used instead a fast square pulse for the projection imaging technique. The high-voltage pulse is modified from a square pulse generator [40], which uses power FETs to fast switch a high voltage source (the circuit diagram is shown figure 1.10). It has an amplitude of 340 V (can be adjusted from 50 to 500 V), a width of 4.5 μs, and a rise time of 60 ns. The key part of this circuit is the transformer, which is necessary for the best square pulse characteristics with very little overshoot, ringing, back-swing, and maximum flap-top droop. It is wound on one Fair-Rite Products Corp's Toroidal core (Part number: 5977001201) with medium permeability materials (materials 77 with initial permeability of $\mu_i = 2000$). The secondary, having 30 turns of AWG 18 magnet wire, is evenly wound on the core first as a first layer; the primary (the second layer) is wound with 15 turns of AWG 18 magnet wire. We can easily change the polarity of the high voltage pulser by exchanging the output pins.

At varying times in the plasma expansion, the high speed, high-voltage pulse is applied to the grid above the UCP. The middle grid is usually biased at about -300 V, and the front of MCP is at about -700 V. The high voltage pulse removes the electrons from the plasma in a few nanoseconds, but does not affect the ions distribution during that short period of time. It then accelerates the ions toward the

MCP in a few microseconds. The ions strike the MCP and the phosphor lights up with an intensity distribution that reflects the spatial distribution of the ions before the time-of-flight. A picture of the phosphor screen is taken by a CCD camera. The resulting image is then fitted using a 2-D Gaussian function, and the resulting size as a function of time is determined (Figure 1.11).
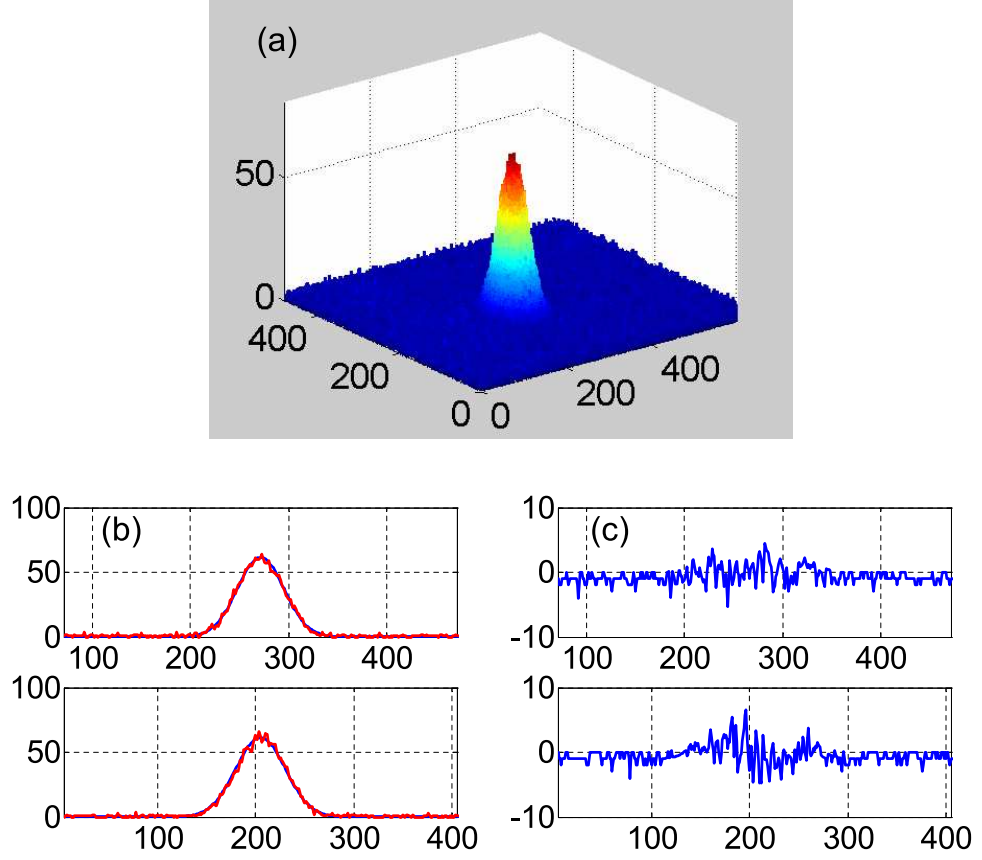
Figure 1.11: Typical ion projection images at 20 μs after the formation of UCP. (a) A false color ion image of an expanding UCP at the delay time of 20 μs for $T_e = 100$ K; (b) 2D Gaussian fitting of the ion image in (a). The red curves are from raw image, and the blue curve are the fitting curves; (c) The residuals between the Gaussian fittings and the ion images in figure (b). All the horizontal units in (a)-(c) are in pixel number, and one pixel unit corresponds to 150 μm.

Chapter 2

Ultracold Plasma Free Expansion and Electron Temperature

Evolution

2.1 Ultracold Plasma Free Expansion

Upon creation of the plasma, the electrons are substantially warmer than the ions ($T_e(0)$: 1-500 K; $T_i(0)$: ~15-1000 μK). The electron cloud then begins to expand, exerting an outward force on the ions. A small number ($\sim$ 2-5%) of electrons escape the plasma, resulting in a slight macroscopic positive charge for the overall system which serves to create a confining potential well for the remaining electrons. When this well depth becomes greater than the average electron kinetic energy, the remaining electrons are trapped, forming a neutral plasma. On the other hand, the potential experienced by the ions has opposite sign, which drives the expansion of the plasma at later times. In an alternative description, the expansion can also be related to the thermal pressure of the electrons on the ions. Since the electrons have high kinetic energy, they tend to leave the plasma cloud. As the electrons leave, the Coulomb force due to the net positive charge in the cloud, pulls the electrons back into the cloud. In this process, the ions face a recoil force in a direction radially outwards. Hence, as the plasma expands, the thermal energy of the electrons gets converted into expansion energy of the ions and causes the

whole cloud to expand radially outwards over time. The expansion dynamics of UCPs are studied experimentally by various methods, such as plasma collective modes [16, 22], optical absorption and fluorescence imagings [13, 14] and time-of-flight projection imaging [41, 42], and are also studied theoretically by a variety of methods [27, 30, 31, 43, 44].

2.1.1   Using Electron Collective Plasma Modes

The first quantitative experimental study of the expansion was performed using excitation of electron plasma oscillations as a probe of the density [16]. The most characteristic aspect of plasmas is perhaps that the charged particles exhibit collective behavior because of the long range Coulomb interaction between the charged particles. Plasma oscillation, in which electrons oscillate around their equilibrium positions and ions are essentially stationary, is a fundamental collective plasma mode first described by Tonks and Langmuir and often refers to cold plasma theory, which neglects finite electron temperature effects. This mode is a valuable probe of plasma expansion because the oscillation frequency depends solely on the electron density.

By applying a radio-frequency field to the top grid (Figure 1.8), we can resonantly excite this collective mode, and use a MCP to monitor the escaped electrons from the plasma [16]. Typical electron emission signals with and without an rf field are shown in Figure 2.1a. The rf field is applied continuously. The plasma is created by photoionization at time t = 0. Some electrons leave the sample and arrive at the detector at about 1 μs, producing the first peak in the signal. The resulting
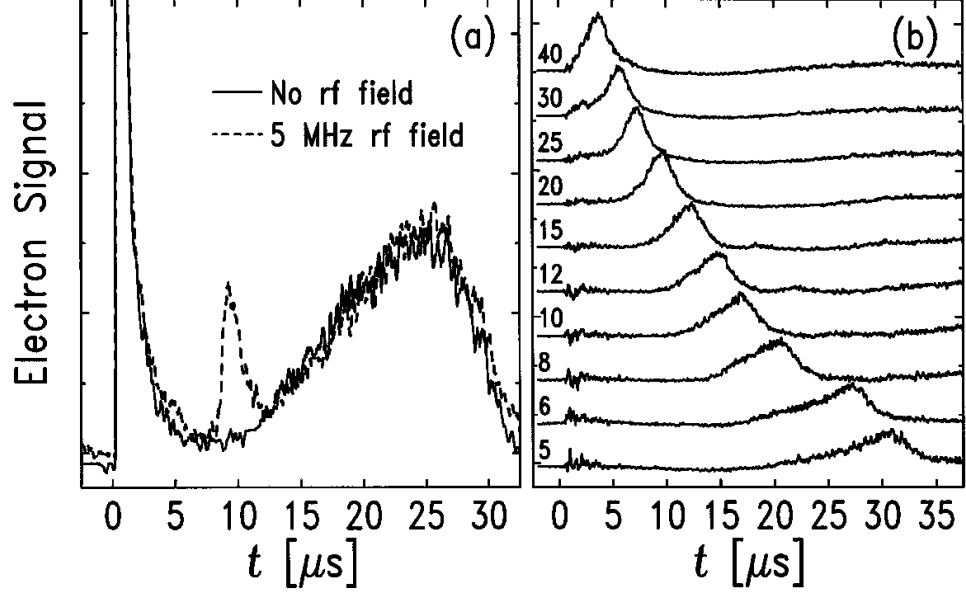
Figure 2.1: Electron signals from UCPs created by photoionization at t = 0 μs. (a) 3×10^4 atoms are photoionized and $T_{e0} = 540$ K. Both signals with and without rf field are shown, and the rf field is applied continuously. (b) 8×10^4 atoms are photoionized and $T_{e0} = 26$ K. For each trace, the rf frequency in MHz is indicated, and the nonresonant response has been subtracted. The signals have been offset for clarity. The resonant response arrives later for lower frequency, reflecting expansion of the plasma. From [16], used with permission.

excess positive charge in the plasma creates a Coulomb potential well that traps the remaining electrons. As the plasma expands, the depth of the Coulomb potential well decreases, allowing the remaining electrons to leave the trap. This produces the broad peak at $\sim 25 \ \mu$s.

An additional peak appears in the electron emission signal in the presence of an rf field (Figure 2.1a), which indicates that resonant excitation of plasma oscillations has pumped energy to the plasma causing more electrons to leave the plasma. If we assume the excited mode in the regions of near resonant density - the average density ($\omega_{pe} = \sqrt{e^2 \bar{n}_e / \epsilon_0 m_e}$), the changing resonant frequency shows the decrease in plasma density with time as the plasma expands into the surrounding vacuum (Figure 2.1b).

Figure 2.2 shows the average plasma density as a function of time when the peak response arrives. It is well described by a self-similar expansion of a Gaussian cloud with $\bar{n} = N / \left[4\pi (\sigma_0^2 + v_0^2 t^2) \right]^{3/2}$, where σ_0 is the initial rms radius, v_0 is the rms radial velocity at long times, and $\bar{n}$ is the density in resonance with the rf field, which is assumed to equal the average density of the plasma. That is, the ballistic expansion of plasma size is valid ($\sigma(t) = \sqrt{\sigma_0^2 + v_0^2 t^2}$), which is a self-similar solution of the Vlasov equation for a spherically symmetric plasma [2, 16]). The extracted values of σ_0 are equal to the size of the initial atom cloud, and the extracted values of v_0 for different initial electron temperatures are shown in Figure 2.3.

For an initial temperature $T_{e0} \geq 70$ K, the expansion velocity approximately follows $v_0 = \sqrt{k_B T_{e0} / \alpha m_i}$, with $\alpha = 1.7$, the ion acoustic velocity due to the electron pressure on the ions, which agrees with a simple hydrodynamic electron pressure

35
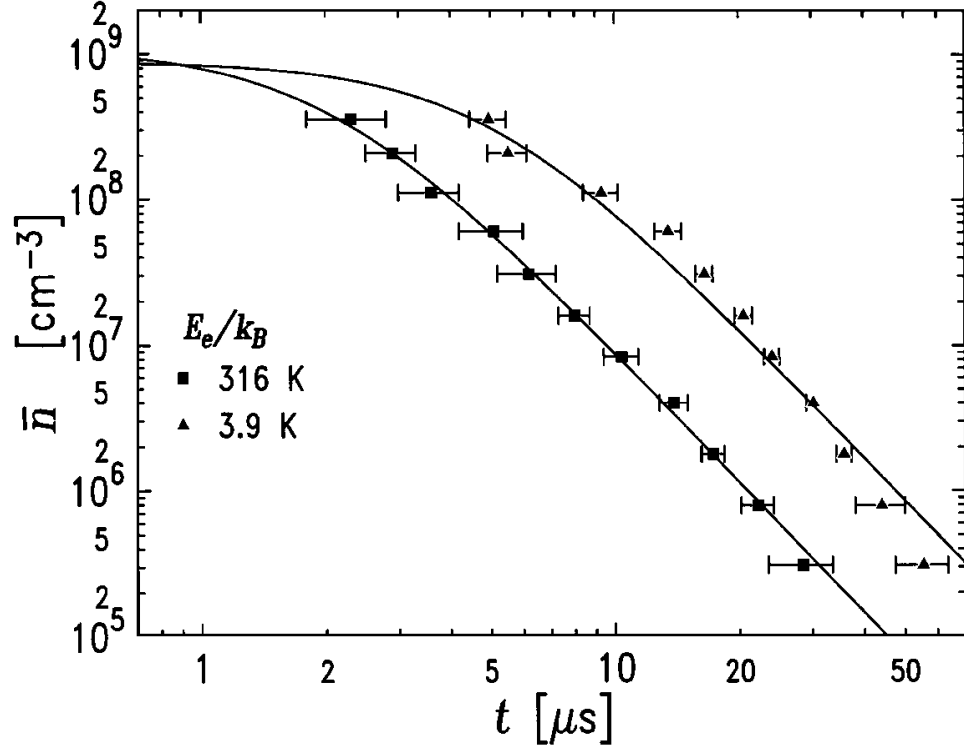
Figure 2.2: Expansion of the plasma for $N = 5 \times 10^5$ photoionized atoms. The expansion is well described by $\bar{n} = N/\left[4\pi(\sigma_0^2 + v_0^2 t^2)\right]^{3/2}$, where σ_0 is the initial rms radius, v_0 is the rms radial velocity at long times, and $\bar{n}$ is the density in resonance with the rf field, which is assumed to equal the average density of the plasma. Horizontal error bars arise from uncertainty in peak arrival times in data such as Fig. 2.1. The fits are consistently poor at low T_{e0}, as in the 3.9 K data. From [16], used with permission.

36
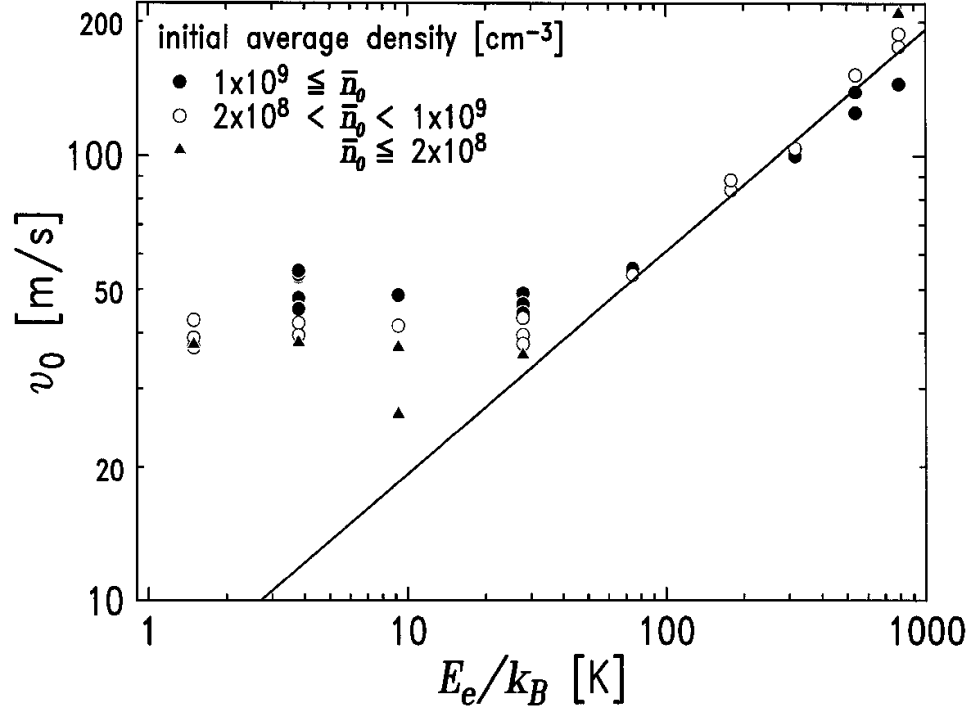
Figure 2.3: Expansion velocities v_0, found from fits to data such as in Fig. 2.2, as a function of different initial electron temperature T_{e0}. The initial average density $\bar{n}_0$ varies from 6×10^6 to 2.5×10^9 cm^{-3}. The solid line, $v_0 = \sqrt{k_B T_{e0}/\alpha m_i}$, with $\alpha = 1.7$, is a fit to data with $T_{e0} \geq 70$ K. The behavior of low T_{e0} data is discussed in the text. Uncertainty in v_0 is typically equal to the size of the symbols. There is a 0.5 K uncertainty in T_{e0} reflecting uncertainty in the dye laser wavelength. Note that for $T_{e0} < 70$ K, v_0 shows a systematic dependence on $\bar{n}_0$. From [16], used with permission.

model assuming quasineutrality and self-similar expansion. At low initial temperature, the UCPs expand faster than expected from the self-similar expansion model, which indicates that there are extra heating effects such as three-body recombination driving the expansion (discussed in the next section) [16, 31].

When applying an rf field to the plasma, not only can it excite the cold plasma resonance (plasma oscillation), but it can also also excite a series of resonances that we identified as Tonks-Dattner (TD) resoances [45, 46] (as shown in Figure 2.4). These TD resonances arise from finite-temperature effects in an inhomogeneous finite-sized plasma. Recalling the cold plasma resonant frequency (with the local approximation):

$$\omega_p^2(r) = \frac{n_e(r)e^2}{\epsilon_0 m_e} \tag{2.1}$$

By including the effect of the electron temperature, the resulting dispersion relationship takes the following form [47], which is often called Bohm-Gross dispersion relation:

$$\omega_i^2 = \omega_p^2(r) + \frac{3k_B T_e}{m_e} k_i^2(r) \tag{2.2}$$

where $k(r)$ is the local wave number and $\omega_p(r)$ is the local plasma frequency from eqn 2.1, assuming a local density approximation. Thus as T_e (or k) $\rightarrow$ 0, the plasma wave has frequency ω_p (the cold plasma result), and high T_e or k results in a linearly dispersive wave (that is, an electron acoustic wave) in the plasma. It is at first surprising that thermal effects are important in UCPs. But because of the small plasma size, the wavelength of density waves must be small and the wavevector

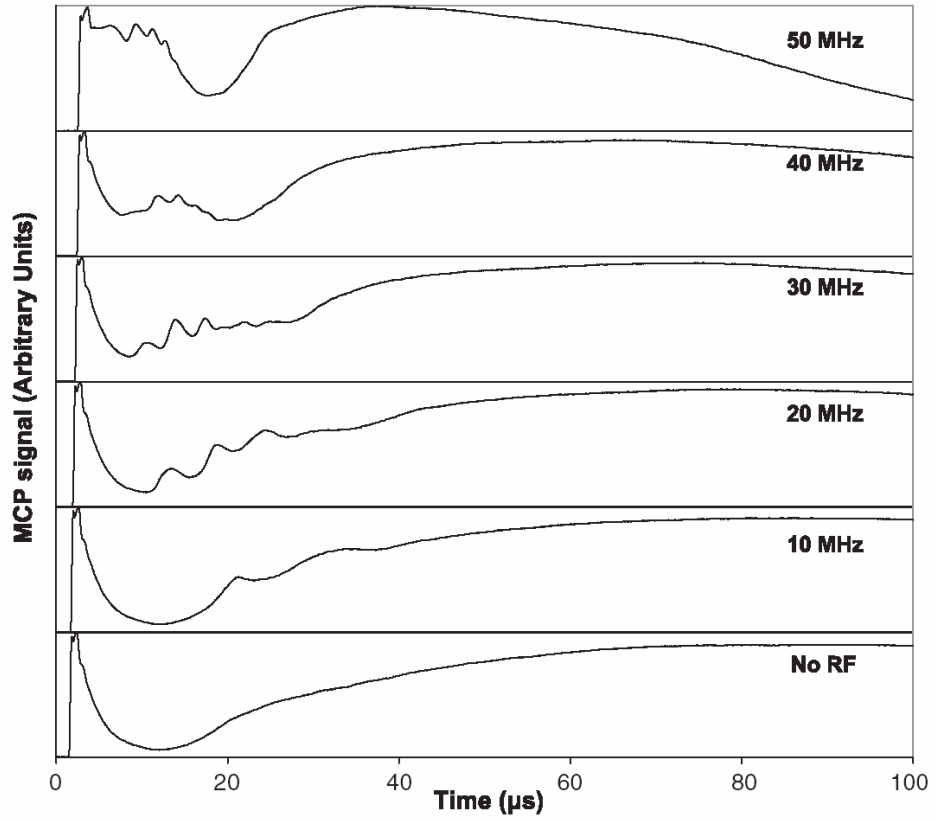Figure 2.4: Example of electron emission signals with Tonks-Dattner resonances due to the external rf fields. rf electric fields with the noted frequencies are applied to the expanding plasma (more dense than [16]), yielding distinct peaks that depend on frequency. For a given rf frequency, the earliest peak is the cold plasma mode as described above, the later modes are the Tonks-Dattner resonances.

must be large. This makes the thermal term (the second one) in the Bohm-Gross dispersion relation (2.2) comparable to $\omega_p(e)$.

Physically, these TD resonances are simply standing acoustic waves in the electron system with frequencies determined by the dispersion relationship of eqn 2.2. The inner turning point for the standing wave is the radial distance r_c where the local plasma frequency $\omega_p(r)$ is equal to the frequency of the standing TD wave; at radii less than this, the plasma frequency is greater than the TD wave frequency, so the wave cannot propagate into the core of the plasma and is evanescent in this region. The outer turning point r_w is not so clearly defined as r_c (previous laboratory observations of these TD resonances were done in cylindrical plasmas with well-defined walls) and is addressed in the following paragraphs. Using this concept of a standing wave, and adapting the work of [48] for application to a spherical system, one can simply find mode frequencies by using the WKB method [49] for the pressure theory (resulting in the expression $\bigtriangledown^2 \delta n(r) + k^2(r)\delta n(r) = 0$ for the density fluctuation $\delta n(r)$):

$$\text{Tan}\Big(\int_{r_c}^{r_w} k(r)\ dr\Big) = \frac{r_w}{2}(k(r_w)), \omega_p(0) < \omega \tag{2.3}$$

$$\int_{r_c}^{r_w} k(r)\ dr = (i + \frac{1}{4})\pi, i = 1, 2, 3, \cdots, \omega_p(0) > \omega$$

where $\omega_p(0)$ corresponds to the peak plasma density.

Since $k^2(r) = [\omega_i^2 - \omega_p^2(r)]/(3k_B T_e/m_e)$, we can numerically solve Equations 2.3 to determine the resonant frequency ω_i. We assume a spherically symmetric
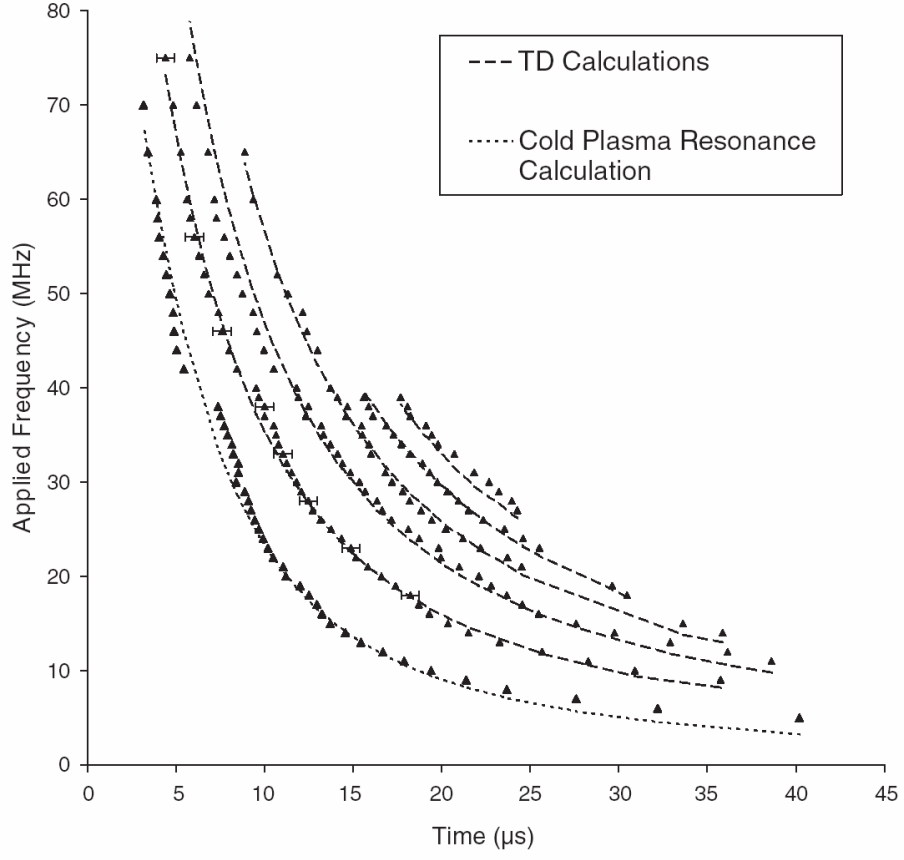
Figure 2.5: Mode frequencies as a function of time. The data have errors at all points approximately the same as the representative error bars. Dashed lines are Tonks-Dattner theory fits with $T_e = 19$ K, $n_0 = 1.9 \times 10^9$ cm^{-3}, and expansion velocity $v_0 = 65$ m/s. The dotted line is a cold plasma theory fit with $n_0 = 1.9 \times 10^9$ cm^{-3}, $v_0 = 65$ m/s, and multiplicative factor of 0.24 scaling the peak plasma frequency. From [22].

Gaussian density distribution with self-similar expansion (per Eq. 2.4).

$$n_e(r,t) \sim n_i(r,t) \sim \frac{n_i(0,0)\sigma_0^3}{\sigma(t)^3} exp[-r^2/2\sigma(t)^2] \qquad (2.4)$$

As mentioned above, r_c is the well-defined inner turning point for the TD standing waves ($\omega_p(r_c) = \omega_i$). The outer turning point r_w, is a free parameter in our model since there is no physical wall in our system. We choose the "wall" r_w to be 3σ, as this limit of integration for Equations 2.3 is reasonable in that it includes a large portion of the plasma and gives results consistent with our estimated densities and with cold plasma theory. We note that at the 3σ point, the local Debye length $\lambda_D(r)$ is on the order of the size of the plasma σ, where $\lambda_D(r) = \sqrt{\epsilon_0 k_B T_0/e^2 n(r)}$. And also some theoretical simulations predict that there will be an ion shock wave formation around the 3σ point [31, 33].

Using the time-dependent Gaussian density profile and our choice of r_w, we numerically integrate 2.3, with the results shown in Figure 2.5. The lowest frequency mode is given by cold plasma theory. We use a fit to the cold plasma curve and find an expansion velocity of 65 m/s. We adjust T_e and n_0 to fit the generated TD curves to the data (to all data curves except the lowest) and find $T_e = 19$ K and $n_0 = 1.9 \times 10^9$ cm^{-3}, which are well within the expected range of temperature and density for our system. Using this n_0 found by fitting the TD calculations to the data, we fit $\omega_p(0)$ to the cold plasma data curve of Figure 2.5, finding $\omega = 0.24\omega_p(0)$, which is consistent with [43] (it finds a factor of 0.22 for a static Gaussian distribution, and a factor of 0.38 for a time-dependent calculation between the peak response and the peak plasma frequency.), although not necessarily consistent with previous

measurements [16].

For these TD resonances, given a choice of r_w, the temperatures can be well determined; however, since the mode frequencies are dependent on r_w, we do not view this method as a quantitative way to determine T_e. Changing r_w by 10% results in a 20% change in the fitted temperature and as much as a factor of 2 change in the fitted density. This highlights one of the unusual features of expanding UCPs the lack of defined boundary conditions. With the theoretical work on these electron sound waves in our system geometry, these TD modes can be an accurate method to measure the electron temperature evolution and the plasma expansion dynamics since it depends on both temperature and density. Hence, both types of collective electron modes can provide information on the time evolution of the plasma, the changing density and electron temperature and may be used to monitor dynamical effects in the plasma expansion.

2.1.2 Using Optical Imaging Probes

Other groups have studied the expansion of UCPs with optical measurements such as fluorescence and absorption imaging [13, 14]. These methods provide excellent spatial and temporal resolution, and the possibility to follow the entire expansion from plasma formation, through ion acceleration, to final velocity. By using the laser-induced fluorescence of ions in an expanding UCP [14], the expansion can be measured up to 50 μs, and reasonably agrees with a modified version of isothermal fluid model with elliptical symmetry. For initial temperatures < 100 K, the plasma expanded with more energy than expected from the initial electron temperature. By using optical absorption imaging [13], the rms velocity along the laser beam can be extracted from the width of the absorption images for the first 20 μs. For high initial temperatures and low initial density, the rms ion velocities agree with expected values from a self-similar expansion of the plasma which assumes adiabatic expansion, that is, neglecting the three-body recombination and disorder-induced heating of electrons. At low initial electron temperature and high density, similar measurements show that electron heating effects contribute more signicantly and for longer times. The detail information about studying the expansion with optical absorption imaging can be found in P. Gupta's Ph.D. thesis [25].

2.1.3   Using Charged-Particle Projection Imaging

The expansion of UCPs can also be studied with a recently developed method - time-of-flight projection imaging technique. This method can follow the ultra-cold plasma expansion during the whole lifetime (especially later times), while the methods mentioned above focus on the dynamics early in the plasma lifetime (the first 20 μs). More details about the technique and the method of data-analysis are described in Chapter 3.

Briefly, by applying a high-voltage pulse (amplitude about 340 V, width about 4 μs, and rise time about 60 ns) to the top grid and with proper accelerating field on the middle and front grids (figure 1.8), we can image the ion distribution of an UCP onto a position-sensitive detector (a phosphor screen) attached to a micro-channel plate detector. Figure 2.6 shows typical ion projection images with an average of 8 images to increase the signal to noise ratio. One pixel corresponds to about 150 μm. Figure 2.6a is a false color plot of ion image of UCP at the delay time of 20 μs and initial electron temperature $T_e = 100$ K, which is approximately a 2D Gaussian profile (as shown in Figure 2.6b). The red curves are from the raw image, and the blue curves are from the 2D Gaussian fitting curves. Figure 2.6c and 2.6e are the false color ion images at different delay times after the formation of the UCP for $T_e = 200$ K and 10 K, respectively. Figure 2.6d and 2.6f are the corresponding 2D Gaussian fits of 2.6c and 2.6e, respectively. The size of the image first decreases at early times from 0 μs to 20 μs due to the strong Coulomb explosion (discussed in detail in Chapter 3) of the dense ion cloud during the time-of-flight time to the
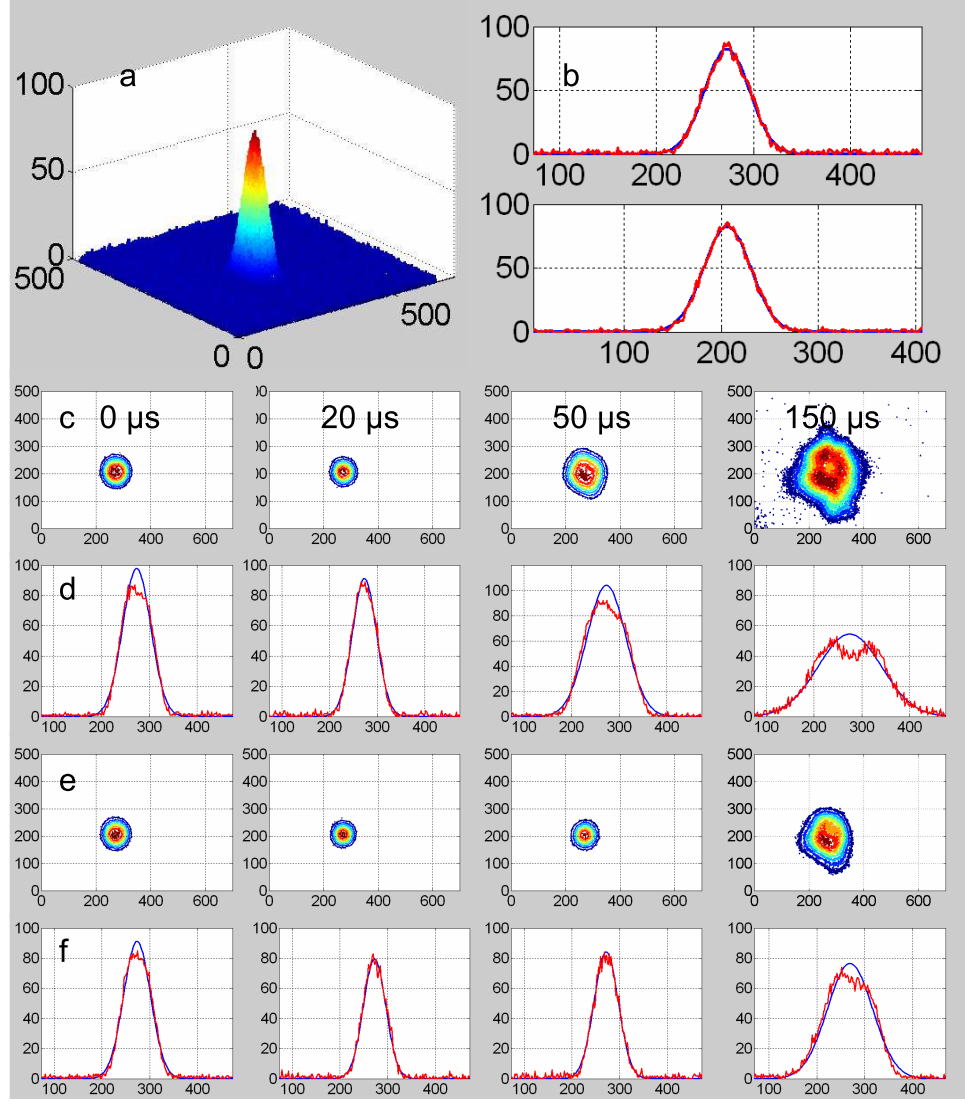
Figure 2.6: Typical ion projection images at different delay times after the formation of UCP. (a) a false color ion image at t = 20 μs and T_e = 100 K; (b) 2D Gaussian fitting of the ion image in (a). The red curves are from raw image, and the blue curve are the fitting curves. (c) and (e) the contour plots of the ion images at different delay times for T_e = 200 K and 10 K, respectively; (d) and (f) the corresponding 2D Gaussian fitings of (c) and (e). All the units in (a)-(f) are in pixel number, and one pixel unit corresponds to 150 μm. From [42].

46
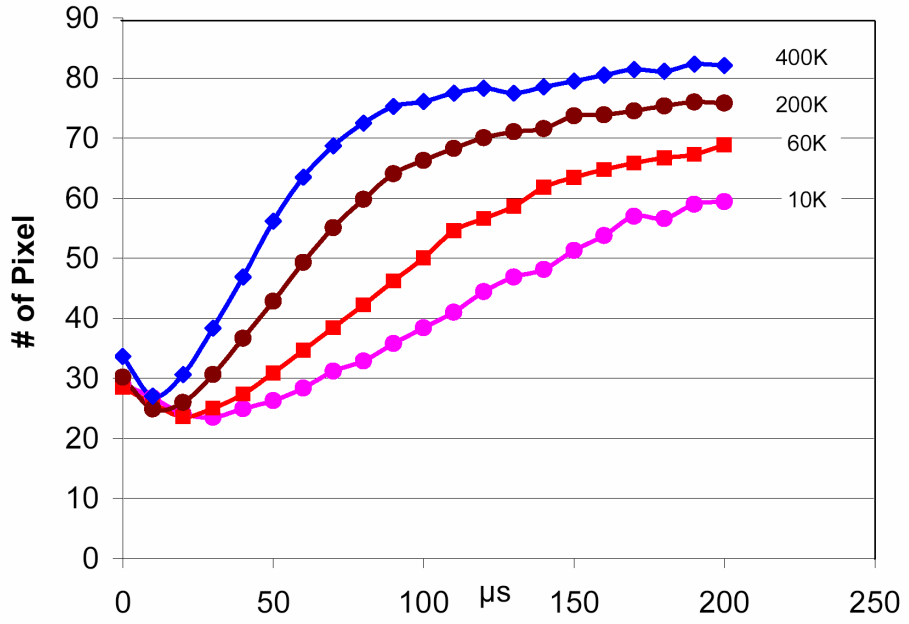
Figure 2.7: The sizes of UCPs as a function of time for different initial temperatures. The curves are for 400 K, 200 K, 60 K and 10 K initial electron temperatures from top to bottom, respectively. Early in the lifetime of the plasma, the size of the image is dominated by the Coulomb explosion of the dense ion cloud. At about 20 μs the image size is at a minimum and then linearly increases, reflecting the true size of the plasma.

detector (which is typically about 8-9 μs) [41]; it then increases afterward with less Coulomb explosion effect due to the expansion of the UCP. The ion images maintain a Gaussian density profile during the whole lifetime of UCP which is about 200 μs as shown in figure 2.6d and 2.6f.

By 2D Gaussian fitting of the ion images (figure 2.6c and 2.6e) at different delay times after the formation of the UCP, we can get the temporal plasma size

evolution. Figure 2.7 is the plasma size as a function of time (the first 200 μs) for different initial electron temperatures. The curves are for 400 K, 200 K, 60 K and 10 K from top to bottom respectively. At about 20 μs the image size is at a minimum and then linearly increases, reflecting the true size of the plasma.

By linear fitting to the sizes after about 20 μs (for higher initial electron temerature, only fitting the linear region), we can get the asymptotic expansion velocities of ultracold neutral plasmas at different initial electron temperatures (the red solid curve with square points in Figure 2.8). At high initial electron temperature($\geq 60K$), the expansion velocities $v_0 \propto \sqrt{\alpha T_e}$, that is, the slope of the red dashed line in Figure 2.8 is 1/2; at lower initial electron temperature ($\leq 60K$), the expansion velocities are higher than expected from the self-similar expansion, which indicates extra heating for the expansion at low initial electron temperatures. The black solid line with circle points is the result obtained by measuring the plasma oscillation frequency [16]. There is a global factor of about 1.5 between our data and the data from reference [16]. This scaling factor is because of the charge particle lensing effect as the ions fly to the detector. This is confirmed by adjusting the voltage settings of grids (especially the middle grid), which changes the ion image size as well as the scaling factor. The good agreement between these two independent methods strongly supports the measurement of UCP expansion velocity by using time-of-flight ion projection imaging and the previous technique.
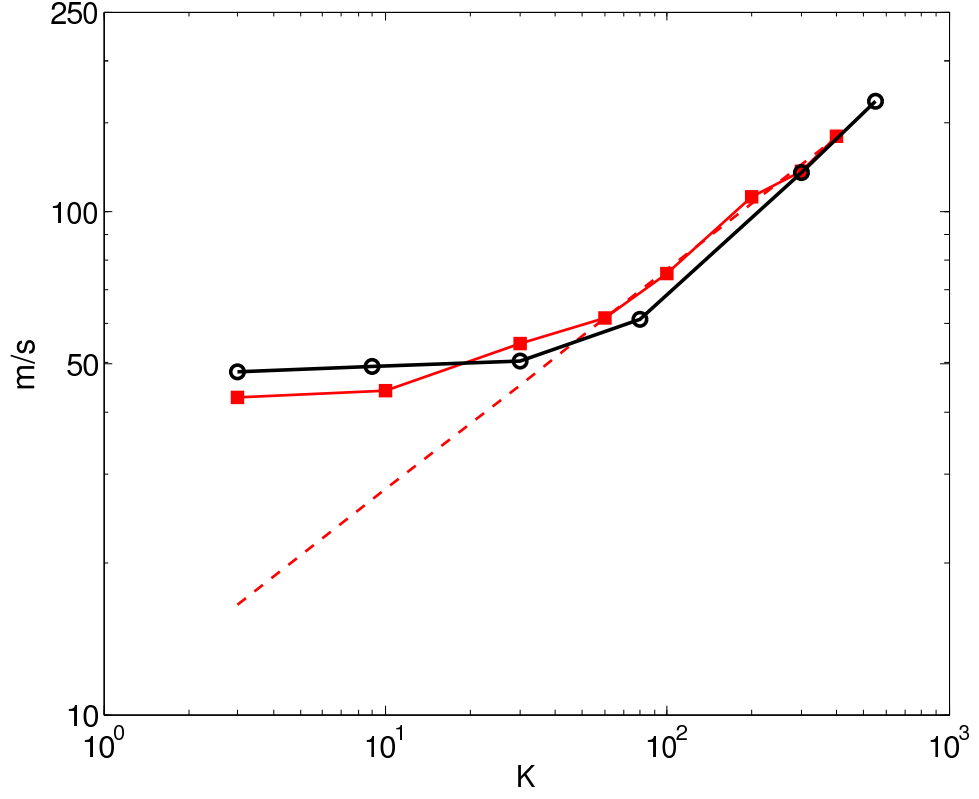
Figure 2.8: The asymptotic expansion velocity as a function of initial electron temperature T_e. The red solid line with square points is the experimental result which matches the results obtained by measuring the plasma oscillation frequency (the black solid curve with circle points)[16]. the red dashed lines is the linear fitting of the data above 60 K with a slope of about 1/2.

2.2 Electron Temperature Evolution

Electron temperature is one of most important parameters in UCPs. Good knowledge of the electron temperature and its evolution is fundamental and critical to the understanding of UCPs. Measurements of the electron temperature can test molecular dynamics simulation of UCPs. Furthermore, three-body recombination is a fundamental collisional process in plasmas and the dominant one at sufficiently low electron temperatures due to its $T_e^{-9/2}$ dependence. Measurements of the electron temperature can help us verify the three-body rate expression at very low temperatures. Finally, knowledge of the electron temperature is necessary to determine whether the electrons are in the strongly coupled regime.

The electron temperatures are expected to be influenced by a wide variety of effects. The electrons are subject to very early disorder-induced heating which was first observed in the ion system of an UCP with a optical absorption imaging probe by Chen *et al.* [19] and slow (and incomplete) equilibration with the ions. The fast heating process can be understood as follows: immediately after the photoionization, the system is far from equilibrium and the charged particles are spatially uncorrelated due to the initial random positions of atoms in the MOT. As the ions and electrons shift to minimize the local Coulomb interaction, correlations develop and potential energy is converted into (thermal) kinetic energy. This leads to an effective lower bound on the $t = 0$ electron temperature of a few Kelvin regardless of how small we set the surplus energy in the photons. Furthermore, there is also some heating due to the creation of Rydberg atoms by three-body recombination,

and the subsequent Rydberg-electron collisions can further influence the electron temperature. On the other hand, as the plasma expands, the electron system undergoes adiabatic cooling, because the expansion is driven by the electron pressure on the ion system (that is, the electron energy is transfered to the ion kinetic energy). Throughout the expansion of the plasma, hot electrons leave the system, resulting in an evaporative cooling effect. So there is a competition between strong cooling and a heating process that rapidly turns on as the temperature falls, and an uncertain evolution of the electron temperature and Coulumb coupling parameter.

Direct measurement of the electron temperature in UCPs is a quite challenging problem. This is largely due to the nature of the UCP system; given its small size (several hundred micrometers) and low number of charge carriers $\sim$ 500,000 electrons at creation), the use of standard plasma probes is not feasible. Instead, new techniques must be developed and employed to extract information regarding this particular plasma parameter.

2.2.1 Electron Spilling Technique

The first electron temperature as a function of time was directly done by tipping the confining Coulomb potential and measuring the fraction of electrons that escaped from the lower potential barrier by applying a small electric pulse [23]. That is, the electric field creates a saddle point that allows electrons above particular energies (the hot tail of a Boltzmann distribution) to leave the plasma. The electron temperature can be extracted from the fraction of spilled electrons as a function of
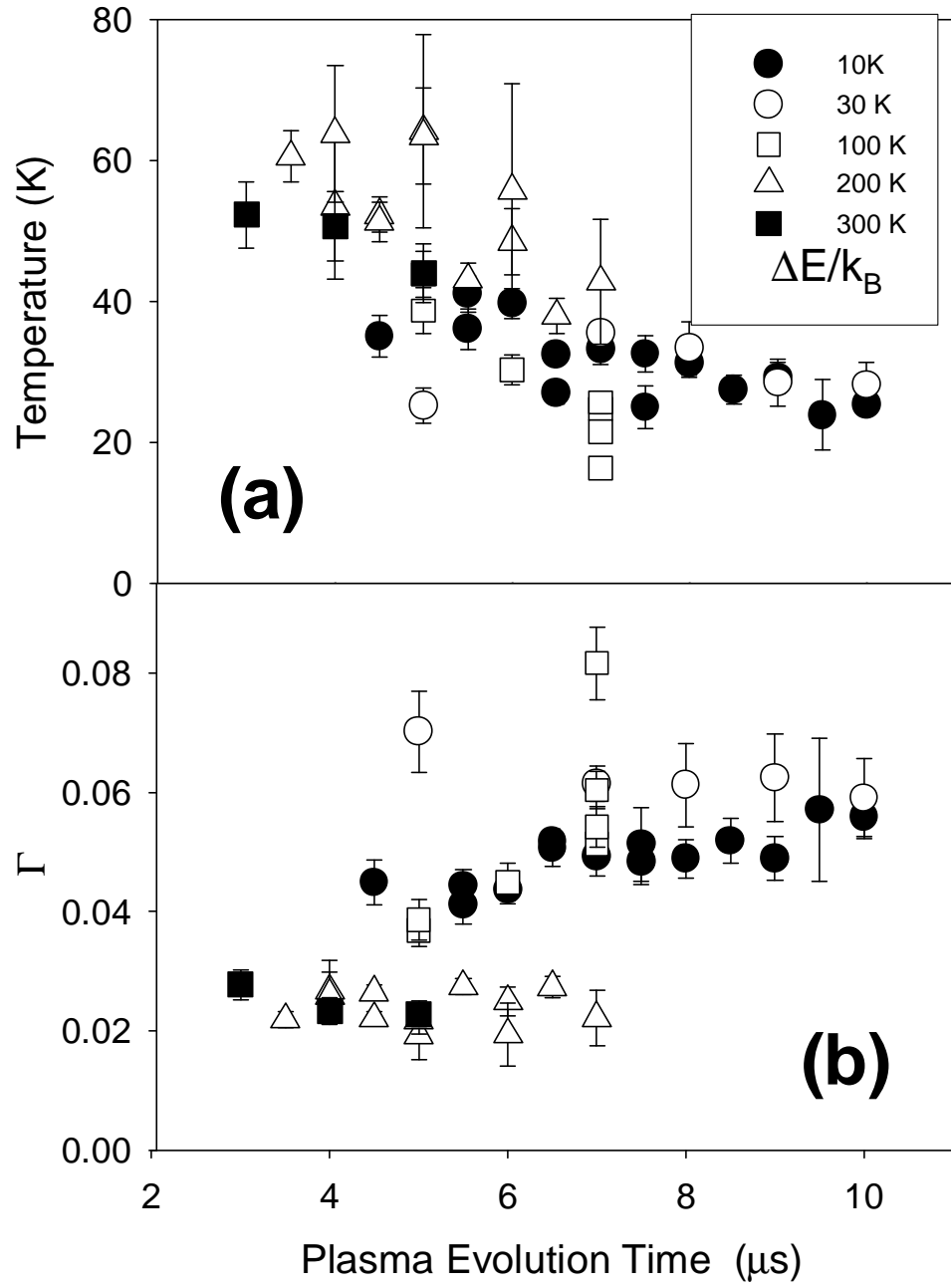
Figure 2.9: Measured time evolution of electron temperature (a) and electronic Coulomb coupling parameter (b) for different initial electron temperatures. From [23], used with permission.

the tipping electric field by assuming the far-field electron potential proportional to 1/r. Figure 2.9 shows the electron temperature and the electronic Coulomb coupling parameter over a wide range of initial electron temperatures. Competition between heating and cooling mechanisms tend to bring plasmas to similar electron temperatures ($\sim$ 60 K) after several microseconds, and the electron temperature subsequently dropped over in the next 10 μs along a similar curve regardless of the initial conditions, and the electron Coulumb coupling parameter remains less than 1 all the time.

However, this technique is only applicable early in the plasma lifetime (3-10 μ s); after about 10 μs, the emitted electron signals are no longer valid to determine the electron temperature; this is because after this time, the plasma has expanded to sizes large enough that the saddle point created by the spilling field is in the 1/r part of the plasma potential (that is, the far-field potential), violating the assumption of the model to extract the electron temperature. Furthermore, since the electrons in this finite potential obviously cannot have a true Maxwell-Boltzmann distribution, this technique requires careful modeling of the plasma density distribution and appropriate treatment of the truncated Maxwell-Boltzmann distribution as well as the proper calculation of the density of states, such that the temperature meansurements have fairly large uncertainties associated with them.

2.2.2 Using Three-body Recombination Rate

Three-body recombination (TBR), in which an electron and an ion recombine to form a highly excited Rydberg atom while a second electron participates in the collsion to conserve energy and momentum ($e^- + e^- + Xe^+ \rightarrow e^- + Xe^*$), is an important process in ultracold plasmas. It dominates other Rydberg formation processes, such as dielectronic recombination (DR) and radiative recombination (RR) because the total TBR rate varies with temperature as $T_e^{-9/2}$ [50]. The subsequent evolution of Rydberg state population is predominantly driven by electron-Rydberg collisions, radiative decay (RD), and blackbody-induced transitions (BB).

As mentioned in the previous section of this chapter, the plasma expansion velocities at low initial electron temperatures (figure 2.3) indicate electron heating which might be due to the formation of highly excited Rydberg atoms. The following experimental evidence of Rydberg atom production [52] and the observation of the electron temperatures almost independent of initial energies [23] show that TBR and its associated heating play a critical role in the evolution of UCPs.

The most widely used formula for the TBR rate is from an early seminal work of Mansbach and Keck using classical Monte Carlo trajectory calculations [53]. Integrating over the plasma ions gives the number of recombinations per second in the entire plasma:

$$R_{3BR}\,(s^{-1}) = K_{3BR}\,T_e^{-9/2} \int n_e^2(r)n_i(r)4\pi r^2 dr \tag{2.5}$$

where n_e and n_i are the electron and ion spatial density distributions, respectively, $K_{3BR} = 4.5 \times 10^{-21}$ m^{6}K$^{9/2}$s^{-1}.
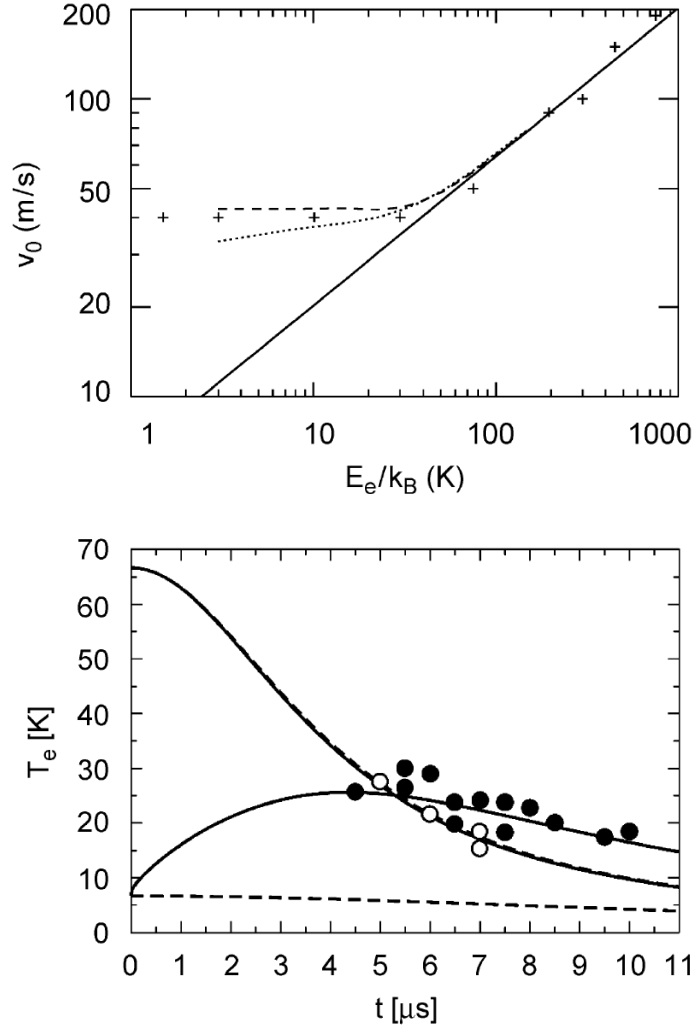
Figure 2.10: Comparison of theoretical caculations and measurements of the plasma expansion velocity and the electron temperature. (Top): The cross line is the experimental data from [16]. The solid line is without TBR; the dotted line is with TBR but no electron-Rydberg atom scattering; the dashed line is with TBR and electron-Rydberg scattering. Reused with permission from [30]. (Bottom): Calculated time evolution of T_e [51] compared to experiment for two different initial T_e of 6.7 K (filled circles) and 66.7 K (open circle). Reused with permission from [51].

Given the very strong inverse electron temperature dependence in Eq. 2.5, this process is clearly of great importance in UCP systems. This divergent temperature dependence has motivated theoretical investigations into whether TBR theory need to be modified in the ultracold regime [54, 55, 58]. In addition to the fundamental interest in TBR at low temperatures, the process is important in the formation of cold antihydrogen through positron-antiproton recombination. A series of theories and experiments [23, 28, 30, 52] suggest that the electrons remain in the weakly coupled regime so that the traditional TBR is still valid. A simple hydrodynamic description with standard collision rates [30] yields a very good description of the plasma dynamics as shown in Figure 2.10. The enhanced expansion velocity of Figure 2.3 can indeed be reproduced by inclusion of electron-Rydberg collisions, and this model gives a quantitative agreement with the temperature measurement [23].

TBR is a process that clearly heats the electron system in the plasma (due to the energy released by the recombination of an ion and electron being carried from the collision by the extra electron), yet has a higher rate of occurrence for a colder plasma. This leads to the possibility of a thermostat effect in the UCP; as temperatures drop due to various processes (and particularly driven by equilibration with the ions and by adiabatic expansion), TBR turns on and arrests the decline in temperature. Thus TBR is a critical process in determining the time-dependent temperature of UCPs.

A measurement of TBR in an UCP can thus be used to test TBR theory by using existing T_e measurements. This is less than ideal, given the paucity of

measurements and the sensitivity of the rate constant to T_e due to the 9/2 power. Conversely, using TBR theory, T_e can be extracted from the measured TBR rate. This is relatively insensitive to the value of the rate constant (due to a 2/9 power law), and can be used to make the first measurement of T_e throughout the life of the plasma. In addition, modifications of the rate constant due to strong-coupling will overestimate T_e (the TBR rate is predicted to be reduced below the 9/2 scaling law to a T_e^{-1} rule in the strong-coupling regime [54, 55]); i.e., our extracted T_e are an upper limit.

We use a microwave ionization technique to detect Rydberg atoms. This technique has several advantages to study Rydberg atoms in UCPs compared with a field ionization ramp (FIR) used in most systems studying Rydberg atoms. Rydberg atoms are ionized by a multi-photon ionization process which is a non-resonant process and largely independent of the microwave frequency. We use 2.4 GHz pulses to take advantage of an electrical resonance in our apparatus. The microwave field has little effect on the plasma and therefore is non-destructive to the plasma because microwaves are much higher frequency than the characteristic plasma frequencies (in our system, 2.4 GHz as compared to ten to a few hundred MHz). Microwave ionization has a slight heating effect on the plasma electrons at times early in the plasma expansion, as the electrons involved in the Rydberg formation via TBR are typically warmer than plasma electrons and undergo several collisions while leaving the plasma. A short, several-hundred nanosecond pulse with our current equipment (microwave source, amplifier, directional couplers, and vacuum feedthrough) tuned to 2.4 GHz is capable of ionizing all Rydberg atoms with principal quantum number

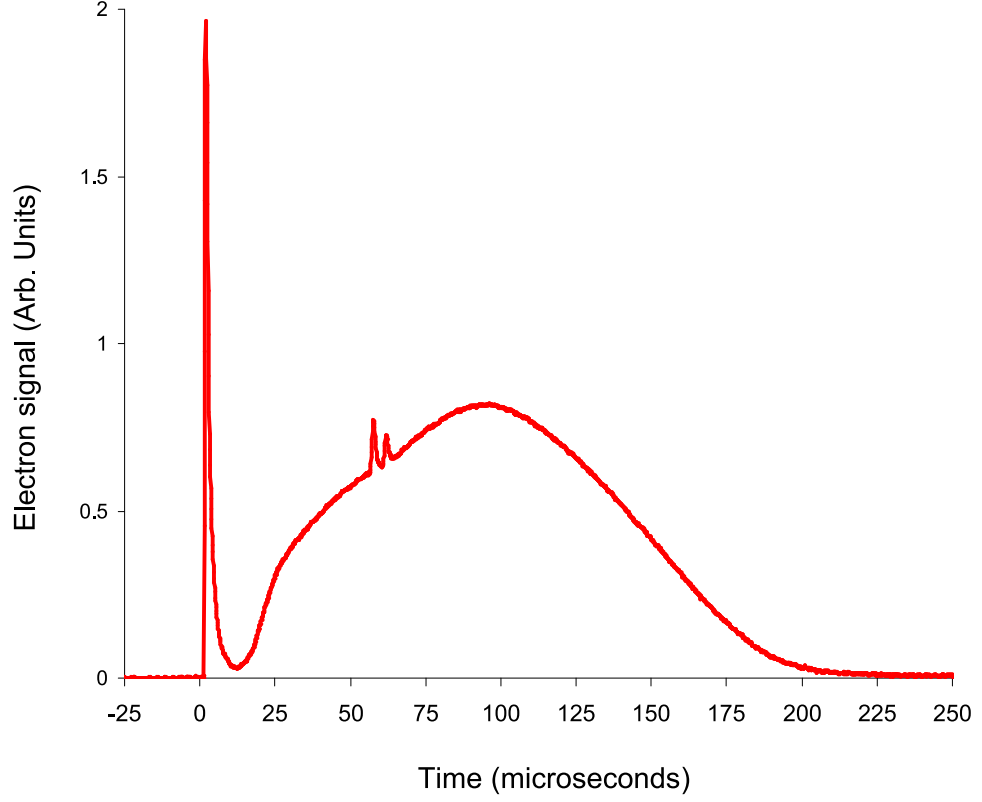Figure 2.11: Electron emission signal from an expanding UCP, averaged over 50 runs. The double peaks at $\sim 55\mu$s are the response due to a pair of short (200 ns) microwave pulses. The first of the two pulses is at a fixed time and ionizes Rydberg atoms that have formed in the plasma. The second pulse is applied at varying times to ionize the Rydberg population that is refilled by three-body recombination. From [26].

$N \geq 35$, which is verified by applying a dc field ionization ramp immediately after a microwave pulse and noting that the signal corresponding to Rydberg atoms with $N \geq 35$ is almost entirely eliminated. This technique can be used to obtain Rydberg population distribution information, as the FIR can. By varying the strength of the microwave pulse, the minimium N-level the pulse is able to ionize is varied [50].

While microwave pulses are a very effective way to detect Rydberg atoms in UCPs, and a single microwave pulse (as well as DC field ionization) can provide a means to measure the number of Rydberg atoms in the plasma, a single pulse does not effectively convey the TBR rate in the plasma because of the complex Rydberg atom processes in UCPs (the long Rydberg lifetime and the collisional redistribution of Rydberg states make this measurement difficult to interpret in the context of TBR, as it is the result of past Rydberg creation and redistribution). Instead, we use a double-microwave pulse to measure the TBR rate. The first microwave pulse (~ 200 ns in duration, with minimal heating) at a chosen time in the plasma expansion clears all Rydberg atoms with N≥35; a second pulse after a variable delay time δt relative to the first pulse detects the Rydberg atoms formed during δt. This results in a double-peaked electron signal (figure 2.11 near 55 μs after the formation of UCP).

This technique is somewhat challenging, given the short delays between the two pulses that are required; for long delays of a μs or longer, the N≥35 population begins to be strongly affected by N-changing collsions, such that the populations measured are no longer simply due to TBR but may be altered due to a loss of the created Rydberg atoms to either ionization or down-shifting of N-levels. Because of
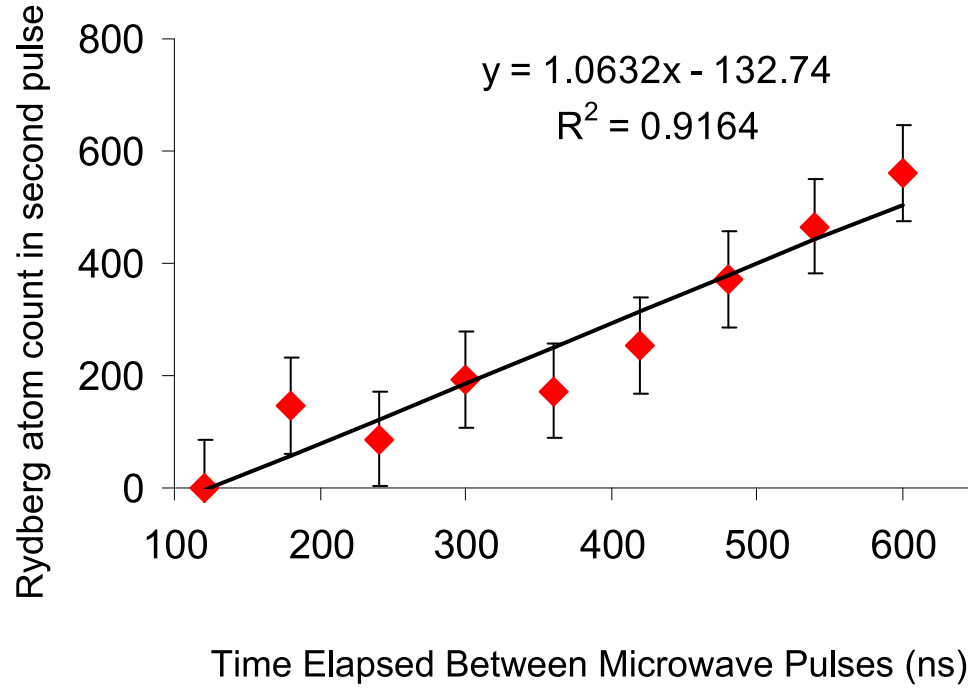
Figure 2.12: An example of the Rydberg refill curve at 55 μs after the formation of the plasma. A linear best fit to these points will have a slope equal to the three-body recombination rate. The uncerntainty for each point is ± 40, so typically we fit straight lines to several such plots and average the fitted slopes.

this challenge, together with the typical signal-to-noise difficulties associated with shot-to-shot noise in the system, we actually use a collection of measurements using different delays (δt) (see Figure 2.12) and perform a linear best-fit to the collection. The slope is then the three-body recombination rate. The linear best-fit is typically limited to delay times of less than 750 ns, as for delay times greater than this the refill curve is no longer linear due to non-TBR effects beginning to turn on. The Rydberg atom count in the second pulse is around several hundred (in the linear region), and it is only about 0.1% of the total number, so the signal to noise ratio is small. The uncerntainty for each point is ± 40, so typically we fit straight lines to several such plots and average the fitted slopes to get the three-body recombination rate.

After performing this several times over a range of times after ionization, we obtained a collection of widely varying three-body recombination rate measurements. To improve the statistics, we binned the rate measurements with respect to time and averaged in both time and rate measurement. Figure 2.13 shows the measured Rydberg refill rates as a function of time.

This is the first measurement of three-body recombination in weakly-coupled neutral plasmas at temperatures below 10 K. Our measurement of the TBR rate has the potential to be the strongest test case for low-temperature TBR theories available. This potential, however, is contingent on better electron temperature measurements being available for these systems. That is, while the TBR rate has been measured and good estimates for the electron and ion time-dependent spatial densities exist, eqn 2.5 depends on electron temperature in a $T_e^{-9/2}$ manner; thus,
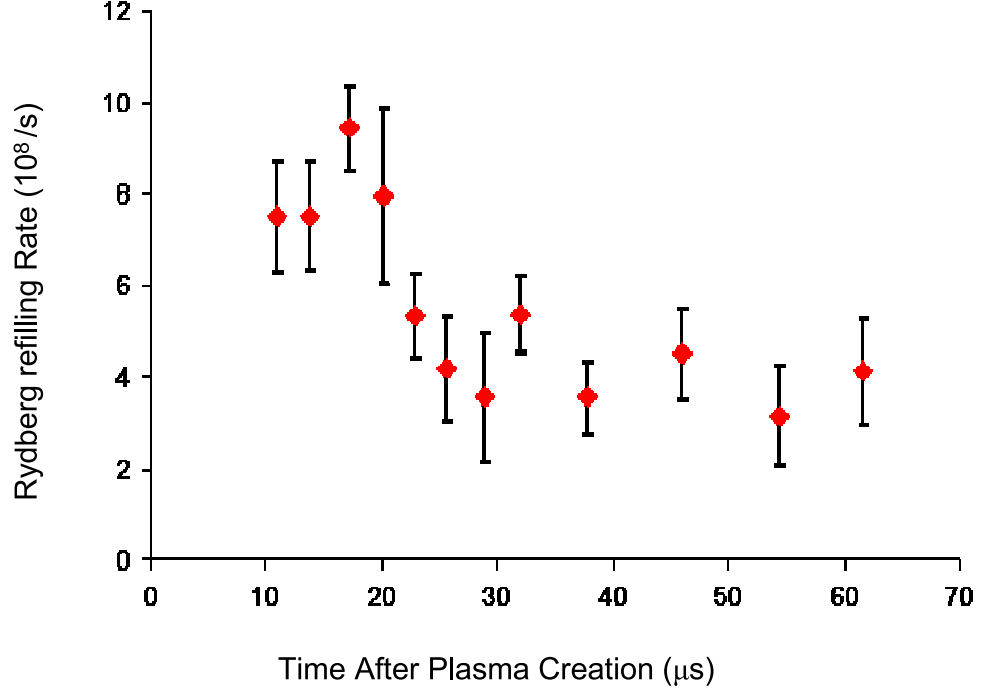
Figure 2.13: The total Rydberg refill rates. The early increase in the rate is likely due to 3BR turning on as temperatures drop; the rate peaks at about 19 μs and then drops to a constant value as the density and temperature continue to decrease. Note that the peak plasma density falls by over two orders of magnitude, from 1×10^{14} m^{-3} at 10 μs to 6×10^{11} m^{-3} at 60 μs, while the 3BR rate only decreases by a factor of two. The error bars represent the 1σ standard uncertainty resulting from the linear fits to the refill curves (Figure 2.12).

without very good electron temperature measurements, it is impossible to say with any certainty whether a given theoretical rate expression is a valid description of the measured TBR rates.

If we assume that TBR theory with $K_{3BR} = 4.5 \times 10^{-21} \text{m}^6 \text{K}^{9/2} \text{s}^{-1}$ provides us with an accurate rate equation (eqn 2.5) [53], we can invert the expression and instead attempt to use the rate measurements as a means to extract the electron temperatures $T_e(t)$:

$$T_e(t) = \left[\frac{R_{3BR}(t)}{K_{3BR} \int n_e^2(r) n_i(r) 4\pi r^2 dr} \right]^{-2/9} \tag{2.6}$$

By using our measured TBR rates (figure 2.13) with the inverted TBR rate equation (eqn 2.6), we calculate the time-dependent electron temperatures, as plotted in Figure 2.14a. Our calculated temperatures are diamonds (also in the inset plot), while we include previous T_e measurements for an initial $\Delta E = 10$ K (squares, [23]), simulation results for a $\Delta E = 66$ K (dashed line) [56] and simulation results for a $\Delta E = 3$ K (solid line) [57] for comparison. A simple power-law fit of the temperature curve of Figure 2.14a gives $T_e(t) \sim t^{-1.2(1)}$. Adiabatic cooling would suggest a $T_e(t) \sim t^{-2}$ relationship; the difference is likely due to the significant heating effects from TBR. This method of determining the electron temperature results in electron temperatures well below one Kelvin at later times (after 40 μs), by far the lowest T_e observed in any neutral plasma. Indeed, extrapolating to the end of the plasma lifetime (~ 200 μs), the power-law fit indicates temperatures as low as ~ 200 mK. T_e is rather insensitive to the value of K_{3BR}, as a factor of two change in the rate

constant results in only a 16% change in temperature.

Using the temperature calculations of Figure 2.14b with the density expression given in eq. 1, we calculate the electron coupling parameter $\Gamma = e^2/(4\pi\epsilon_0 a k_b T_e)$, where a is the average Wigner-Seitz length. $\Gamma(t)$ is plotted in Figure 2.14b. The system remains weakly coupled ($\Gamma \ll 1$), but the coupling increases as the plasma expands and cools.

Although standard TBR theory is expected to fail in strongly coupled systems, we use a typical TBR expression and extract $T_e(t)$ for the plasma. Because the resulting T_e estimates match well with another measurement of the temperature and with simulation results (at least at early times in the plasma expansion), the use of the accepted TBR rate expression in this work appears justified. Our method is self-consistent with extracted temperatures that show the plasma to be weakly coupled. Future measurements of T_e in an independent manner would allow a direct test the validity of the TBR expression in UCPs. This is the lowest-T_e measurement of three-body recombination rates to date; the measured rates indicate the plasma system achieves sub-Kelvin electron temperatures at late times.

Recent theoretical work by Pohl [58] suggests a somewhat different form for the three-body rate expression. His proposed rate is somewhat lower than that of Mansbach and Keck, but has the same $T_e^{-9/2}$ scaling, and could affect the eqn 2.6 that we used in calculating electron temperatures. The improved rate coefficients yield quantitative agreement with our Rydberg atom refilling rate measurements as shown in figure 2.15). However, as the two rates are less than a factor of 5 different for the parameters typical of our system [58], this modification would only alter our
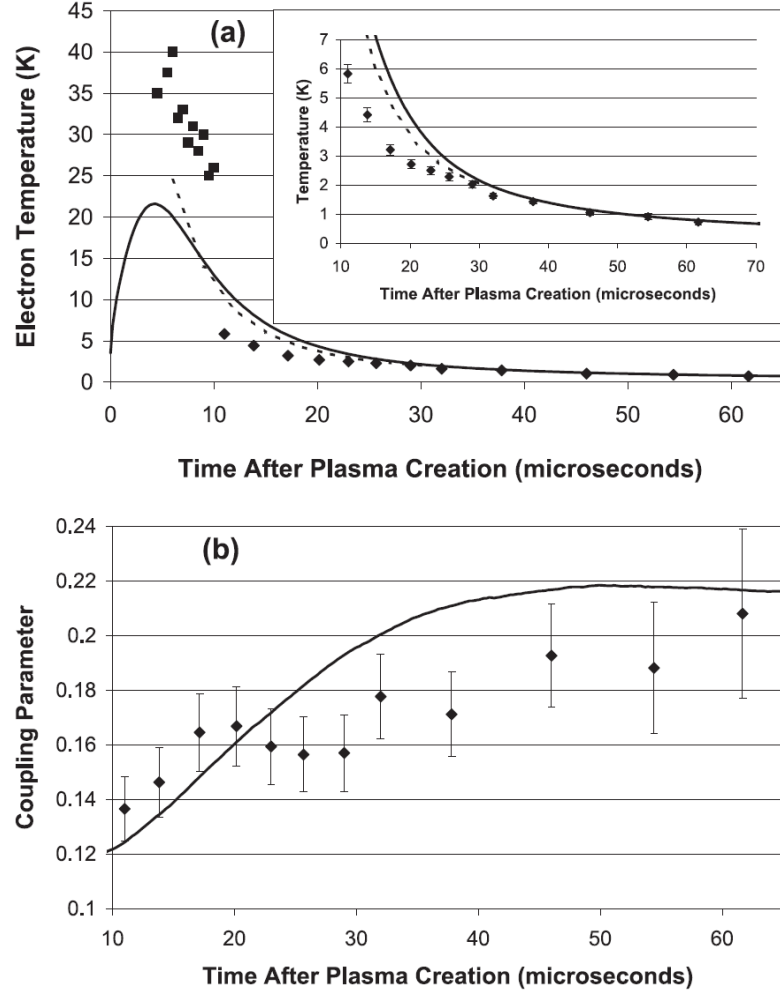
Figure 2.14: The extracted T_e from TBR rate and corresponding plasma coupling parameter. (a) We calculate T_e using established TBR theory with the rates we measure and an assumed self-similar Gaussian expansion of the plasma (diamonds; also inset). The initial energy is $\Delta E = 3$ K. For comparison, we plot earlier T_e measurements for $\Delta E = 10$ K (squares) [23] and simulation results for $\Delta E = 66$ K (dashed line) [56] and $\Delta E = 3$ K (solid line) [57]. (b) The corresponding plasma coupling parameter Γ with the simulation results by Pohl (solid line) [57]. The error bars are the propagated uncertainties from figure 2.13.
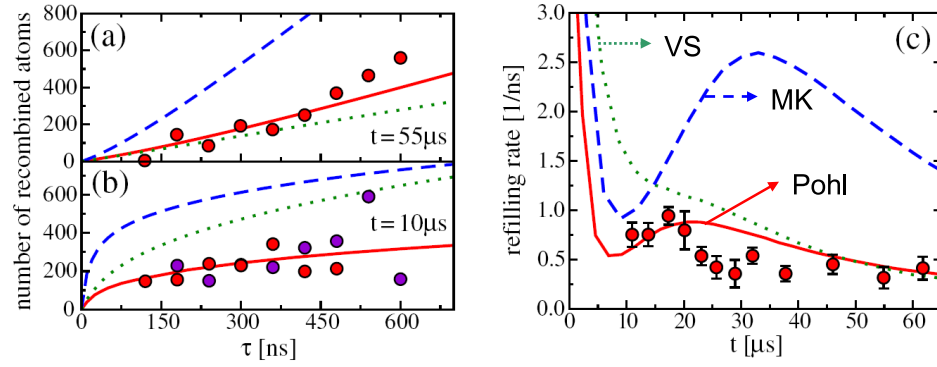
Figure 2.15: Comparison of actual number of recombined Rydberg atom and the Rydberg refilling rate calculations by using MK rate and Pohl rate. (a), (b) Actual number of recombined Rydberg atom and (c) the Rydberg refilling rate, as measured in ref [26]. Compared to the predictions of the MK rates (dashed lines) and VS rates (dotted lines), plasma simulations based on the Pohl rates (solid lines) yield an improved description of the experimental data points (dots). The experimental data points at 10 μs include two separate measurements. From [58], used with permision.

electron temperature calculations by, at most, 40%.

Future work on the Rdyberg atoms in UCP will focus on testing the three-body recombination rate expression. The Mansbach and Keck expression [53] results in TBR generating Rydberg atoms with a population distribution varying with the principal quantum number N as N^6, with a cutoff in the distribution at $N_{max} = \sqrt{(13.6eV/2k_BT_e)}$. However, the Pohl expression [58] predicts a population distribution due to three-body recombination that varies as N^4, with a similar N_{max} cutoff. It is clear that measuring the Rydberg N-distribution due to three-body recombination can be a potentially definitive means to verify one or the other expression without requiring accurate knowledge of the electron temperatures. This will further support the use of three-body recombination rate measurements as a means of measuring the electron temperatures. Such a measurement can be performed by modifying the double-pulse technique for measuring the three-body recombination rate. Varying the second (probe) pulse power, we can measure the Rydberg atoms formed during the time delay between the two pulses, and extracted the Rydberg N-distribution [50].

Chapter 3

Ultracold Plasma Expansion in a Magnetic field

Plasma expansion in a uniform magnetic field is of interest in astrophysical, ionospheric, and laser-produced plasma applications. The presence of a magnetic field during the expansion can initiate various phenomena, such as plasma confinement and plasma instabilities [59]. UCPs have system parameters many orders of magnitude away from traditional laser-produced plasmas, with electron and ion temperatures on the order of meV, or even μeV, and densities of 10^5 to 10^{10} cm^{-3}. UCPs thus provide a testing ground to study basic plasma theory in a clean and simple system. Since ultracold plasmas are so cold, we need only tens of gauss magnetic field to confine them (note that the cyclotron (Larmor) radius of an electron with energy of 10 K is about 70 μm in a 10 G magnetic field). In a magnetic field where the electron Larmor radius is much less than the size of plasma, the electrons become "bound" to the field lines, and the ions are confined by the Couloumb force from the electrons. All previous studies of ultracold plasma expansion, both experimental [13, 14, 16, 22] and theoretical [27, 31, 43, 44], focus on free expansion in the absence of magnetic fields as discussed in the previous chapter.
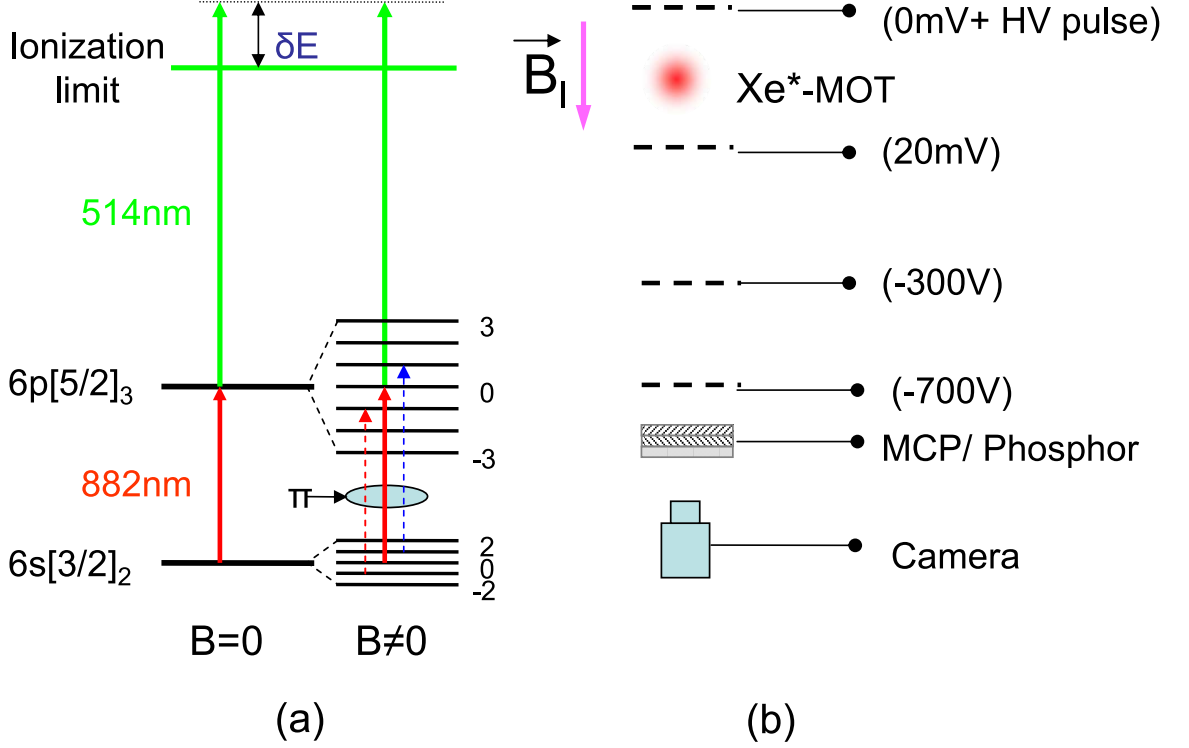
Figure 3.1: Experimental setup and two-photon excitation process for UCP in a magnetic field. (a) two-photon excitation process: one photon (red solid line, π polarized) is from a Ti:sapphire laser at 882 nm and drives the $6s[3/2]_2$ (m = 0) $\rightarrow$ $6p[5/2]_3$ (m = 0) transition, and the other is from a pulsed dye laser at 514 nm and ionizes the atoms in the $6p[5/2]_3$ (m = 0) state. The dashed lines are the repumping beams (both blue and red of the $6s[3/2]_2 \rightarrow 6p[5/2]_3$ transition, also π polarized); (b) experimental setup for imaging the ions onto the MCP/phosphor screen.

3.1 Creation of Ultracold Plasma in a Magnetic field

As described in Chapter 1, metastable Xenon atoms are cooled and trapped in a magneto-optical trap (MOT). The neutral atom cloud has a temperature of about 20 μK, total number of about 2×10^6, peak density of about 2 x 10^{10} cm^{-3}, and a Gaussian spatial density distribution with an rms radius of about 280 μm. The plasma is then produced by a two-photon excitation process (figure 3.1a), ionizing up to 30% of the MOT population. One photon for this process is from the cooling laser at 882 nm, and the other is from a pulsed dye laser at 514 nm (10-ns pulse). We control the ionization fraction with the intensity of the 514-nm photoionization laser, while the initial electron energy is controlled by tuning the 514-nm photon energy with respect to the ionization limit.

Without magnetic field, we can simply use the MOT beams to drive the $6s[3/2]_2 \rightarrow 6p[5/2]_3$ transition; with the addition of a magnetic field, the $6s[3/2]_2$ and $6p[5/2]_3$ states split into 5 and 7 Zeeman sub-levels respectively, shifting the transitions out of resonance as shown in Figure 3.1a. To maintain a reasonable excitation fraction, we need to optically pump the atoms into the m = 0 magnetic sublevel of the ground state and then drive the $6s[3/2]_2$ (m = 0) $\rightarrow 6p[5/2]_3$ ($m' = 0$) transition, which will be unaffected by the magnetic field to first order. (We cannot turn on magnetic fields in a time short compared to the time that ions acquire velocity in the plasma due to electron pressure ($\sim$ 1 μs) and thus must photoionize in the presence of the magnetic field). It is difficult to accumulate a large m = 0 population via optical pumping for a $J \rightarrow J + 1$ transition, so we developed a multiple-frequency

70

VCO-1 — 83.7 MHz

VCO-2 — 81.2 MHz

VCO-3 — 78.7 MHz

Power Splitter

RF Switch

3 repumping beams

DP AOM

RF Amplifier

0th order beam from MOT AOM
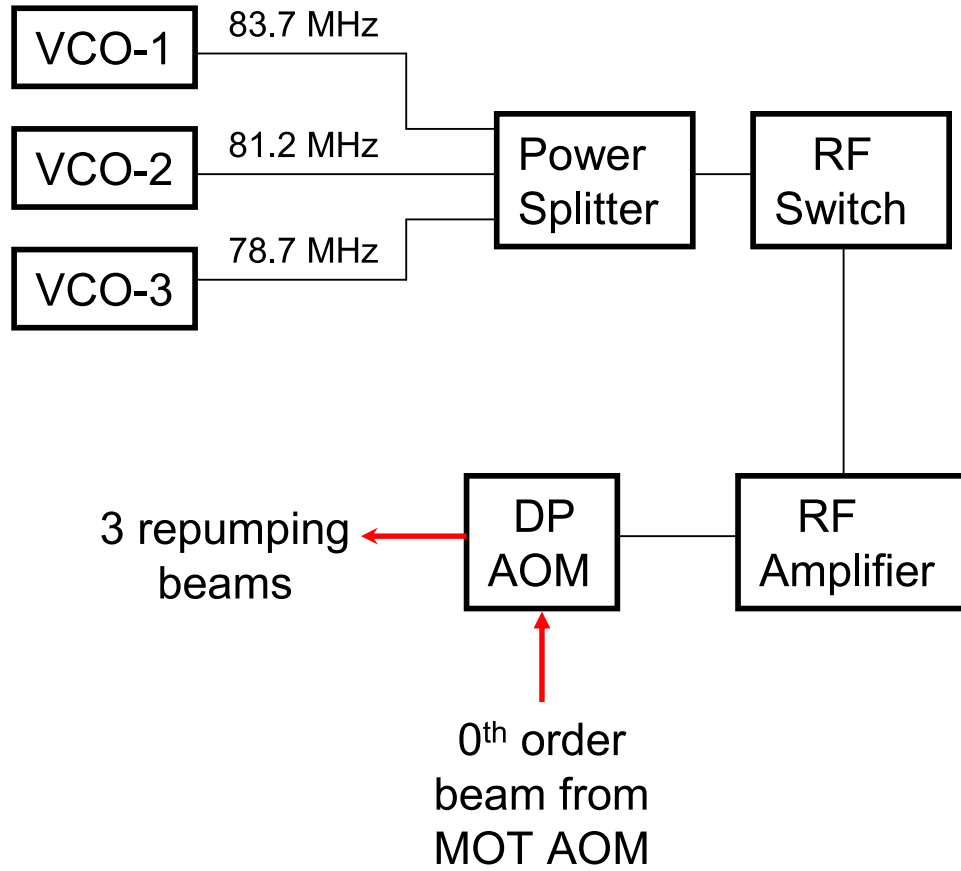
VCO: Voltage controlled oscillator

DP: Double passed

AOM: Acousto-optic modulator

Figure 3.2: Schematic diagram for generating three π-polarized optical pumping beams. They are detuned -5, 0, 5 MHz respectively relative to the $6s[3/2]_2$ (m = 0) $\rightarrow 6p[5/2]_3$ ($m' = 0$) transition. The AOM has a central value of 80 MHz.

scheme that uses Zeeman shifts to address the m = 0 and m = $\pm$ 1 sublevels (figure 3.1a). We use three voltage controlled oscillators, which are detuned -5, 0, 5 MHz respectively relative to the $6s[3/2]_2$ (m = 0) $\rightarrow$ $6p[5/2]_3$ ($m' = 0$) transition, to drive a double-pass acousto-optical modulator to generate three π-polarized optical pumping beams (the 3-frequency scheme is a compromise of a 5-frequency one, which would be best since the ground state $6s[3/2]_2$ has 5 Zeeman sub-levels, but it is too complicated (needs several AOMs and more laser power).) (Figure 3.2). At about 20 G field, the energy shift between $m = 0 \rightarrow m' = 0$ and $m = +1 \rightarrow m' = +1$ is about 5 MHz. We first turn on the repump beams for several hundred nanoseconds at a field of 20 G to repump the atoms into the $6s[3/2]_2$ (m = 0) state, and then turn the field on to the final specific value at which we create UCPs by two photon process. With this configuration, we can achieve UCP densities of $\sim$ 50% of the zero field value, approximately independent of magnetic field up to 100 G, which is consistent with a simple rate calculation by assuming that the atoms are equally distributed in m-sublevels. Figure 3.3 is the electron emission signal for different magnetic fields. As we increase the magnetic field from zero to several tens of gauss, the electron signal looks similar to that without a magnetic field except for a smaller signal and longer lifetime, so it is hard to extract useful information about the magnetic field effect on the plasma, and a new method to study the plasma dynamics in a magnetic field is needed.
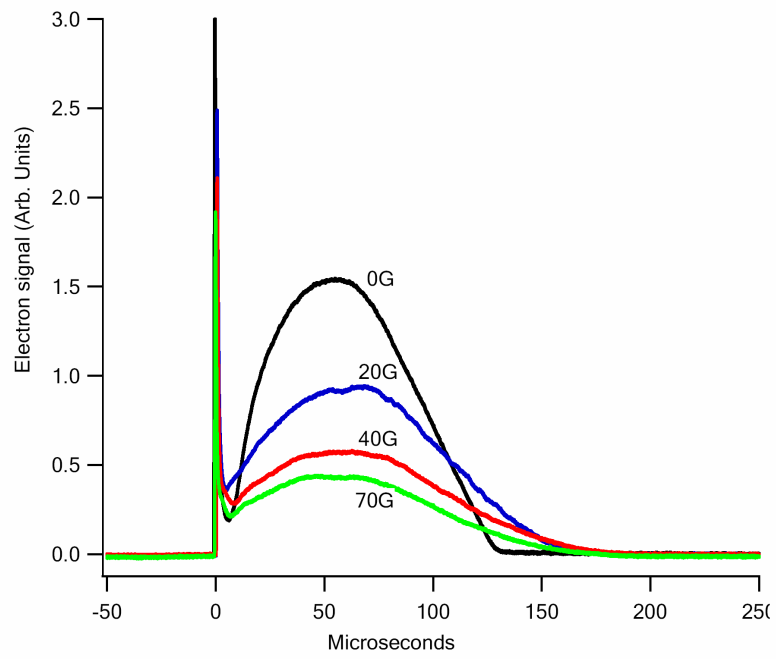
Figure 3.3: Typical electron emission signals for different magnetic field. The curves are for magnetic field B = 0, 20, 40, 70 G from top to bottom, respectively.

3.2 Using Projection imaging to Study UCP Expansion in a Magnetic field

For Xenon UCP experiments, we usually use the charged particle detection method to study the UCP dynamics. Fortunately, the charged particle detector - MCP also has a phosphor screen, allowing us to obtain spatial information regarding where on the detector charged particles strike, even though we can not use the absorption or fluorescence imaging used in UCPs of other elements. This is potentially more useful than the optical probes in some aspects, as the MCP technique can be applied to either electrons or ions, and can be used at later times in the plasma expansion when the densities are too low for effective use of the two optical techniques, especially for study the UCP dynamics in the presence of a magnetic field.

The magnetic field is generated by a pair of coils which are located outside the vacuum chamber with 40 turns each and 11-cm diameter and 5-cm separation, and is fully turned on before the creation of the UCP. By applying a high-speed, high-voltage pulse ($\sim$ 400 V with a 50-ns turn-on time) to the top grid (about 1.5 cm above the plasma) and with accelerating fields on the middle and front grids (figure 3.1b), we image the ion distribution of the UCP on the phosphor screen of the MCP detector. The phosphor images are recorded with a CCD camera. We image the ions at different delay times after the formation of plasma by applying the high voltage pulse to the plasma at specific delay times. Figure 3.4 is a typical result obtained by averaging of 8 images to increase the signal-to-noise ratio. Figure

74

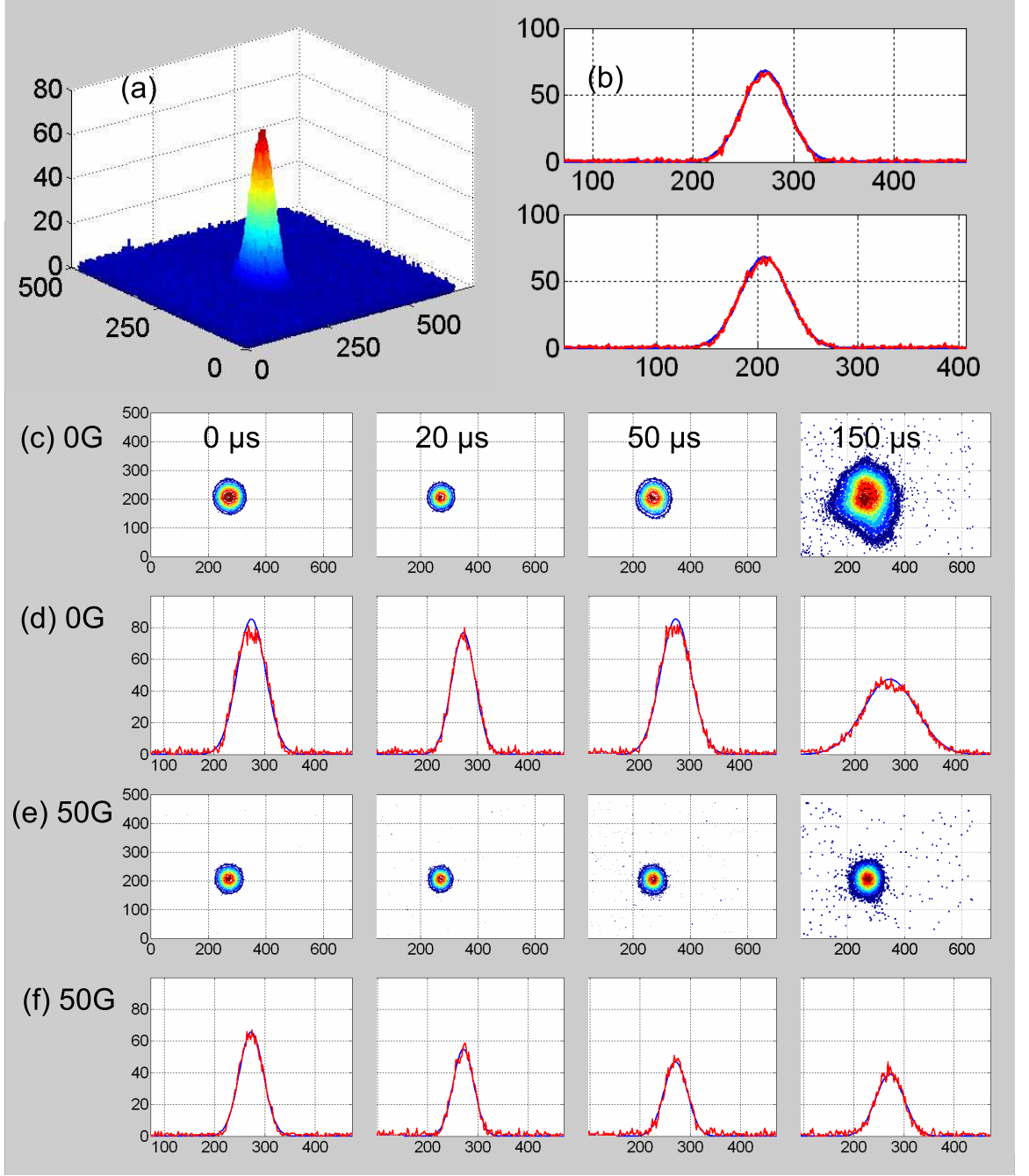Figure 3.4: (a) a false color ion image of UCP at delay time of 20 μs for $T_e = 100$ K and B = 20 G; (b) 2-D Gaussian fitting of the ion image (a); (c) and (e) are the contour plots of the ion images at different delay times for 0 G and 50 G respectively; (d) and (f) are the corresponding 2-D Gaussian fit of (c) and (e). All the units in (a)-(f) are in pixel number, and 1 pixel unit is about 150 μm.

3.4a is a false color plot of an ion image after 20 μs of plasma evolution for $T_e =$ 100 K and B = 20 G, which fits well to a 2-D Gaussian profile (figure 3.4b). Figure 3.4c and 3.4e are the contour plots of the ion images at different delay times for 0 G and 50 G respectively; figure 3.4d and 3.4f are the corresponding 2-D Gaussian fit of 3.4c and 3.4e. All the units in (a)-(f) are in pixel number, and 1 pixel unit is about 150 μm. The ion images maintain a Gaussian profile during the whole lifetime of the UCP (about 200 μs) as shown in figure 3.4 c-f.

By 2-D Gaussian fitting of the ion image, we extract the transverse size perpendicular to the applied magnetic field at specific delay times (the extracted size is the average one from the two directions which have only several percent difference). In figure 3.5, we plot the transverse sizes of UCPs in a magnetic field as a function of time. The size of the image decreases in the first 20 μs due to the decrease of the strong time-of-flight Coulomb explosion of the dense ion cloud as the plasma expands [42], and then afterwards increases, reflecting the true size of the plasma. This can be understood as the following: the electrons will be extracted from the UCPs very fast (several hundred nanoseconds) by the high voltage pulse, but does not affect ion distribution during that short time. The ions will then fly to the detector in about 8-9 μs, which can be extracted from the delay between the high voltage pulse and the ion current pulse on the detector. For a spherical Gaussian distribution of an ion cloud of size σ and total number N, The Couloumb potential energy is given by:

$$\phi_{(r)} = \frac{1}{4\pi\epsilon_0}\frac{Ne}{r}erf(\frac{r}{\sqrt{2}\sigma}) \tag{3.1}$$

76
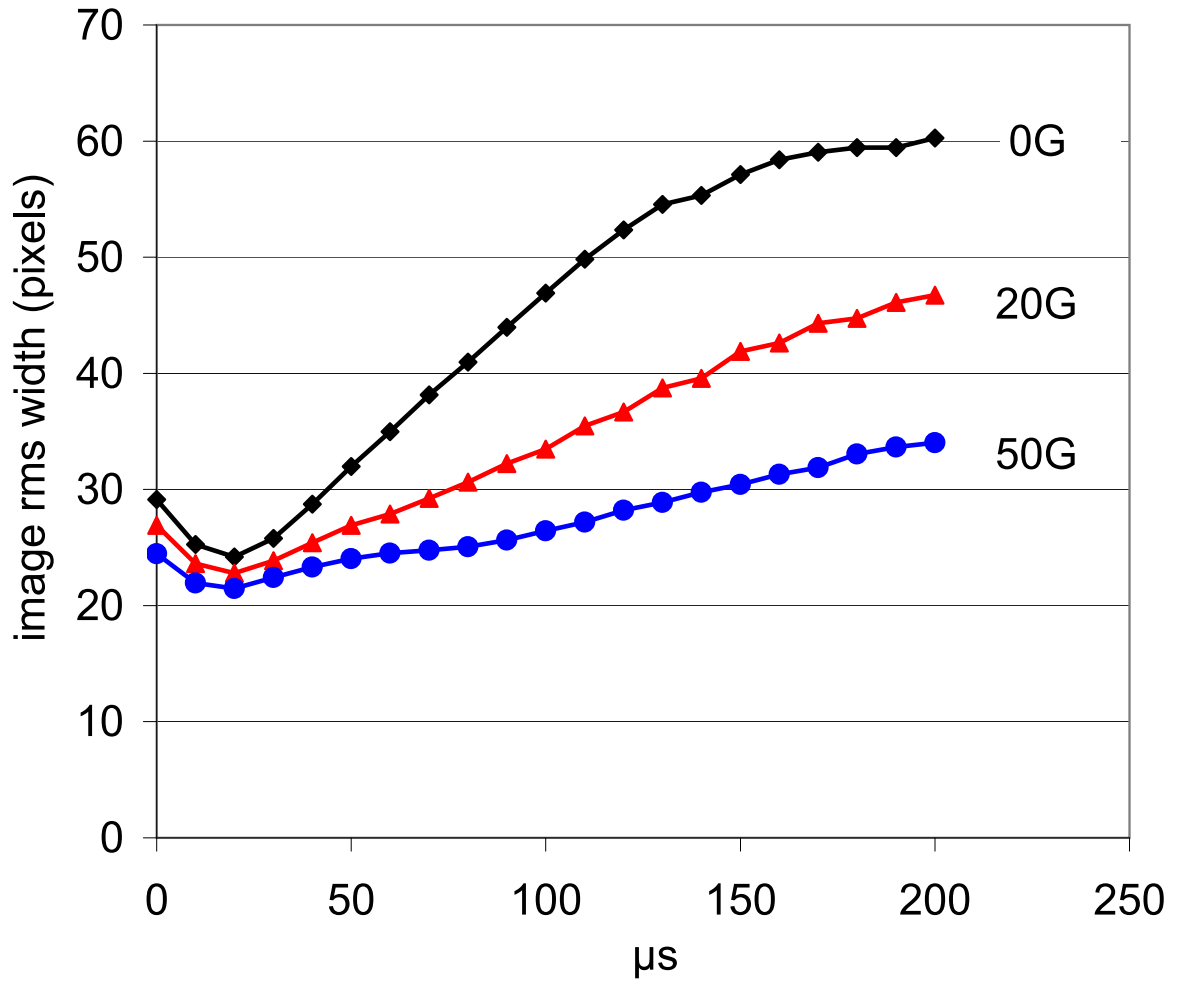
Figure 3.5: Transverse sizes of UCP in a magnetic field. The black curve (diamonds) is for 0 G, the red curve (triangles) is for 20 G, and the blue curve (dots) is for 50 G. Early in the lifetime of the plasma, the size of the image is dominated by the Coulomb explosion of the dense ion cloud.
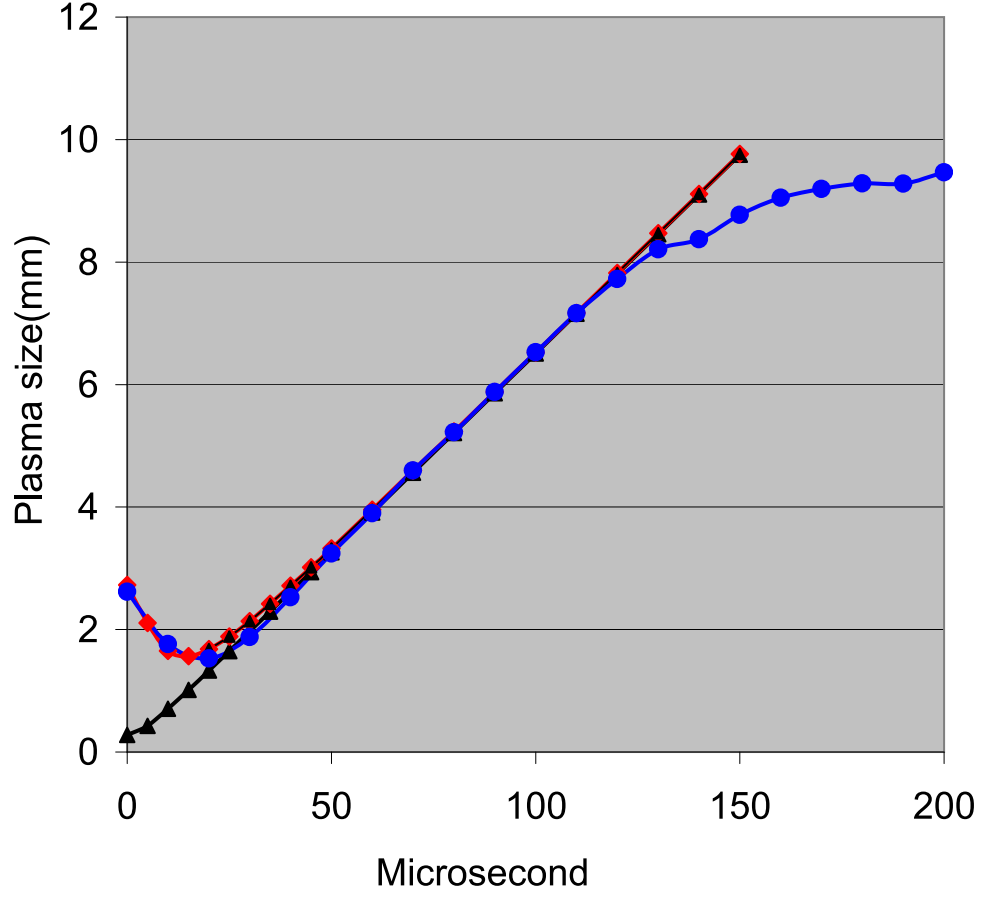
Figure 3.6: Couloumb explosion of ion cloud. The black curve (triangles) is from the balllistic expansion model with initial size of 300 μm and expansion velocity of 65 m/s; The blue curve (dots) is the zero-field plasma size with a global factor of 1.4 (ion lensing effect, discussed later); The red curve (diamonds) is the calculated plasma size after 8 μs Couloumb explosion.

Where $erf(x)$ is the error function. So the average Couloumb energy, which is close to the potential energy at $r = \sigma$ point, is inversely proportional to the size of the ion cloud as we can tell from eqn. 3.1. At early times, the plasma size is small (on the order of intial size, about several hundred micrometers) and the strong coulomb repulsion of the ions produces a large ion image during the transport of the ions to the phosphor screen detector. As time evolves, the size of the UCP increases because of the free expansion driven by the electrons pressure on the ions, so the Coulomb repulsion is reduced with less effect on the plasma size. As the size of the UCP is much larger than the inital size and the Coulomb explosion is negligible, it will linearly increase over time, reflecting the true size of the plasma, as expected from the ballistic expansion model. Assuming that ion cloud is not affected by the fast high voltage pulse and maintains a spherical Gaussian distribution in the Coloulomb explosion phase (an approximation, not entirely true), we can extract the initial ionic cloud size from the ion projection image on the detector. The plasma size indeed follows the ballistic expansion model as shown in Figure 3.6. If we also consider that the ion cloud will freely expand with the ion acoustic velocity in addition to the Coulomb explosion during the 8 μs time-of-flight time, this will increase the plasma size by several hundred micrometers, but not affect the overall slope of the temporal evolution of the size of the plasma.

As we increase the magnetic field, the transverse size increases more slowly with time, i.e., the slopes of the curves decrease, which indicates a slower expansion and magnetic confinement in the transverse direction of the UCP. For 0 G at long times, the size does not increase linearly. This is in part because the size of the

79

UCP is large enough to be affected by the four posts that secure our grids above and below the plasma. We also note that the ion images have a flat top and even dip at late times of about 150-200 μs for the 0 G case, the cause of which is unknown.

By linear fitting to the transverse sizes as a function of time after about 20 μs (for 0 G, only fitting the restricted linear region), we extract the transverse asymptotic expansion velocity of the UCP with a magnification factor of 1.5 due to the ion lensing effect (The electrodes tends to focus or expand a charged particles beam when it passes thorough a series of electrodes). This is confirmed by adjusting the voltage settings of grids (especially the middle grid), which changes the ion image size as well as the scaling factor. By using SIMION 3D, a popular ion optics simulation program designed to study and analyze ion optics, we simulate our ion projection imaging setup with the actual voltage settings of the grids and get the ion lensing factor of 1.4 from the ion trajectories, which is consistent with the global scaling factor.

It only results in about several percent change in the plasma expansion velocity by including the restored plasma sizes of the early time in the linear fitting compared to that by only fitting the linear region of the ion image temporal evolution after the Coulomb explosion phase. In figure 3.7, we plot the transverse asymptotic expansion velocity as a function of magnetic field. The blue solid curve with square points is the experimental result, the black dashed curve is a power-law fit of the data, and the red curve with triangle points is a simulation by assuming that the transverse expansion is due to ambipolar diffusion (discussed next section). In the absence of a magnetic field and 100 K initial electron temperature, the UCP expands with an

80

$$V_0 = (92\pm10)B^{-(0.43\pm0.1)}$$
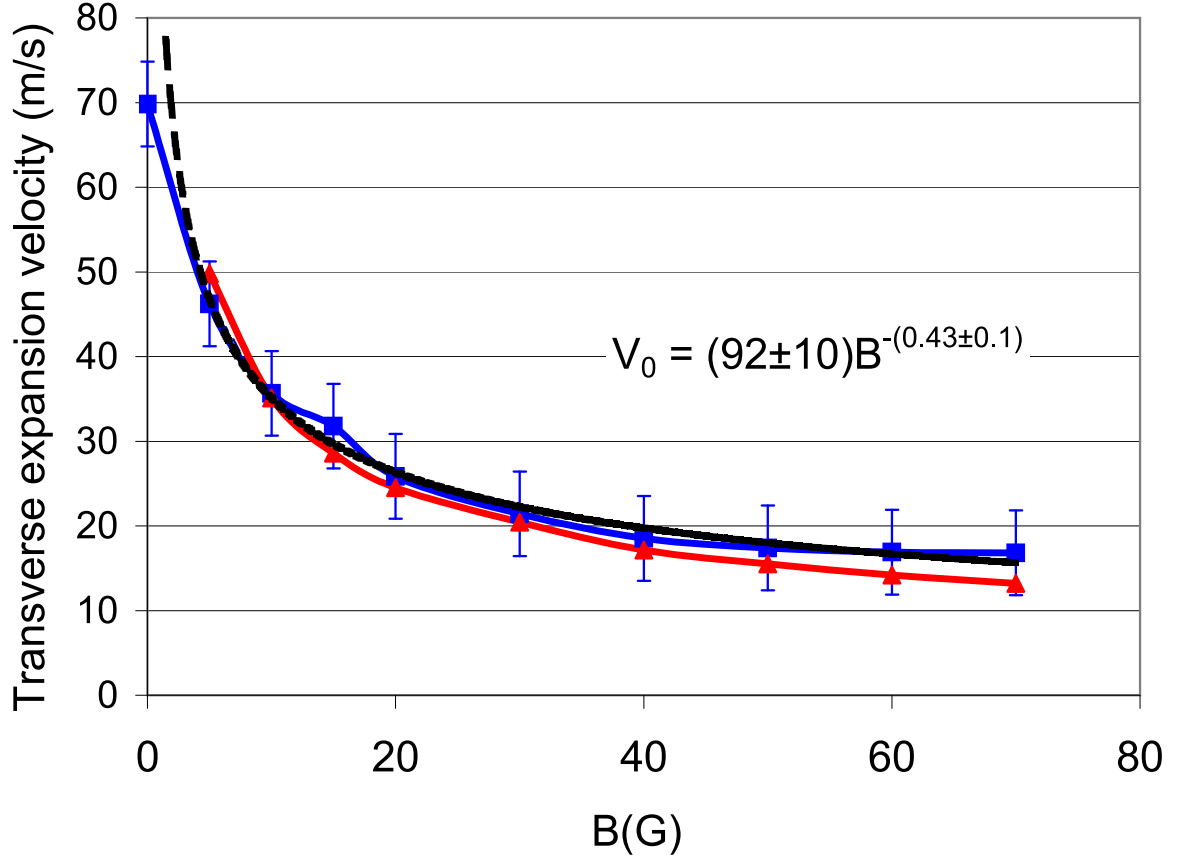
Figure 3.7: The transverse asymptotic expansion velocity as a function of applied magnetic field. The blue curve (squares) is the experimental result, the black dashed curve is power-fitting of experimental data, and the red curve (triangles) is the computer simulation using an ambipolar diffusion model that involves anisotropic diffusion in two directions. The error bars represent the 1σ standard uncertainty resulting from the linear fits to the curves in figure 3.5.

asymptotic velocity of about 70 m/s caused by the outward electron pressure. This is the ion acoustic velocity at the initial electron temperature. As the magnetic field increases, the transverse expansion velocity decreases, roughly scaling as $B^{-1/2}$. At 50 G, it is about 17 m/s, about a factor of four smaller than that at 0 G.

Using the same technique, we extract the transverse asymptotic expansion velocity for different initial electron temperatures, shown in figure 3.8. The red solid line with square points is the experimental result for 0 G, which agrees with the results obtained by measuring the plasma oscillation frequency (the black solid curve with circle points) [16], as discussed in Chapter 1. The dashed lines are linear fits of the data above 60 K. For 50 G, the transverse expansion velocity as a function of initial electron temperature is similar to that at 0 G except for a factor 3-4 smaller. The expansion velocity goes as $T_e^{1/2}$ for an initial electron temperature higher than 60 K, that is, the slopes of the dashed lines in figure 3.8 are about 1/2 which is indicated by the self-similar expansion model.

3.3 Ambipolar Diffusion Model of UCP Expansion in a Magnetic Field

The expansion of the UCP at the ion acoustic velocity can be understood in terms of electron pressure in a simple hydrodynamic model [16], or alternatively as ambipolar diffusion, where oppositely charged particles (electrons and ions) diffuse together at the lower ion velocity. In a magnetic field, ambipolar diffusion allows charged particles to cross field lines, and produces a diffusion constant that scales as
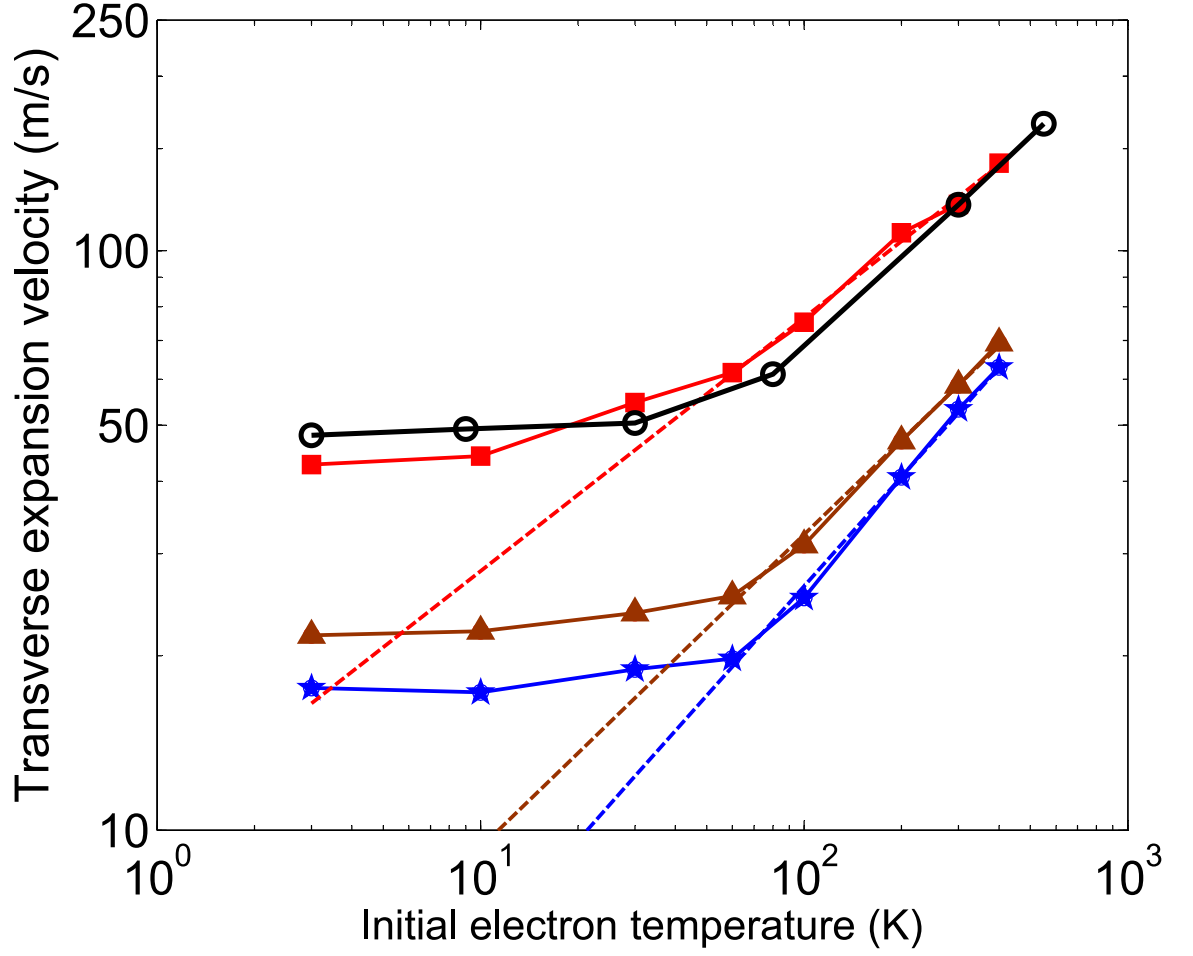
Figure 3.8: The transverse expansion velocity as a function of initial electron temperature T_e. The red solid curve (squares) is the experimental result for 0G which matches the results obtained by measuring the plasma oscillation frequency (the black solid curve (circles)) [16]. The brown solid curve (triangles) is for 25 G, and the blue solid curve (stars) is for 50 G. all the dashed lines are the linear fitting of the data above 60 K with slopes of about 1/2.

B^{-2}, and a transverse decay size (expansion velocity) scaling of B^{-1} for conventional low temperature plasmas such as arc plasmas and strongly ionized plasmas in steady state (Q machine) [60]. This is in contrast to our observed $B^{-1/2}$ scaling. Another possibility would be anomalous diffusion (Bohm diffusion) with a diffusion constant scaling as B^{-1}, which is closely connected to plasma instabilities [61, 60]. However, observing the electron signals as well as the ion images with the magnetic fields, we do not see any signature of plasma instabilities.

Our UCPs are rather novel plasma systems, not only because of their low temperatures, but also because they are unconfined, inhomogeneous, and freely expanding into vacuum (the same properties hold for the UCP expansion along the magnetic field). There is also competition between adiabatic cooling and three-body recombination-induced heating leading to a time-dependent falling electron temperature [26]. Given the dynamics of the plasma, we cannot simply apply steady-state ambipolar diffusion theory, but must include the dynamics. In a strong magnetic field, the diffusion rate of a plasma becomes anisotropic; the diffusion rate is almost unaffected in the direction along the magnetic field, while it is reduced in the direction normal to the field. For our UCP expansion in the magnetic field, we assume ambipolar diffusion in both directions (along the field and normal to the field) and write the diffusion equation as follows by separating the diffusion rate into two terms in cylindrical coordinates:

$$\frac{\partial n}{\partial t} = \frac{1}{r}\frac{\partial}{\partial r} r D_\perp \frac{\partial n}{\partial r} - \frac{n}{\tau_\parallel} \tag{3.2}$$

where $D_\perp$ is the transverse ambipolar diffusion rate with $D_\perp = \rho_e^2 \nu_{ei} \propto \frac{n_e}{B^2 T_e^{1/2}}$,

84

ρ_e is the electron gyroradius and ν_{ei} is the electron-ion collision rate. $\tau_\parallel$ is the characteristic time with $\tau_\parallel = a(t)/v_s(t)$, a(t) and $v_s(t)$ are the plasma size and the expansion velocity along the magnetic field respectively. The first term in the right hand side of eqn 3.2 corresponds to the diffusion normal to the field, and the second term is the diffusion along the magnetic field. By normalizing eqn 3.2, we get:

$$\frac{\partial \tilde{n}}{\partial \tilde{t}} = \frac{1}{\tilde{r}} \frac{\partial}{\partial \tilde{r}} \frac{\tilde{r}\tilde{n}}{\tilde{T}^{1/2}} \frac{\partial \tilde{n}}{\partial \tilde{r}} - \frac{\alpha \tilde{n}}{\tilde{\tau}_\parallel} \tag{3.3}$$

where $\tilde{n} = \frac{n}{n_0}$, $\tilde{t} = \frac{t}{t_0}$, $\tilde{r} = \frac{r}{a_0}$, $\tilde{T} = \frac{T}{T_0}$, $\tilde{\tau}_\parallel = \frac{\tau_\parallel}{\tau_{\parallel 0}}$, $\alpha = \frac{t_0}{\tau_{\parallel 0}}$, with $t_0 = \frac{a_0^2}{\rho_{e0}^2 \nu_{ei0}}$ and $\tau_{\parallel 0} = \frac{a_0}{v_{s0}}$.

For simplicity, we assume that there is no spatial temperature gradient for our UCP, and that the density profiles in both directions remain Gaussian throughout the lifetime of the UCP. To solve eqn 3.3, we also need to know the electron temperature evolution of the UCP in the magnetic field. We did not observe any difference in electron temperature evolution with the application of a large magnetic field when we measured the electron temperature with three-body recombination [26], so we assume the electron temperature evolution is independent of magnetic field for our diffusion model. Electron temperature evolution in an expanding UCP is a complicated problem and has been studied using various methods [23, 22, 24, 26]. By using Doppler broadening of the ion optical absorption spectrum together with numerical simulation, it has been found that the electron temperature evolution follows the self-similar analytic solution during the first 20 μs for an initial temperatures greater than 45K, that is, $T_e = T_e(0)/(1 + t^2/\tau_{\parallel 0}^2)$ [24]. By using three-body recombination
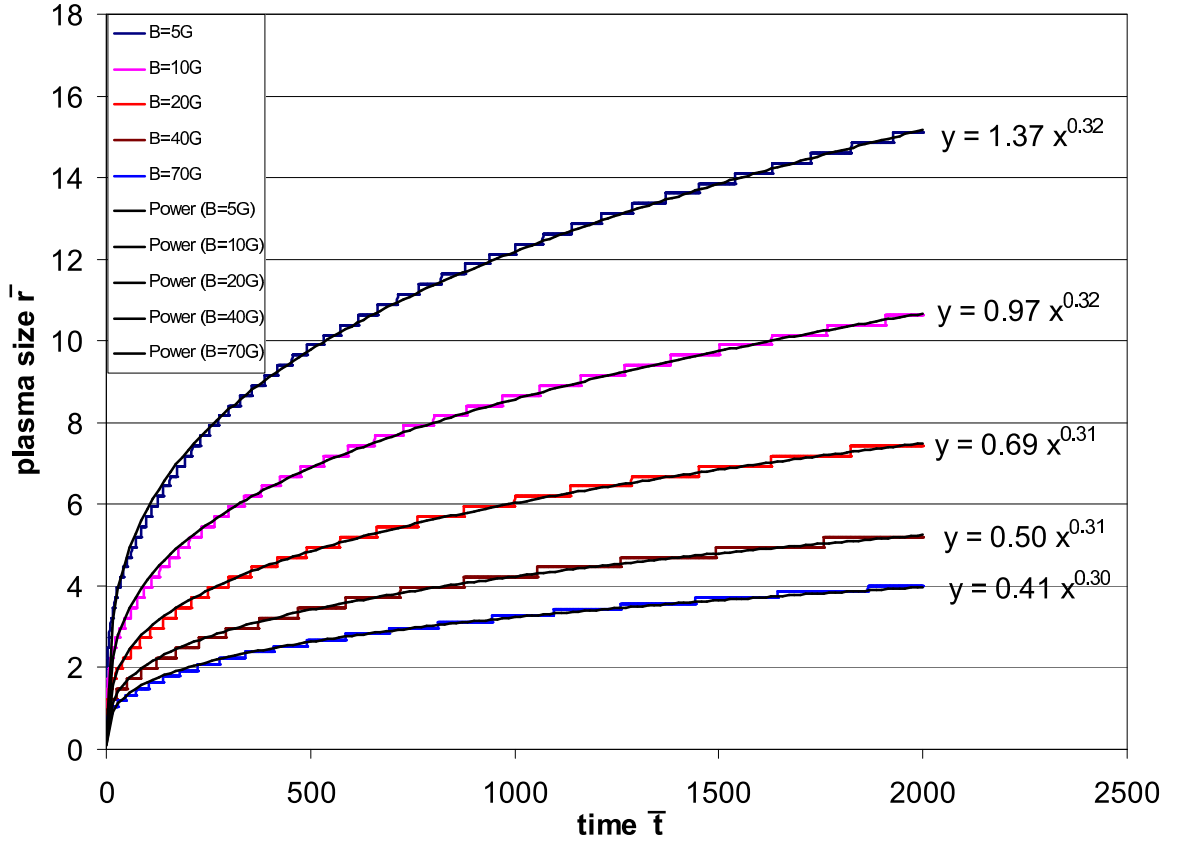
Figure 3.9: Numerical simulation of eqn 3.3 with the electron temperature evolution given by eqn 3.4. The curves are for B = 5, 10, 20, 40 and 70 G from top to bottom with power law fitting of $\tilde{t}^{\,0.3}$.

to extract electron temperatures, we can get the electron temperature evolution up to 70 μs, which roughly follows $T_e \propto t^{-1.2}$ for $T_{e0} = 3K$ [26]. We use the following empirical equation as our electron temperature evolution:

$$
\begin{aligned}
T_e &= T_e(0)/(1 + t^2/\tau_{\|0}^2), t < 20\mu s \\
T_e &= T_e(20\mu s)t^{-1.2}, t \geq 20\mu s.
\end{aligned}
\tag{3.4}
$$

By numerically solving eqn 3.3 with the electron temperature evolution given by eqn 3.4, we find the transverse size evolution for different magnetic fields from 5 G

to 70 G as shown in figure 3.9. The curves are for B = 5, 10, 20, 40 and 70 G from top to bottom with power law fitting of $\tilde{t}^{\,0.3}$. We then extract the transverse expansion velocity as a function of magnetic field from the transverse size evolution, shown as the red curve (triangles) in figure 3.8. The simulation result is in good agreement with the experimental data, which shows the transverse expansion velocity scales as $B^{-1/2}$. Therefore ambipolar diffusion can explain the B-dependence when the expansion dynamics are included. Using self-similar arguments for the diffusion [62], it can be shown that $r \propto B^{-1/2}t^{(1+\Delta)/4}$, where $T_e \propto t^{-\Delta}$ (note that $r \propto t^{0.55}$ for $\Delta = 1.2$ in the self-similar arguments, which is different from the numerical simulation result $r \propto \tilde{t}^{\,0.3}$. This is because the self-similar arguments only consider the transverse diffusion term in eqn 3.3). By taking the derivative of r, we find an expansion velocity scaling as $B^{-1/2}$, as observed. Even if the electron temperature evolution in the presence of magnetic field is different from eq. 3 (different Δ), it will only change the time-dependence of the transverse size, not the $B^{-1/2}$ scaling of the above self-similar argument. This scaling of the transverse size (expansion velocity) is the result of the electron density dependence of the tranverse ambipolar diffusion rate, while that of other low temperature plasmas is density independent and yields the usual B^{-1} dependence of the characteristic transverse decay distance. Bohm diffusion also has the same $B^{-1/2}$ dependence of the transverse size for our UCP systems if we assume $D_\perp \propto T_e/eB$. However, the plasma will quickly stop expanding in a very short time ($< 20~\mu$s) if we assume only Bohm diffusion is involved, because the Bohm diffusion rate is proportional to T_e. The ambipolar diffusion rate is inversely proportional to $T_e^{1/2}$, and should dominate Bohm diffusion

at later times which is consistent with the abscence of any signature of plasma instabilities.

In conclusion, we have developed a method to study the transverse expansion of an ultracold plasma in a magnetic field by using a high voltage pulse to image the ion distribution onto a position sensitive detector. The expansion velocity roughly scales as $B^{-1/2}$ for magnetic field up to 70 G, and is in good agreement with a nonlinear ambipolar diffusion model. Future work will focus on a full 3D confinement of the ultracold plasmas by using a magnetic mirror geometry (magnetic bottle). This will allow us to study the plasmas for a longer times, up to several milliseconds.

Chapter 4

Ultracold Plasma Instability

4.1 Overview

Ultracold plasmas (UCPs), described in chapter 1, have well-controlled initial conditions (plasma size, density and temperature), very low temperature, inhomogeneous and non-equilibrium properties. Such plasmas can support stable collective modes [16, 43, 31, 22], as well as develop instabilities [63]. Plasma instabilities usually involve plasma waves that grow exponentially from small perturbations to large amplitudes or even faster. Much of the quest for fusion energy involves control and suppression of plasma instabilities [64]. They occur in all kinds of plasmas, including space plasmas [65, 66, 67], dusty plasmas [68], magnetically confined plasmas [69], and Hall thruster plasmas for spacecraft propulsion [70, 71, 72, 73].

In this chapter, we present the first observation of a plasma instability in an UCP. By applying a small magnetic field ($\sim$ 2 G) perpendicular to an applied electric field ($\sim$20 mV/cm), we observe periodic pulsed emission of electrons from an expanding UCP, with a frequency range from 50 to 500 KHz. Using a time-of-flight (TOF) electron projection imaging technique [41], we image the electron spatial distributions by extracting them with a high-voltage pulse and accelerating them onto a position-sensitive detector. We observe that these electron projection images split into two or three lobes in the $E \times B$ direction, coincident with the

observation of periodic electron emission signals. This provides strong evidence for a plasma instability in the expanding UCP due to electrons drifting relative to the ions across the magnetic field. A high-frequency electron drift instability [72, 73] quantitatively matches our observation, which has a frequency lower than the electron gyrofrequency and a short wavelength on the order of the electron gyroradius due to the coupling between the electron drift wave and an harmonic of the electron gyrofrequency. The high-frequency drift instability has been studied in Hall thruster plasmas [70, 71, 72, 73], which can develop oblique unstable modes perpendicular to the magnetic field and induce large currents across magnetic field lines.

4.2 Observation of an Ultracold Plasma Instability

The electron emission signal in a longitudinal magnetic field $B_\parallel$ (which is along the applied electric field E) is similar to that of zero-field case except for some variations in the expansion dynamics (UCP expansion dynamics in a large $B_\parallel$ is studied in chapter 3 by TOF projection imaging [42]). The emission signal consists of a prompt peak (initially escaped electrons) followed by a region of little electron loss where the quasineutral plasma state forms. This is followed by a long $\sim$150 μs loss of electrons, interpreted as the decay of the plasma as electrons spill out of the potential well that continuously decreases in depth with plasma expansion.

The electron emission signal with a small transverse magnetic field $B_\perp$ (which is normal to the applied electric field E direction) is dramatically different from
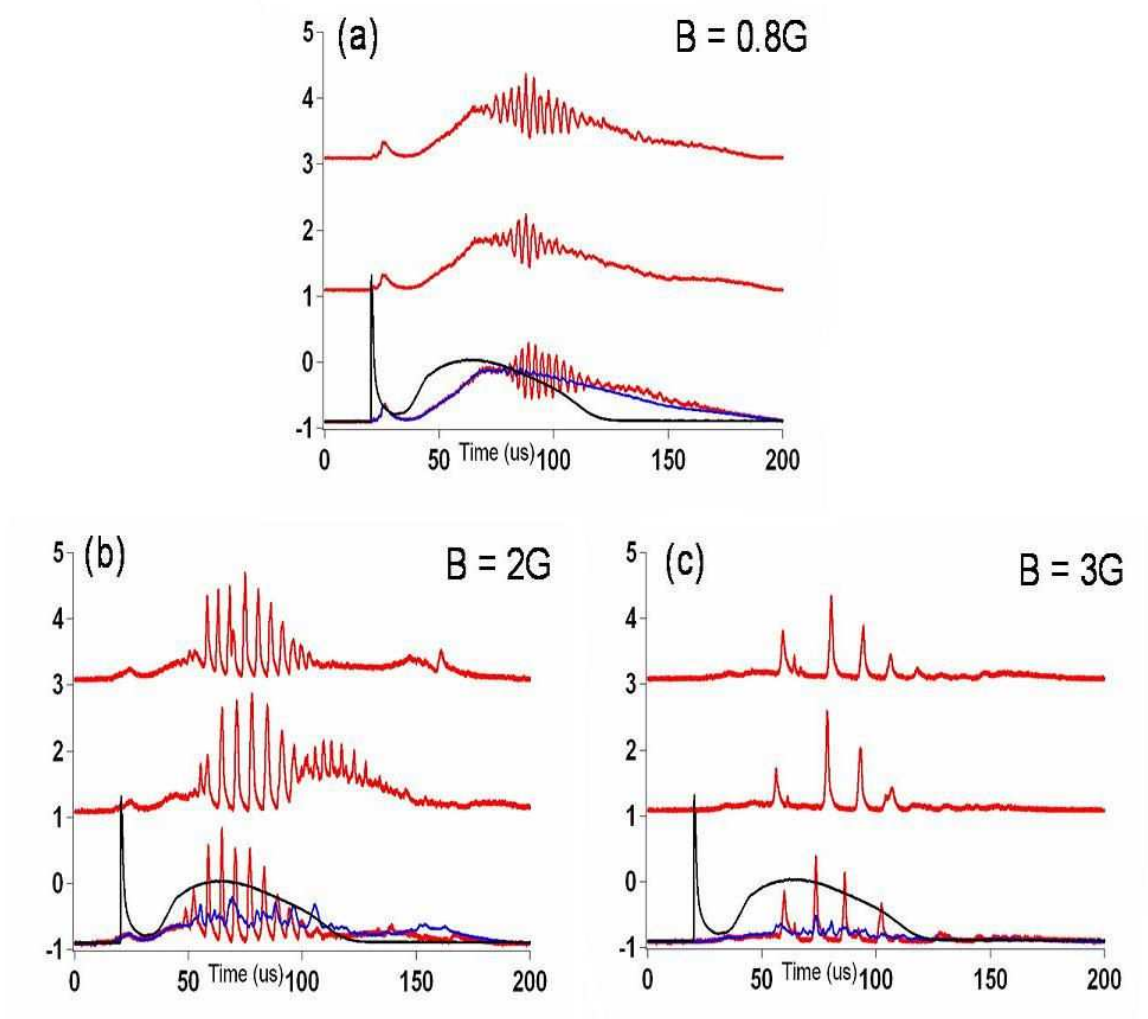
Figure 4.1: Electron emission signals for constant E and different $B_\perp$. (a)-(c) constant E of 10 mV/cm and different $B_\perp$ of 0.8, 2 and 3 G, respectively. The red curves (with large periodic emission) are single shot; the blue curve (with much less periodic emission) is the average of 40 shots. the black curve (with large prompt peak) is the electron signal without a magnetic field. The emission frequency increases as we decrease $B_\perp$.

Figure 4.2: Electron emission signals for constant $B_\perp$ and different E. (a)-(c) $B_\perp$ of 1.5 G and different E of 7, 20 and 33 mV/cm, respectively. The red curves (with large periodic emission) are single shot; the blue curve (with much less periodic emission) is the average of 40 shots. the black curve (with large prompt peak) is the electron signal without a magnetic field. The emission frequency increases as we incease E.
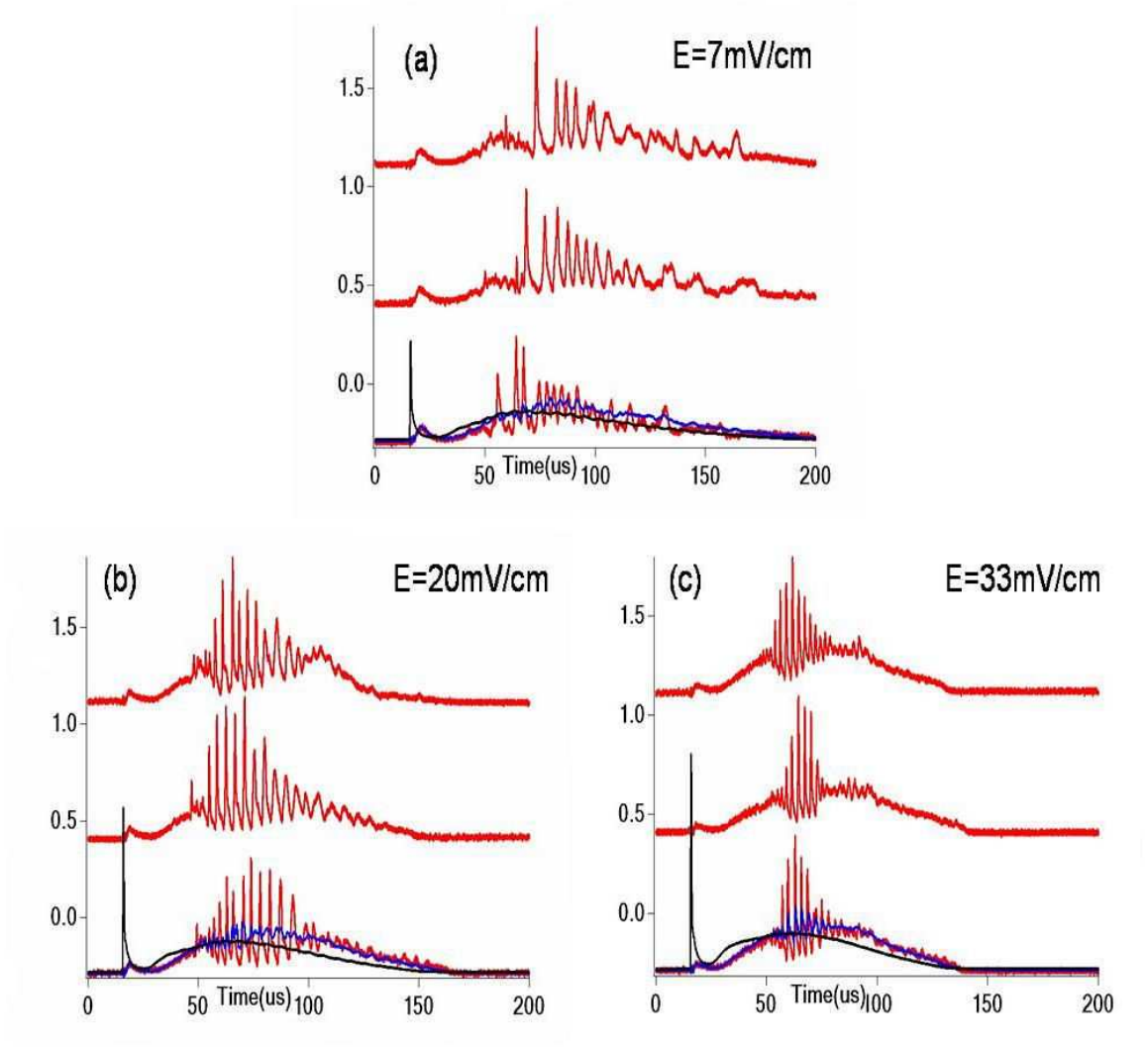
92

that with a small $B_{\parallel}$. We observe periodic pulsed electron emission even with a very low $B_{\perp}$, as shown in Figure 4.1a-4.1c. The black curve in Figure 4.1 is the typical electron emission signal from a freely expanding UCP for $T_{e0} = 100$ K. The red curves (with large periodic emission) are single shot; the blue curve (with much less periodic emission) is the average of 40 shots. As we increase $B_{\perp}$ from zero to about 0.8 G, the electron signal starts to show periodic emissions, which appear at about 30-50 μs after the formation of the plasma with frequency of several hundred KHz. The three traces in each panel of Figure 4.1 correspond to individual single realizations of the UCP. Note that the emissions have similar character for each shot, although the phases are random. As we continue to increase $B_{\perp}$ to about 2 G (Figure 4.1b), the amplitude of the emissions increase, comparable to the prompt peak in the absence of a magnetic field. The frequency decreases to 50-100 KHz and the prompt peak shrinks. At a field of 3 G, the electron emission signal almost vanishes except for few peaks(Figure 4.1c).

The oscillation frequency and amplitude in the electron emission signal also depends on the applied electric field E (figure 4.2a-4.2c). The magnetic field is 1.5 G, and the electric fields are 7, 20 and 33 mV/cm for figure 4.2a, 4.2b and 4.2c respectively. The frequency increases and the amplitude of the emissions decreases as we increase E, which is similar to the case of decreasing $B_{\perp}$. Using fast Fourier transform (FFT) of the electron signals in figures 4.1 and 4.2, we can extract the oscillation frequency as a function E/B (electron drift velocity V_d) as shown in figure 4.3, which clearly shows that the oscillation frequency depends linearly on the drift velocity with a slope of 10.2 ± 0.2 m^{-1}.
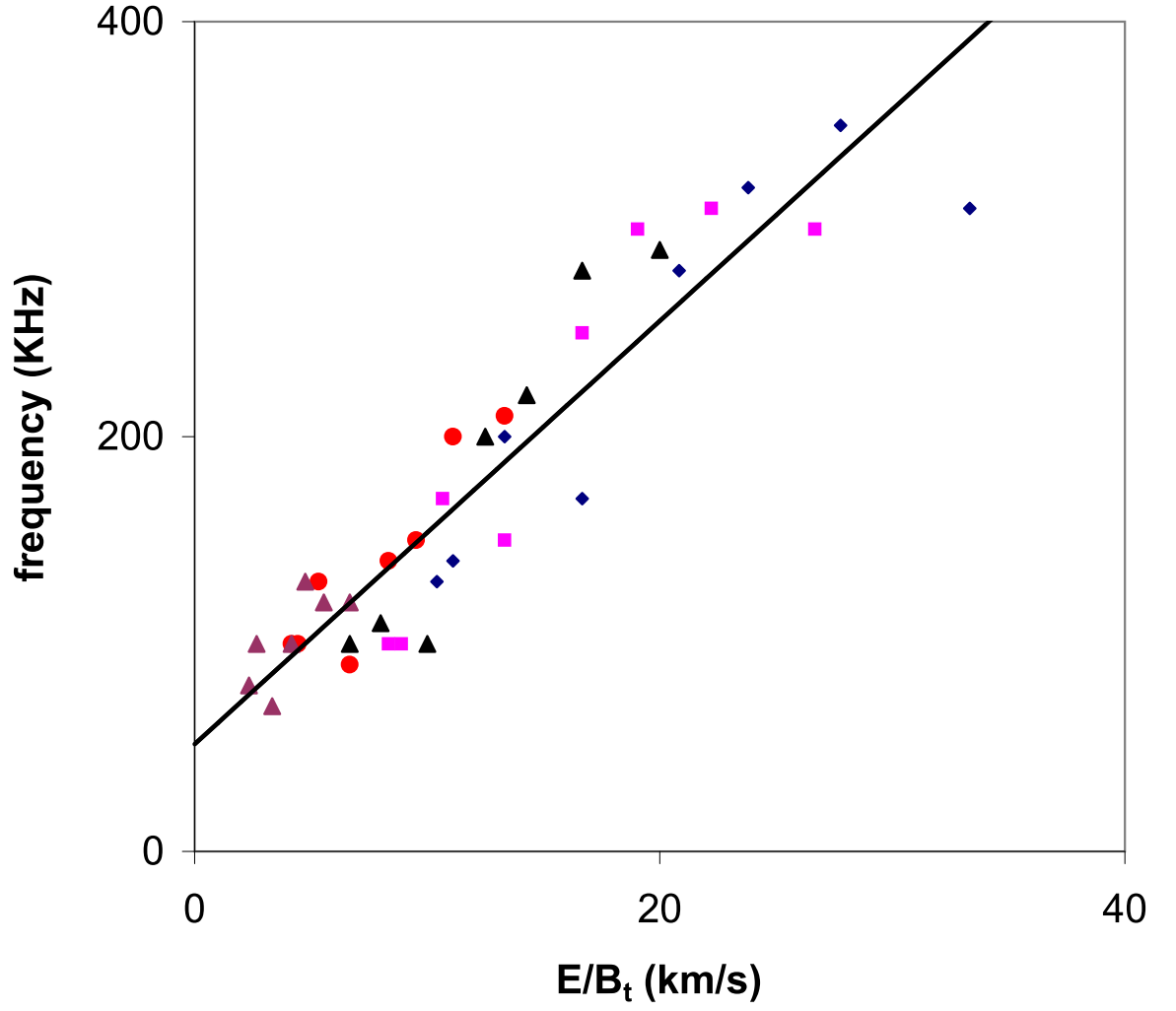
Figure 4.3: The emission frequency as a function of $E/B_\perp$; each symbol for varying $B_\perp$ from 1 to 3.2 G and constant E; different symbol for varying E from 7 to 33 mV/cm and constant $B_\perp$. The emission frequency is linearly dependent on the electron drift velocity V_d with a slope of 10.2 ± 0.2 m^{-1}.
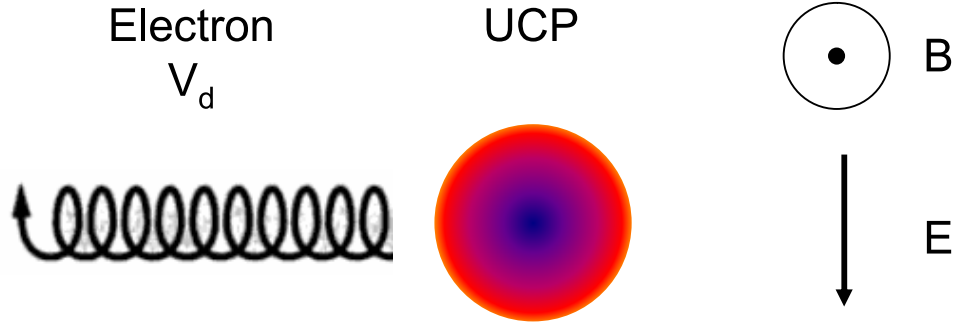
Figure 4.4: Electrons drift in crossed electric and magnetic fields.

4.3 High Frequency Electron Drift Instability

There are many different instabilities in plasmas, but given our plasma parameters we can constrain possible choices to a small number. We identify the periodic electron emission signals as a signature of a plasma instability due to electrons drifting relative to ions across the magnetic field. The crossed magnetic and electric fields drive the electrons to drift with a velocity V_d ($V_d = E/B_\perp$) in the $E \times B_\perp$ direction (as shown in figure 4.4). The ions are unmagnetized, not affected by the small $B_\perp$, due to their large mass (the ion gyroradius is much larger than the UCP size and the ion gyro-period is much longer than the UCP lifetime). In our UCP the electrons are unmagnetized in the first $\sim$30 μs because the electron gyroradius is about the same order of magnitude as the UCP size and the electron collision rate is higher than the electron cyclotron frequency f_{ce}. As the UCP expands, the plasma size increases, the plasma density decreases, and T_e decreases (due to various cooling mechanisms) [26]. The electrons become magnetized at about 30-50 μs because the electron collsion rate starts to be less than f_{ce} and the plasma size at

95
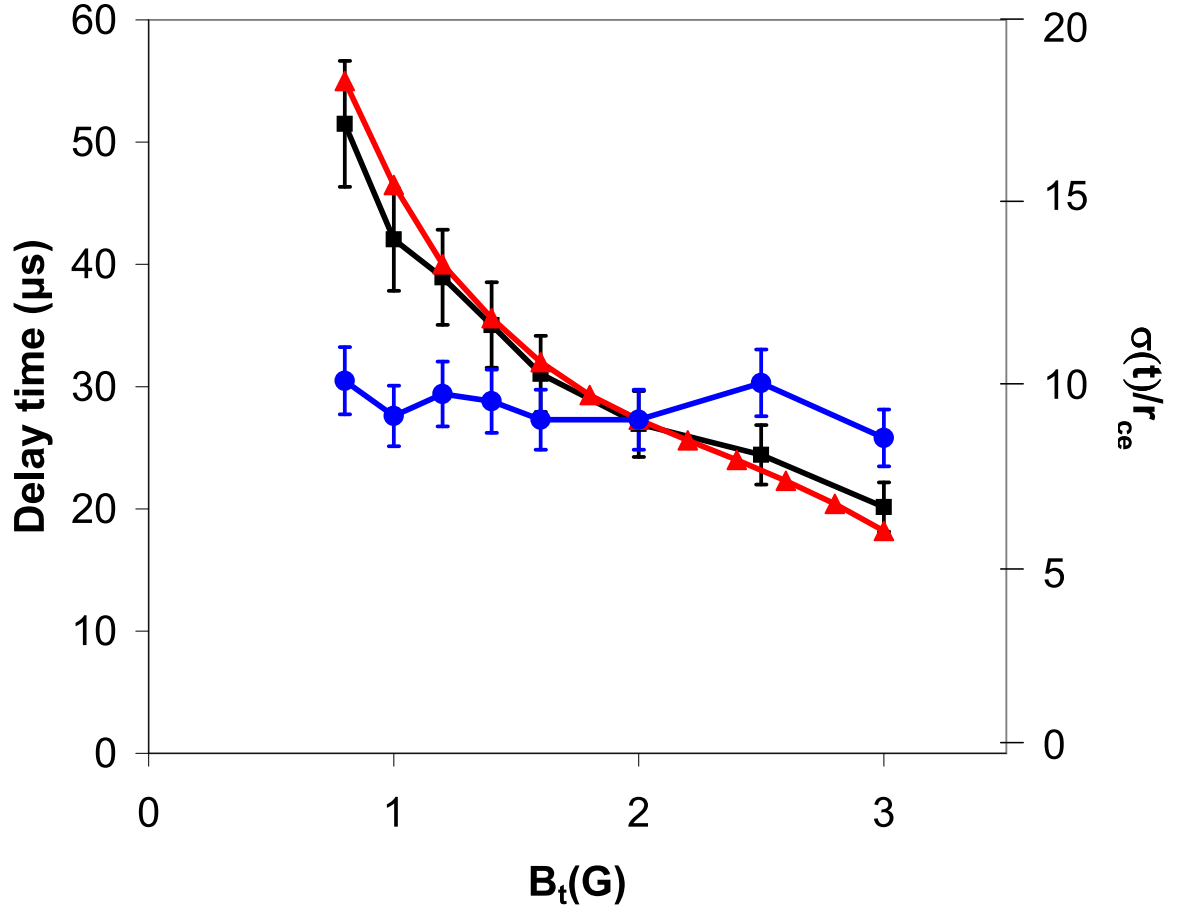
Figure 4.5: The delay time and $\sigma(\mathbf{t})/\mathbf{r_{ce}}$ VS magnetic field. The delay time when the electron signals start to have periodic emissions in Figure 4.1 (square points) and the ratio of plasma size to the electron gyroradius at that time (circle points) as a function of transverse magnetic field. The red curve with triangle points is the theoretical calculation of the delay time when the electron collision rate equals to the electron gyrofrequency. The error bars represent the 1σ standard uncertainty in the average of 40 single shots.

that time is about ten times larger than the electron gyroradius, which is consistent with our observation that the periodic emissions start at the same time. Figure 4.5 is the delay time (square points) when the electron signals start to have periodic emissions as a function of B_t, which agrees with the theoretical calculation of the delay time (triangle points) when the electron collsion rate equals to the electron gyrofrequency using the empirical equation as our electron temperature evolution in eqn 3.4 [24, 26, 42]. The plasma size (circles) at that delay time is about a factor of 10 larger than the electron gyroradius which also indicates that the electrons are magnetized after the electron signals start to have large periodic emissions (note the ratio between the plasma size and the Debye length is about 45 at the start time of the periodic emission of electron, so the electric field can not penetrate the plasma except for the edge region). The frequency is in the range from 50 KHz up to a few hundred KHz, which is much larger than the ion cyclotron frequency f_{ci} ($\sim$12 Hz at 1 G) and much less than electron cyclotron f_{ce} ($\sim$2.8 MHz at 1 G) and the electron plasma wave f_{pe} which is about 10-20 MHz at the delay time of about 30-50 μs. The periodic emission signal is roughly independent of plasma density (or plasma frequency) as shown in figure 4.1 and 4.2 (note that the plasma density drops by a factor of 8 from 50 μs to 100 μs). There are periodic emissions with different frequencies (Fig. 4.1b and 4.2a), which also indicates that we have plasma instability (mode switching) in the crossed-field configuration.

A candidate instability is the high-frequency electron drift instability, which has been studied in Hall thruster plasmas (a type of plasma-based propulsion systems for spacecrafts) experimentally [70, 71] and theoretically [72, 73] in the past few
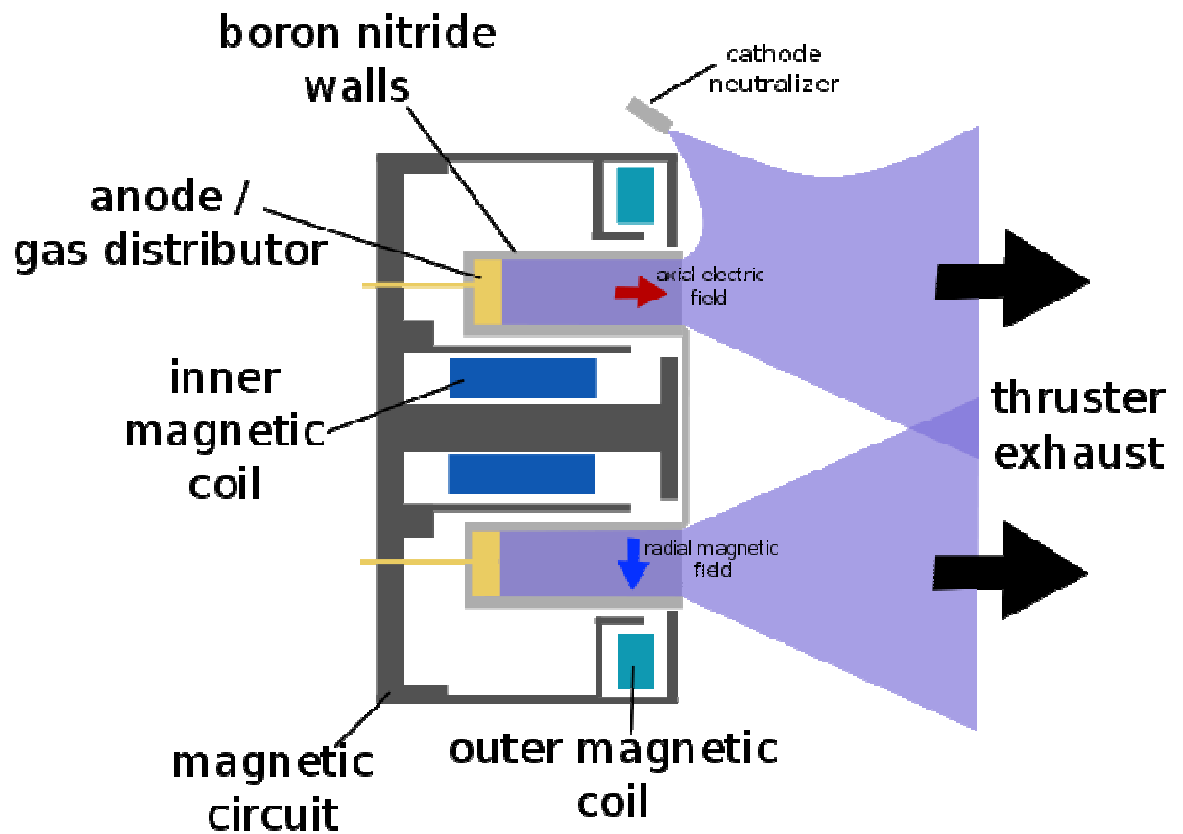
97

Figure 4.6: A schematic of a Hall thruster which is from http://en.wikipedia.org/wiki/Hall_effect_thruster. It is a type of plasma-based propulsion systems for spacecrafts.

years to explain the transport of electrons across magnetic field lines. The essential working principle of the Hall thruster is that it uses an electrostatic potential to accelerate ions up to high speeds (a schematic of a Hall thruster is shown in figure 4.6). The attractive negative charge is provided by an electron plasma at the open end of the thruster instead of a grid. A radial magnetic field of a few hundred Gauss is used to hold the electrons in place, where the combination of the magnetic field and an attraction to the anode force a fast circulating electron current around the axis of the thruster and only a slow axial drift towards the anode occurs. A 2D fully kinetic model of the Hall thruser developed in ref. [72] has demonstrated that the large drift velocity at the exhaust of the thruster was the source of an instability that gives rise to plasma turbulence and could induce a significant current across the magnetic field. It is a high-frequency electron drift instability with frequency f_r lower than f_{ce} and short wavelength close to the electron gyroradius r_{ce}, which is studied in ref. [73].

The theory of high-frequency electron drift instability is developed from the dispersion equation of electrostatic waves in a hot magnetized electron beam drifting across a magnetic field with unmagnetized cold ions, and is closely related to the ion-acoustic-wave instabilities in other plasma systems, such as non-specular radar meteor trails [65], the ionosphere of the Earth [66, 67], dusty plasmas [68] and magnetic pulses [69], but they usually restrict the analysis to the cases where the drift velocity V_d is much smaller than the electron thermal velocity V_{eth}. For high-frequency electron drift instabilities in Hall thrusters and here, V_d is about the same order of magnitude as V_{eth}, and much larger than the magnetic field gradient drift

velocity and the density gradient drift velocity.

Assuming an electrostatic field perturbation $\phi = \phi_0 \times \exp(\mathrm{i}k \cdot r - \mathrm{i}(2\pi f)t)$ and a Maxwellian electron distribution function with mean velocity V_d and temperature T_e, the dispersion equation can be written in the limit $k_z = 0$ (where k_z is the wavenumber along $B_\perp$) [73]:

$$k_{xy}^2 \lambda_D^2 \left(1 - \frac{m}{M}\frac{f_{pe}^2}{f^2}\right) = \sum_{n=1}^{n=\infty} \frac{2(f - k_y V_d/2\pi)^2 I_n(b)e^{-b}}{(f - k_y V_d/2\pi)^2 - (nf_{ce})^2} + (I_0(b)e^{-b} - 1) \tag{4.1}$$

where k_{xy} is the wavenumber in the plane perpendicular to $B_\perp$; $\lambda_D^2 = k_B T_e/m(2\pi f_{pe})^2$ is the Debye length; k_y is the wavenumber in the $E \times B_\perp$ direction, and $b = k_y^2 V_{eth}^2/(2\pi f_{ce})^2$. The functions I_n are modified Bessel functions of order n.

A further approximation is to neglect the perturbations perpendicular to the drift motion ($k_x = 0$, the wavenumber along E) because the electron drift velocity V_d is about an order of magnitude larger than the density gradient drift velocity. In this limit, we get the following dispersion relation equation:

$$k_y^2 \lambda_D^2 \left(1 - \frac{m}{M}\frac{f_{pe}^2}{f^2}\right) = \sum_{n=1}^{n=\infty} \frac{2(f - k_y V_d/2\pi)^2 I_n(b)e^{-b}}{(f - k_y V_d/2\pi)^2 - (nf_{ce})^2} + (I_0(b)e^{-b} - 1) \tag{4.2}$$

In a qualitative picture of the instability from the dispersion relation equation 4.2, the instability can only occur when $(f - k_y V_d/2\pi)^2 - (nf_{ce})^2 = 0$, that is, $k_y V_d/2\pi \approx nf_{ce}$ for $f \ll f_{ce}$. So the instability is due to the coupling between the electron drift motion and the electron cyclotron motion. In order to find the dependence of f_r (real component) and f_i (imaginary component) on the
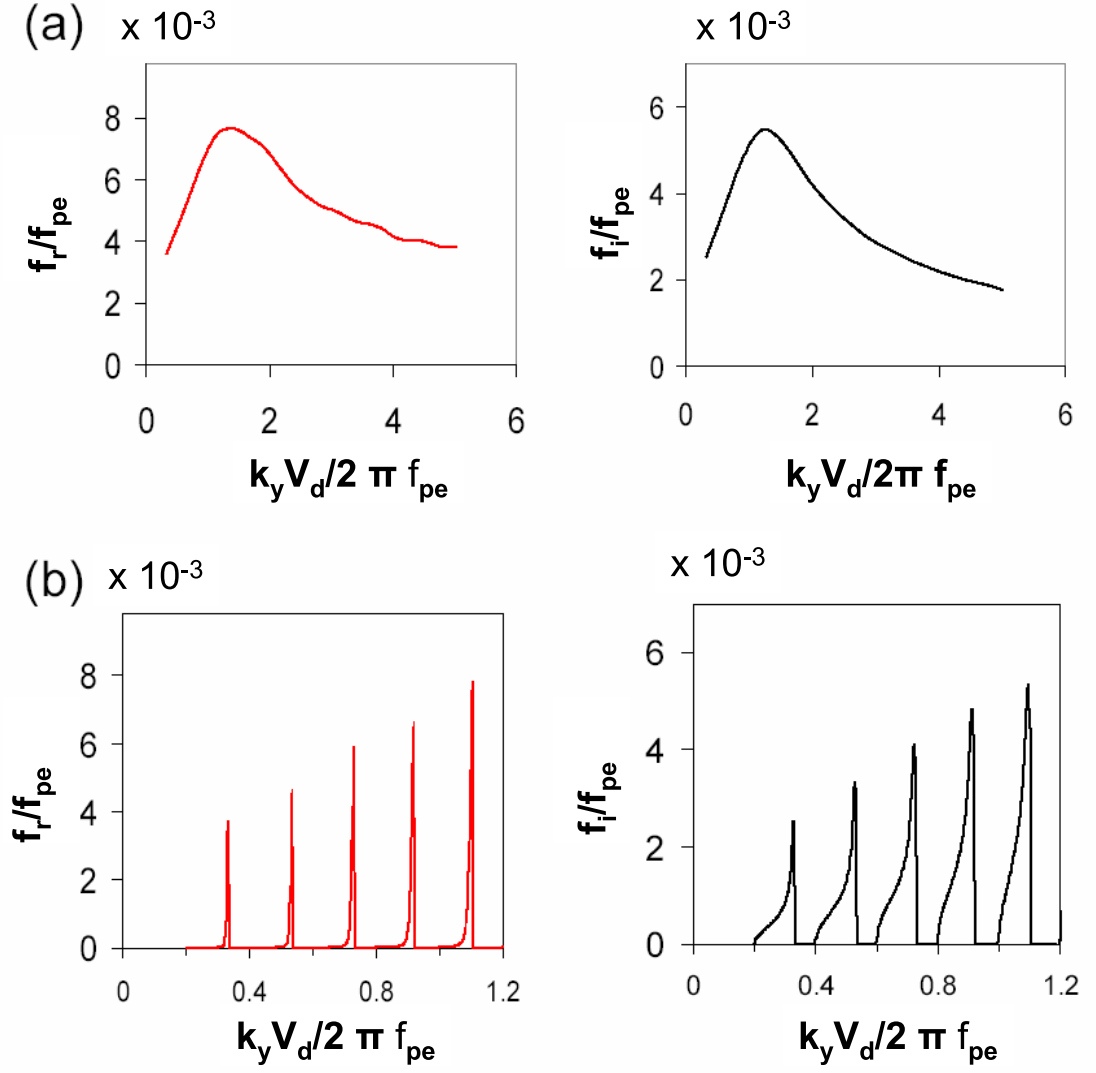
Figure 4.7: Numerical solutions of the 1D dispersion relation of equation (1) as in [73], but for our condition. (a) represents the envelopes of the real (frequency) and the imaginary (growth rate) as a function of $k_y V_d/(2\pi f_{pe})$. (b) the corresponding ones for small wavenumbers. The electron cyclotron frequency is equal to $0.2 f_{pe}$, and $V_{eth}/V_d = 0.5$.

wavenumber k_y quantitatively, we numerically solve equation 4.2. Figure 4.7 shows the frequency and the corresponding growth rate of the unstable modes as a function of k_y. Figure 4.7a and 4.7b are the envelopes of the solutions and the first 5 modes, respectively. The values of f_r for the maximum growth rate correspond to frequencies ranging from 90 KHz to 140 KHz for $f_{pe} = 21$ MHz, $B_\perp = 2$ G, $E = 20$ mV/cm and $T_e = 2.7$ K at delay time of about 30 μs (where T_e is from [26]), which agrees with the measured frequencies at $V_d = 10^4$ m/s in Fig. 4.3. The ratio of the frequency to the drift velocity is about 9-14 m^{-1}, in agreement with the measured slope of Fig. 4.3 (10.2 m^{-1}). The maximum of the growth rate is reached for $k_y V_d/(2\pi f_{pe}) = 1.2$, and the corresponding wavelength is about 0.5 mm, close to the electron gyroradius (about 0.2 mm for $B_\perp = 2$ G and $T_e = 2.7$ K). We can also see the transitions from stability to instability whenever $k_y V_d/(2\pi f_{pe})$ is close to a cyclotron harmonic $n f_{ce}/f_{pe}$. The growth rate reaches a maximum and then decreases sharply between each cyclotron harmonic, and is separated by stable regions. The frequency is several orders of magnitude below the growth rate except in the vicinity of the maximum.

The frequency roughly linearly depends on the drift velocity (below $k_y V_d/(2\pi f_{pe}) = 1$), but is independent of the plasma frequency (i.e., plasma density) before the frequency reaches the maximum value (both axis are scaled by electron plasma frequency in Fig. 4.7a), which explains the lack of density dependence seen in Fig. 4.1 and 4.2. We measure the growth rate by suddenly applying the electric field at different delay times (Fig. 4.8), and find the periodic emission occurs within 1-2 μs after application of the field, corresponding to a growth rate of $\sim$ 100-150 KHz for
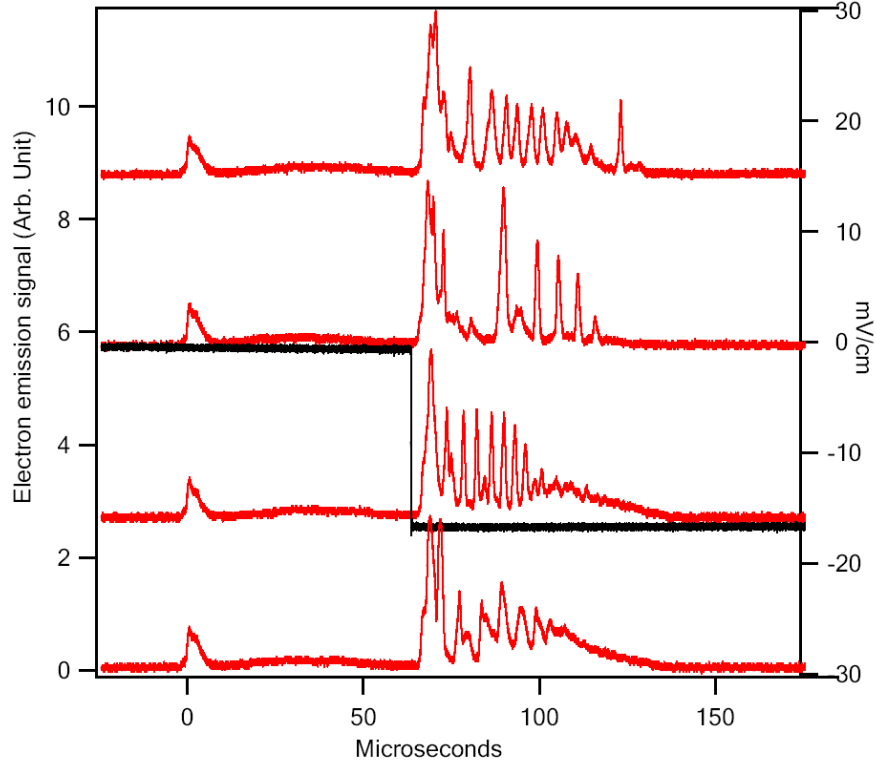
Figure 4.8: Typical electron emission signals with a pulsed electric field to measure the growth rate. The red curves are single shot; the back curve is the pulsed electric field which is turned on at specific time after the formation of the plasma. the electric field E is 18 mV/cm and the transverse magnetic field is 2 G.

$B_\perp = 2$ G and $E = 20$ mV/cm, which is about the same as the frequency f_r, and consistent with the calculated growth rates.

By taking into account the perturbation perpendicular to drift direction in the plane perpendicular to B_t, it has been shown in [73] that the unstable modes extend over a very large range of $k_x \lambda_D / \omega_{pe}$ in the 2D results, and the instability persists with large growth rates even for k_x close to k_y, that is, the instability can develop

in packets of unstable modes in the plane perpendicular to the magnetic field which could induce a significant current across the magnetic field lines.

Note that the applied magnetic field should suppress electron detection, since it is transverse to the detector direction. This is seen in the strong suppression of the prompt electron emission peak (Figure 4.1 and 4.2). Nevertheless, we detect large pulses of electrons, presumably due to large electron trajectories that extend past the grid (1.5 cm below the plasma) where the large acceleration field can direct the electrons to the detector, even in the presence of the transverse magnetic field.

4.4 Electron Projection Images in the Crossed-field Configuration

We use the same TOF projection imaging technique for electrons as that for ions (the ion images during instabilities in the crossed-field configuration look Gaussian, that is, the ions did not see the small magnetic field as expected.)[42]. Figure 4.9 shows the electron images at different delay times after the formation of the UCP for different $B_\perp$ and E. All the images are single shot, with little variation from shot to shot. In the absence of a magnetic field (Fig. 4.9a), the electron images show a Gaussian density profile. Figure 4.10 is the measured electron image spatial distribution in the absence of a magnetic field as a function of elapsed time after the formation of UCP. The black curve with dots is the measured electron size extracted from the 2D Gaussian fitting of the electron images. The brown curve with triangles is the electron size with the scaling factor due to the electron lensing effect, which is consistent with the theoretical calculation electron cloud size with
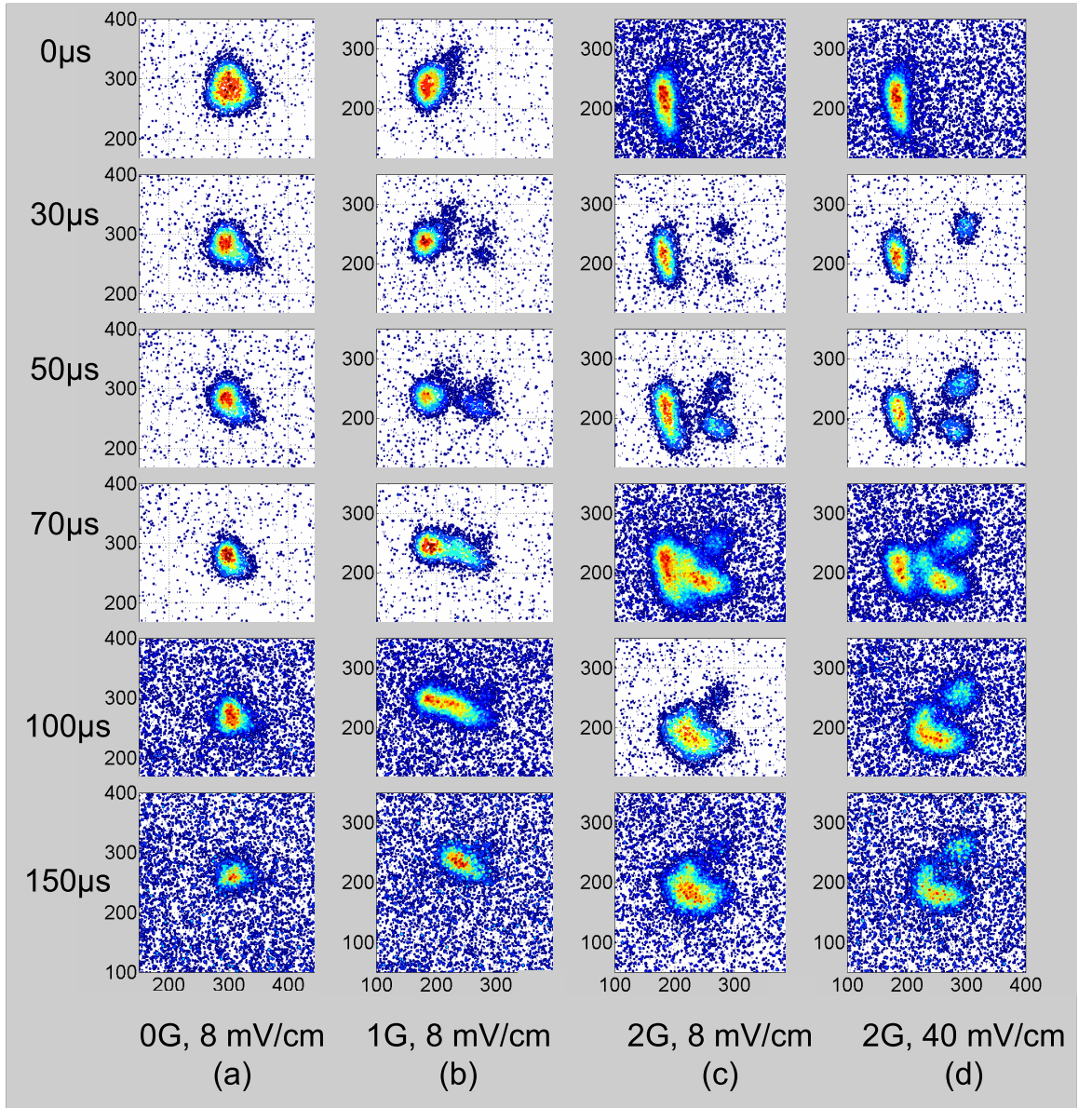
104

Figure 4.9: Electron projection images in weak crossed magnetic field and electric field. All the units of the images here are in pixels, and one pixel is about 150 μm.

100 ns Coulomb explosion time (the red curve with unfilled squares), which also takes into account electron loss due to the evaporation of electrons from the system. We assume that the ion cloud follows a ballistic expansion model (the blue curve with diamond points), while the electron distribution is initially identical to the ion distribution, but with a truncation at the appropriate radius such that the total electron number agrees with the measured charge imbalance at a specific delay time. We then perform self-consistent calculations for the plasma potential to extract the final electron cloud size (the magenta curve with square points) [50]. The electron lensing factor is obtained from the SIMION 3D trajectory simulation with the actual voltage settings of the grids, the spacings between the grids and detector, and the ion spatial distribution. We should point out that the electron lensing factor, unlike that of the ions, is not a constant during the whole UCP lifetime due to the strong Coulomb force of the ion cloud on the much lighter electrons, especially for the first 30 μs. The electrons are removed from the plasma in a few nanoseconds after applying the high-voltage pulse, but the ions maintain their Gaussian spatial distribution during that short period of time. This exerts a strong Coulomb force on the electrons and partialy cancels the applied electric field increasing the electron lensing factor as confirmed by the SIMION trajectory simulation. As the plasma expands, the Couloumb force on the electrons gets smaller, and the electron lensing factor tends towards a constant at later times (after 30 μs). The ion lensing factor is constant because there are no electrons left during the ion Coulomb explosion phase.

As we increase $B_\perp$ to about 1 G (Fig. 4.9b), the electron images start to split
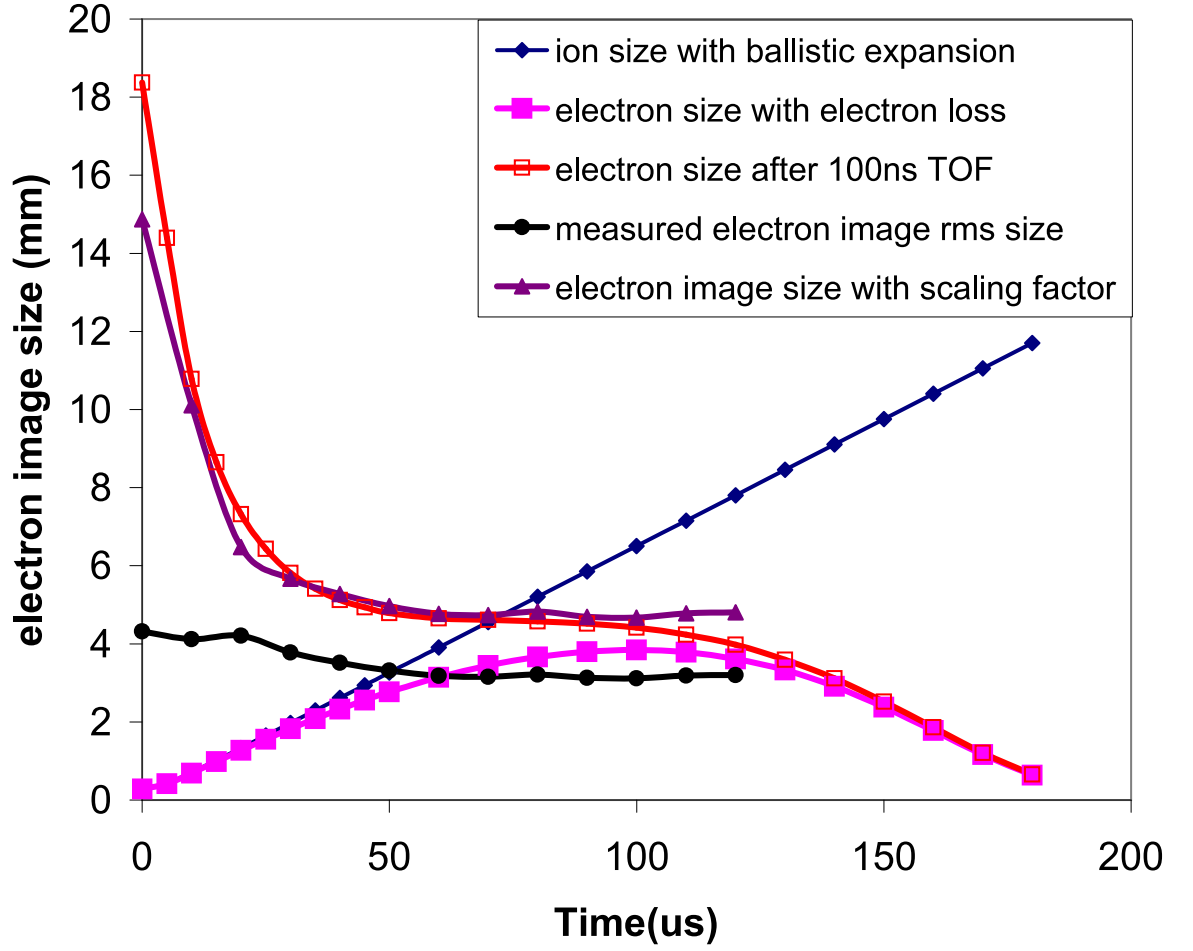
Figure 4.10: The electron sizes of UCPs as a function of time for $T_e = 100$ K and B = 0 G. The black curve with dots is the electron cloud size extracted from the 2D Gaussian fitting of the electron images. The brown curve with triangles are the electron cloud size with the scaling factor due to the charged particle lensing effect. This is consistent with theoretical calculations of electron cloud size with 100 ns Coulomb explosion time (the red curve with unfilled squares).

into two lobes at about 30 μs, coincident with the observation of large periodic electron emission signals. At about 2 G, we observe up to 3 lobes in the electron images between 30 μs and 70 μs (Fig. 4.9a and 4.9d). The extra electron lobes are in the E$\times B_\perp$ direction, and they show up in the other side of the main electron cloud if we change the sign of $B_\perp$. We did not observe any changes in the ion images and ion current in the cross-field configuration compared to those without a magnetic field. This is surprising, as one expects the electron distribution to closely follow the ion distribution for an UCP, and these structures do not explain the electron emission signal.In order to confirm that the extra lobes of the electron images are coming from the plasma itself, rather than dynamics during TOF, we took a series of images at different extraction parameters such as the high-voltage amplitude and width and the accelerating voltages on the middle and front grids (located between the plasma and the detector that strongly affect the sizes of electron images). We always observe the similar results as Fig. 4.9, implying this is a valid measure of the plasma electron distribution. Using a simple model of the electron space charge effects during TOF, we find the separation between the main cloud and the extra lobes before time of flight to be about 0.5-1σ_t, where σ_t is the plasma size at delay time t (figure 4.11). That is, the extra lobes are located inside the plasma. These large scale density structures only appear under conditions of periodic electron emission, and thus must be tied to the instability. Our identification of high-field drift instability does not rely on these density modulations, and in fact we have no theory that connects the observed temporal behavior with the spatial features.

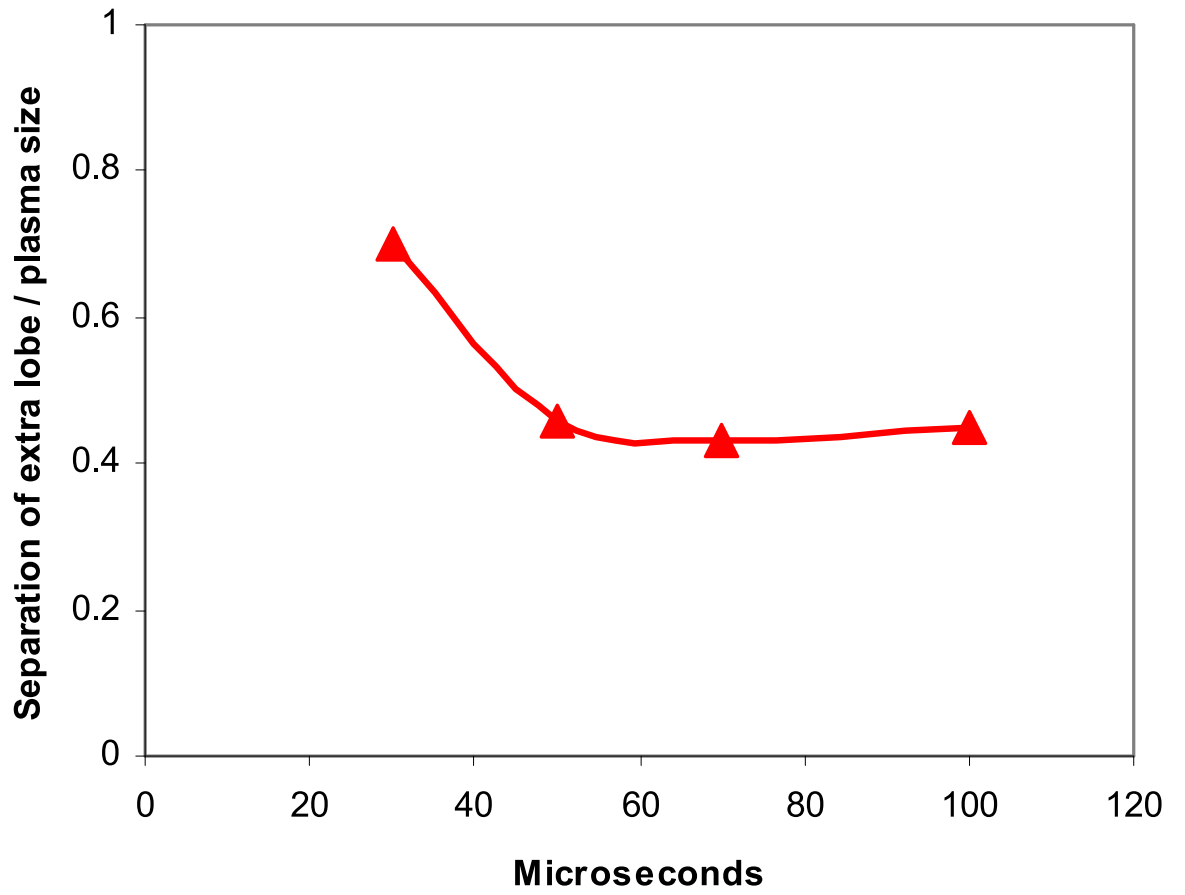In summary, we have observed large periodic electron emission and splitting

Figure 4.11: The normalized separation between the main cloud and the extra lobes before time of flight relative to the plasma sizes. The extra lobes are located inside the plasma, which is at about $0.5\text{-}1\sigma_t$ position.

of the electron distribution into two or three lobes from an expanding UCP in the presence of crossed magnetic and electric fields. We identify them as a signature of high-frequency electron drift instability due to the electrons drifting relative to the ions across the magnetic field. We calculate the unstable mode frequencies and growth rates by solving a 1D dispersion equation and find good agreement. The large scale changes in the electron spatial distribution remain unresolved, as does the exact mechanism that leads to the emission of electrons, which need investigation to fully understand the dynamics of ultracold plasmas in the crossed-field configuration as well as the associated instability. This work shows that UCPs will continue to provide an interesting place to study fundamental plasma physics phenomena.

Future work on the plasma instabilities will focus on the study of the exact mechanism that leads to the emission of electrons as well as the large scale changes in the electron spatial distribution. The magnetic field is perpendicular to the detector axis, so the Larmor motion should prevent the electrons from making it to the detector, unless they undergo large orbits (> 1.5 cm, the distance between the plasma and the grids) that take them into a region of high electric field. Another possible explanation is that a small "polarization electric field" produced by the charge separation, due to the presence of crossed electric and magnetic fields, will generate a secondary drift along the detector axis, develope plasma instability, and make electrons to the detector. Our UCP is also inhomogeneous, and should also have density gradient drift along all directions, so a more precise 3D model for the high frequency electron drift instability is needed by taking into account density gradient and distortation of the electron distribution fuction due to electron loss

and the crossed electric and magnetic fields.

Bibliography

[1] T. C. Killian, S. Kulin, S. D. Bergeson, L. A. Orozco, C. Orzel, and S. L. Rolston. Creation of an ultracold neutral plasma. *Phys. Rev. Lett.*, 83, 4776 (1999).

[2] T. C. Killian, T. Pattard, T. Pohl, and J. M. Rost. Ultracold Neutral Plasmas. *Physics Reports*, 449, 77 (2007).

[3] E. L. Clark, K. Krushelnick, M. Zepf, F. N. Beg, M. Tatarakis, A. Machacek, M. I. K. Santala, I. Watts, P. A. Norreys, and A. E. Dangor. Energetic heavy-ion and proton generation from ultraintense laser-plasma interactions with solids. *Phys. Rev. Lett.*, 85, 1654 (2000).

[4] R. A. Snavely, M. H. Key, S. P. Hatchett, T. E. Cowan, M. Roth, T. W. Phillips, M. A. Stoyer, E. A. Henry, T. C. Sangster, M. S. Singh, S. C. Wilks, A. MacKinnon, A. Offenberger, D. M. Pennington, K. Yasuike, A. B. Langdon, B. F. Lasinski, J. Johnson, M. D. Perry, and E. M. Campbell. Intense high-energy proton beams from petawatt-laser irradiation of solids. *Phys. Rev. Lett.*, 85, 2945 (2000).

[5] A. Maksimchuk, S. Gu, K. Flippo, D. Umstadter, and V. Yu. Bychenkov. Forward ion acceleration in thin films driven by a high-intensity laser. *Phys. Rev. Lett.*, 84, 4108 (2000).

[6] J. Badziak, E. Woryna, P. Parys, K. Yu. Platonov, S. Jabłoński, L. Ryć, A. B. Vankov, and J. Wołowski. Fast proton generation from ultrashort laser pulse interaction with double-layer foil targets. *Phys. Rev. Lett.*, 87, 215001 (2001).

[7] A. J. Mackinnon, Y. Sentoku, P. K. Patel, D. W. Price, S. Hatchett, M. H. Key, C. Andersen, R. Snavely, and R. R. Freeman. Enhancement of proton acceleration by hot-electron recirculation in thin foils irradiated by ultraintense laser pulses. *Phys. Rev. Lett.*, 88, 215006 (2002).

[8] M. Hegelich, S. Karsch, G. Pretzler, D. Habs, K. Witte, W. Guenther, M. Allen, A. Blazevic, J. Fuchs, J. C. Gauthier, M. Geissel, P. Audebert, T. Cowan, and M. Roth. MeV ion jets from short-pulse-laser interaction with thin foils. *Phys. Rev. Lett.*, 89, 085002 (2002).

[9] T. Ditmire, J. W. G. Tisch, E. Springate, M. B. Mason, N. Hay, R. A. Smith, J. Marangos, and M. H. R. Hutchinson. High-energy ions produced in explosions of superheated atomic clusters. *Nature*, 386, 54 (1997).

[10] G. S. Sarkisov, V. Yu. Bychenkov, V. N. Novikov, V. T. Tikhonchuk, A. Maksimchuk, S.-Y. Chen, R. Wagner, G. Mourou, and D. Umstadter. Self-focusing, channel formation, and high-energy ion generation in interaction of an intense short laser pulse with a He jet. *Phys. Rev. E*, 59, 7042 (1999).

[11] K. Krushelnick, E. L. Clark, Z. Najmudin, M. Salvati, M. I. K. Santala, M. Tatarakis, A. E. Dangor, V. Malka, D. Neely, R. Allott, and C. Danson. Multi-MeV ion production from high-intensity laser interactions with underdense plasmas. *Phys. Rev. Lett.*, 83, 737 (1999).

[12] T. C. Killian, Y. C. Chen, P. Gupta, S. Laha, Y. N. Martinez, P. G. Mickelson, S. B. Nagel, A. D. Saenz, and C. E. Simien. Absorption imaging and spectroscopy of ultracold neutral plasmas. *J. Phys. B: At. Mol. Opt. Phys.*, 38, 351 (2005).

[13] C. E. Simien, Y. C. Chen, P. Gupta, S. Laha, Y. N. Martinez, P. G. Mickelson, S. B. Nagel, and T. C. Killian. Using absorption imaging to study ion dynamics in an ultracold neutral plasma. *Phys. Rev. Lett.*, 92, 143001 (2004).

[14] E. A. Cummings, J. E. Daily, D. S. Durfee, and S. D. Bergeson. Fluorescence measurements of expanding strongly-coupled neutral plasmas. *Phys. Rev. Lett*, 95, 235001 (2005).

[15] E. A. Cummings, J. E. Daily, D. S. Durfee, and S. D. Bergeson. Ultracold neutral plasma expansion in two dimensions. *Phys. Plasmas*, 12, 123501 (2005).

[16] S. Kulin, T. C. Killian, S. D. Bergeson, and S. L. Rolston. Plasma oscillations and expansion of an ultracold neutral plasma. *Phys. Rev. Lett.*, 85, 318 (2000).

[17] J.-H. Choi, B. Knuffman, X. H. Zhang, A. P. Povilus, and G. Raithel. Trapping and Evolution Dynamics of Ultracold Two-Component Plasmas. *Phys. Rev. Lett.*, 100, 175002 (2008).

[18] Jr. L. Spitzer. Wiley, New York, 1962. *Physics of Fully Ionized Gases.* Wiley, New York, 1962.

[19] Y. C. Chen, C. E. Simien, S. Laha, P. Gupta, Y. N. Martinez, P. G. Mickelson, S. B. Nagel, and T. C. Killian. Electron screening and kinetic energy oscillations in a strongly coupled plasma. *Phys. Rev. Lett.*, 93, 265003 (2004).

[20] J. Castro, H. Gao and T. C. Killian. Using sheet fluorescence to probe ion dynamics in an ultracold neutral plasma. *Plasma Phys. Control. Fusion*, 50, 124001 (2008).

[21] M. S. Murillo. Using Fermi statistics to create strongly coupled ion plasmas in atom traps. *Phys. Rev. Lett.*, 87, 115003 (2001).

[22] R. S. Fletcher, X. L. Zhang, and S. L. Rolston. Observation of collective modes of ultracold plasmas. *Phys. Rev. Lett.*, 96, 105003 (2006).

[23] J. L. Roberts, C. D. Fertig, M. J. Lim, and S. L. Rolston. Electron temperature of ultracold plasmas. *Phys. Rev. Lett.*, 92, 253003 (2004).

[24] P. Gupta, S. Laha, C. E. Simien, H. Gao, J. Castro, and T. C. Killian. Electron-Temperature Evolution in Expanding Ultracold Neutral Plasmas. *Phys. Rev. Lett.*, 99, 075005 (2007).

[25] P. Gupta. *Expansion and Electron Temperature Evolution in an Ultracold Neutral Plasma.* PhD thesis, Rice University, 2007.

[26] R. S. Fletcher, X. L. Zhang, and S. L. Rolston. Using Three-Body Recombination to Extract Electron Temperatures of Ultracold Plasmas. *Phys. Rev. Lett.*, 99, 145001 (2007).

[27] S. Mazevet, L. A. Collins, and J. D. Kress. Evolution of ultracold neutral plasmas. *Phys. Rev. Lett.*, 88, 55001 (2002).

[28] S. G. Kuzmin and T. M. ONeil. Numerical simulation of ultracold plasmas: How rapid intrinsic heating limits the development of correlation. *Phys. Rev. Lett.*, 88, 65003 (2002).

[29] S. G. Kuzmin and T. M. O'Neil. Numerical simulation of ultracold plasmas. *Phys. Plasmas*, 9, 3743 (2002).

[30] F. Robicheaux and J. D. Hanson. Simulation of the expansion of an ultracold neutral plasma. *Phys. Rev. Lett.*, 88, 55002 (2002).

[31] F. Robicheaux and J. D. Hanson. Simulated expansion of an ultra-cold, neutral plasma. *Phys. Plasmas*, 10, 2217 (2003).

[32] T. Pohl, T. Pattard, and J. M. Rost. Plasma formation from ultracold Rydberg gases. *Phys. Rev. A*, 68, 010703 (2003).

[33] T. Pohl, T. Pattard, and J. M. Rost. Kinetic modeling and molecular dynamics simulation of ultracold neutral plasmas including ionic correlations. *Phys. Rev. A*, 70, 033416 (2004).

[34] T. Pohl. *Relaxation Dynamics of Ultracold Neutral Plasmas.* PhD thesis, Technical University of Dresden, 2005.

[35] H. J. Metcalf and P. van der Straten. *Laser Cooling and Trapping.* Springer-Verlag, New York, 1999.

[36] M. S. Walhout. *Studies of Laser-Cooled and Magneto-Optically Trapped Xenon.* PhD thesis, University of Maryland, 1994.

[37] M. Walhout, H. J. Megens, A. Witte, and S. L. Rolston. Magneto-optical trapping of metastable xenon: Isotope-shift measurements. *Phys. Rev. A*, 48, R879 (1993).

[38] T. F. Gallagher. *Rydberg Atoms.* Cambridge University Press, Cambridge, England, 1994.

[39] M. P. Robinson, B. L. Tolra, M. W. Noel, T. F. Gallagher, and P. Pillet. Spontaneous evolution of Rydberg atoms into an ultracold plasma. *Phys. Rev. Lett.*, 85, 4466 (2000).

[40] D. Tomic. Simple, high-voltage, square pulse generator for ion beam deflection in a neutron generator. *Rev. Sci. Instrum.*, 61, 1729 (1990).

[41] X. L. Zhang, R. S. Fletcher, and S. L. Rolston. Using Charged Particle Imaging to Study Ultracold Plasma Expansion. AIP conference proceedings for the Non-Neutral Plasma Workshop, New York, 2008.

[42] X. L. Zhang, R. S. Fletcher, S. L. Rolston, P. N. Guzdar, and M. Swisdak. Ultracold Plasma Expansion in a Magnetic Field. *Phys. Rev. Lett.*, 100, 235002 (2008).

[43] S. D. Bergeson and R. L Spencer. Neutral-plasma oscillations at zero temperature. *Phys. Rev. E*, 67, 026414 (2003).

[44] T. Pohl, T. Pattard, and J. M. Rost. Coulomb crystallization in expanding laser-cooled neutral plasmas. *Phys. Rev. Lett.*, 92, 155003 (2004).

[45] L. Tonks. The High Frequency Behavior of a Plasma. *Phys. Rev.*, 37, 1457 (1931).

[46] A. Dattner. Resonance Densities in a Cylindrical Plasma Column. *Phys. Rev. Lett.*, 10, 205 (1963).

[47] R. J. Goldston and P. H. Rutherford. *Introduction to Plasma Physics.* IOP Press, Bristol, 1995.

[48] J. A. How and H. A. Blevin. A simplified theory for Tonks-Dattner resonances in cylindrical plasmas. *J. Phys. D: Appl. Phys.*, 9, 1123 (1976).

[49] P. M. Morse and H. Feshbach. *Methods of Theoretical Physics.* McGraw-Hill, New York, 1953.

[50] R. S. Fletcher. *Three-body recombination and Rydberg atoms in ultracold plasmas.* PhD thesis, University of Maryland, 2008.

[51] T. Pohl, and T. Pattard. *Strong-conpling Effect in the Relaxation Dynamics of Ultracold Neutral Plasmas.* *J. Phys. Conf. Series*, 11, 223 (2005).

[52] T. C. Killian, M. J. Lim, S. Kulin, R. Dumke, S. D. Bergeson, and S. L. Rolston. Formation of Rydberg Atoms in an Expanding Ultracold Neutral Plasma. *Phys. Lett. Lett.*, 86, 3759 (2001).

[53] P. Mansbach and J. Keck. Monte Carlo trajectory calculations of atomic excitation and ionization by thermal electrons. *Phys. Rev.*, 181, 275 (1969).

[54] Y. Hahn. Plasma density effects on the three-body recombination rate coefficients. *Phys. Lett. A*, 231, 82 (1997).

[55] Y. Hahn. Improved rates for three-body recombination at low temperature. *Phys. Lett. A*, 264, 465 (2000).

[56] F. Robicheaux (private communication).

[57] T. Pohl (private communication).

[58] T. Pohl, D. Vrinceanu, and H. R. Sadeghpour. Rydberg Atom Formation in Ultracold Plasmas: Small Energy Transfer with Large Consequences. *Phys. Rev. Lett.*, 100, 223201 (2008).

[59] S. S. Harilal, M. S. Tillack, B. OŚhay, C. V. Bindhu, and F. Najmabadi. Confinement and dynamics of laser-produced plasma expanding across a transverse magnetic field. *Phys. Rev. E*, 69, 026413 (2004).

[60] F. C. Hoh. Low-Temperature Plasma Diffusion in a Magnetic Field. *Rev. Mod. Phys.*, 34, 267 (1962).

[61] F. Boeschoten. Low-Temperature Plasma Diffusion in a Magnetic Field. *J. Nucl. Energy, Part C Plasma Phys.*, 6, 339 (1964).

[62] G. I. Barenblatt. *Similarity, Self-Similarity and Intermediate Asymptotics.* Consultants Bureau, New York, 1978.

[63] X. L. Zhang, R. S. Fletcher, and S. L. Rolston. Observation of an Ultracold Plasma Instability. *Phys. Rev. Lett.*, 101, 195002 (2008).

[64] G. D. Conway, D. N. Borba, B. Alper, D. V. Bartlett, C. Gormezano, M. G. von Hellermann, A. C. Maas, V. V. Parail, P. Smeulders, and K D. Zastrow. Suppression of Plasma Turbulence During Optimized Shear Configurations in JET. *Phys. Rev. Lett.*, 84, 1463 (2000).

[65] M. M Oppenheim, L. P. Dyrud, and L. Ray. Plasma instabilities in meteor trails: Linear theory. *J. Geophys. Res.*, 108, 1063 (2003).

[66] D. T. Farley, Jr. Two-Stream Plasma Instability as a Source of Irregularities in the Ionosphere. *Phys. Rev. Lett.*, 10, 279 (1963).

[67] O. Buneman. Excitation of Field Aligned Sound Waves by Electron Streams. *Phys. Rev. Lett.*, 10, 285 (1963).

[68] R. L. Merlino, A. Barkan, C. Thompson, and N. D'Angelo. Laboratory studies of waves and instabilities in dusty plasmas. *Phys. Plasmas*, 5, 1607 (1998).

[69] N. A. Krall and P. C. Liewer. Low-Frequency Instabilities in Magnetic Pulses. *Phys. Rev. A*, 4, 2094 (1971).

[70] A. A. Litvak, Y. Raitses, and N. J. Fisch. Experimental studies of high-frequency azimuthal waves in Hall thrusters. *Phys. Plasmas*, 11, 1701 (2004).

[71] A. Lazurenko, V. Vial, M. Prioul, and A. Bouchoule. Experimental investigation of high-frequency drifting perturbations in Hall thrusters. *Phys. Plasmas*, 12, 013501 (2005).

[72] J. C. Adam, A. Héron, and G. Laval. Study of stationary plasma thrusters using two-dimensional fully kinetic simulations. *Phys. Plasmas*, 11, 295 (2004).

[73] A. Ducrocq, J. C. Adam, A. Héron, and G. Laval. High-frequency electron drift instability in the cross-field configuration of Hall thrusters. *Phys. Plasmas*, 13, 102111 (2006).